

# On the computational modeling of lipid bilayers using thin-shell theory

Roger A. Sauer <sup>1</sup>

*Aachen Institute for Advanced Study in Computational Engineering Science (AICES),  
RWTH Aachen University, Templergraben 55, 52056 Aachen, Germany*

Published<sup>2</sup> in D. Steigmann (Ed.), *The Role of Mechanics in the Study of Lipid Bilayers*

DOI: [10.1007/978-3-319-56348-0\\_5](https://doi.org/10.1007/978-3-319-56348-0_5)

Submitted on 1. February 2017, Published on 25. May 2017

---

## Abstract

This chapter discusses the computational modeling of lipid bilayers based on the nonlinear theory of thin shells. Several computational challenges are identified and various theoretical and computational ingredients are proposed in order to counter them. In particular,  $C^1$ -continuous, NURBS-based, LBB-conforming surface finite element discretizations are discussed. The constitutive behavior of the bilayer is based on in-plane viscosity and (near) area-incompressibility combined with the Helfrich bending model. Various shear stabilization techniques are proposed for quasi-static computations. All ingredients are formulated in the curvilinear coordinate system characterizing general surface parametrizations. The consistent linearization of the formulation is presented, and several numerical examples are shown.

---

## Contents

<b>1</b>	<b>Computational ingredients and challenges</b>	<b>7</b>
<b>2</b>	<b>Literature survey</b>	<b>8</b>
<b>3</b>	<b>Surface description</b>	<b>10</b>
3.1	Surface parameterization . . . . .	10
3.2	Surface decomposition . . . . .	11
3.3	Surface differentiation . . . . .	12
3.4	Surface curvature . . . . .	14
3.5	Surface Cayley-Hamilton . . . . .	14

---

<sup>1</sup>corresponding author, email: [sauer@aices.rwth-aachen.de](mailto:sauer@aices.rwth-aachen.de)

<sup>2</sup>This pdf is the personal version of a book chapter whose final version is available at <http://link.springer.com>

<b>4</b>	<b>Surface kinematics</b>	<b>14</b>
4.1	Surface deformation . . . . .	15
4.2	Surface motion . . . . .	16
4.3	Surface incompressibility . . . . .	18
4.4	Surface variation . . . . .	18
4.5	Surface linearization . . . . .	18
<b>5</b>	<b>Surface balance</b>	<b>19</b>
5.1	Sectional forces and moments . . . . .	19
5.2	Balance of linear momentum . . . . .	21
5.3	Balance of angular momentum . . . . .	21
5.4	Boundary conditions . . . . .	21
5.5	Mechanical power balance . . . . .	22
<b>6</b>	<b>Surface constitution</b>	<b>22</b>
6.1	Dissipation inequality . . . . .	23
6.2	Constrained visco-elasticity . . . . .	23
6.3	Linearization of $\delta\Psi_0$ . . . . .	24
6.4	Material stability . . . . .	25
<b>7</b>	<b>The Helfrich energy</b>	<b>25</b>
7.1	Area-compressible lipid bilayer . . . . .	26
7.2	Area-incompressible lipid bilayer . . . . .	26
7.3	Model properties . . . . .	27
7.4	Material tangent . . . . .	27
	7.4.1 Area-compressibility . . . . .	28
	7.4.2 Area-incompressibility . . . . .	28
	7.4.3 Bending part . . . . .	28
7.5	The Canham model . . . . .	29
<b>8</b>	<b>Weak form</b>	<b>29</b>
8.1	Unconstrained system . . . . .	29
8.2	Constrained system . . . . .	30
8.3	Decomposition . . . . .	30
8.4	Linearization . . . . .	30

<b>9</b>	<b>Analytical solutions</b>	<b>31</b>
9.1	Pure bending and stretching of a flat sheet . . . . .	31
9.2	Inflation of a sphere . . . . .	33
<b>10</b>	<b>Rotation-free shell FE</b>	<b>34</b>
10.1	FE approximation . . . . .	34
10.2	Discretization of kinematical variations . . . . .	35
10.3	Discretized weak form . . . . .	36
10.4	Temporal discretization of the viscosity term . . . . .	37
10.5	Linearization . . . . .	37
10.6	C1-continuous shape functions . . . . .	38
10.7	Patch interfaces . . . . .	39
<b>11</b>	<b>Mixed finite elements</b>	<b>40</b>
11.1	Discretization of the area constraint . . . . .	40
11.2	Solution procedure . . . . .	40
11.3	LBB condition . . . . .	41
11.4	Normalization . . . . .	42
<b>12</b>	<b>Lipid bilayer stabilization</b>	<b>42</b>
12.1	Adding stiffness . . . . .	43
12.1.1	In-plane shear and bulk stabilization . . . . .	43
12.1.2	Sole in-plane shear stabilization . . . . .	43
12.2	Normal projection . . . . .	44
12.3	Summary of the stabilization schemes . . . . .	44
12.4	Performance of the stabilization schemes . . . . .	45
12.4.1	Pure bending and stretching of a flat sheet . . . . .	45
12.4.2	Inflation of a sphere . . . . .	47
<b>13</b>	<b>Numerical examples</b>	<b>48</b>
13.1	Bilayer tethering . . . . .	48
13.2	Bilayer budding . . . . .	50
13.3	Bilayer indentation . . . . .	52
<b>14</b>	<b>Conclusion</b>	<b>53</b>

## List of important symbols

<b>1</b>	identity tensor in $\mathbb{R}^3$
$a$	determinant of matrix $[a_{\alpha\beta}]$
$A$	determinant of matrix $[A_{\alpha\beta}]$
$\mathbf{a}_\alpha$	co-variant tangent vectors of surface $\mathcal{S}$ at point $\mathbf{x}$ ; $\alpha = 1, 2$
$\mathbf{A}_\alpha$	co-variant tangent vectors of surface $\mathcal{S}_0$ at point $\mathbf{X}$ ; $\alpha = 1, 2$
$\mathbf{a}^\alpha$	contra-variant tangent vectors of surface $\mathcal{S}$ at point $\mathbf{x}$ ; $\alpha = 1, 2$
$\mathbf{A}^\alpha$	contra-variant tangent vectors of surface $\mathcal{S}_0$ at point $\mathbf{X}$ ; $\alpha = 1, 2$
$\mathbf{a}_{\alpha,\beta}$	parametric derivative of $\mathbf{a}_\alpha$ w.r.t. $\xi^\beta$
$\mathbf{a}_{\alpha;\beta}$	co-variant derivative of $\mathbf{a}_\alpha$ w.r.t. $\xi^\beta$
$a_{\alpha\beta}$	co-variant metric components of surface $\mathcal{S}$ at point $\mathbf{x}$
$A_{\alpha\beta}$	co-variant metric components of surface $\mathcal{S}_0$ at point $\mathbf{X}$
$a^{\alpha\beta\gamma\delta}$	derivative of $a^{\alpha\beta}$ w.r.t. $a_{\gamma\delta}$
<b>a</b>	class of stabilization methods based on artificial shear viscosity
<b>A</b>	class of stabilization methods based on artificial shear stiffness
$b_{\alpha\beta}$	co-variant curvature tensor components of surface $\mathcal{S}$ at point $\mathbf{x}$
$B_{\alpha\beta}$	co-variant curvature tensor components of surface $\mathcal{S}_0$ at point $\mathbf{X}$
$b^{\alpha\beta\gamma\delta}$	derivative of $b^{\alpha\beta}$ w.r.t. $a_{\gamma\delta}$
<b>b</b>	curvature tensor of surface $\mathcal{S}$ at point $\mathbf{x}$
<b>B</b>	left surface Cauchy-Green tensor
<b>C</b>	right surface Cauchy-Green tensor
$c^{\alpha\beta\gamma\delta}$	derivative of $\tau^{\alpha\beta}$ w.r.t. $a_{\gamma\delta}$
$\gamma$	surface tension of $\mathcal{S}$
$\Gamma_{\alpha\beta}^\gamma$	Christoffel symbols of the second kind of surface $\mathcal{S}$
$d_{\alpha\beta}$	co-variant components of the symmetric surface velocity gradient
<b>D</b>	dissipation per current surface area
$D_0$	dissipation per reference surface area
$da$	differential surface element on $\mathcal{S}$
$dA$	differential surface element on $\mathcal{S}_0$
$d^{\alpha\beta\gamma\delta}$	derivative of $\tau^{\alpha\beta}$ w.r.t. $b_{\gamma\delta}$
$\delta\dots$	variation of ...
$\Delta\dots$	increment of ... that is required for linearization
$\Delta_s$	Laplace operator on surface $\mathcal{S}$
$\text{div}_s$	divergence operator on surface $\mathcal{S}$
$e$	index numbering the finite elements; $e = 1, \dots, n_{\text{el}}$
$e^{\alpha\beta\gamma\delta}$	derivative of $M_0^{\alpha\beta}$ w.r.t. $a_{\gamma\delta}$
$\epsilon$	penalty parameter
<b>E</b>	surface Green-Lagrange strain tensor
$f^{\alpha\beta\gamma\delta}$	derivative of $M_0^{\alpha\beta}$ w.r.t. $b_{\gamma\delta}$
<b>f</b>	'body' force acting on $\mathcal{S}$
$\mathbf{f}^e$	finite element force vector of element $\Omega^e$
$g$	expression for the area-incompressibility constraint
$G$	expression for the weak form
$G^e$	contribution to $G$ from finite element $\Omega^e$
$\mathbf{g}^e$	finite element 'force vector' of element $\Omega^e$ due to constraint $g$
$\nabla_s$	gradient operator on surface $\mathcal{S}$
$H$	mean curvature of $\mathcal{S}$ at $\mathbf{x}$
$H_0$	spontaneous curvature prescribed at $\mathbf{x}$
$\eta$	in-plane surface viscosity

$I$	index numbering the finite element nodes
$I_1, I_2$	invariants of the surface Cauchy-Green tensors
$\mathbf{i}$	surface identity tensor on $\mathcal{S}$
$\mathbf{I}$	surface identity tensor on $\mathcal{S}_0$
$J$	area change between $\mathcal{S}_0$ and $\mathcal{S}$
$J_a$	area change between $\mathcal{P}$ and $\mathcal{S}$
$J_A$	area change between $\mathcal{P}$ and $\mathcal{S}_0$
$k$	bending modulus
$k_g$	Gaussian modulus
$K$	initial surface bulk modulus (=area compression modulus)
$K_{\text{eff}}$	effective surface bulk modulus
$\mathbf{k}^e$	finite element tangent matrix associated with $\mathbf{f}^e$ and $\mathbf{g}^e$
$\kappa$	Gaussian curvature of surface $\mathcal{S}$ at $\mathbf{x}$
$\kappa_1, \kappa_2$	principal curvatures of surface $\mathcal{S}$ at $\mathbf{x}$
$L_I$	pressure shape function of finite element node $I$
$\mathcal{L}$	interface between two NURBS patches
$\lambda_1, \lambda_2$	principal surface stretches of $\mathcal{S}$ at $\mathbf{x}$
$m_e$	number of pressure nodes of finite element $\Omega^e$
$m_\nu, m_\tau$	bending moment components acting at $\mathbf{x} \in \partial\mathcal{S}$
$\bar{m}_\nu, \bar{m}_\tau$	prescribed bending moment components
$M^{\alpha\beta}$	contra-variant bending moment components
$M_0^{\alpha\beta}$	$= JM^{\alpha\beta}$
$\mu$	initial in-plane membrane shear stiffness
$\mu_{\text{eff}}$	effective in-plane membrane shear stiffness
$n_{\text{no}}$	total number of finite element nodes used to discretize $\mathcal{S}$
$n_{\text{el}}$	total number of finite elements used to discretize $\mathcal{S}$
$n_{\text{mo}}$	total number of finite element nodes used to discretize pressure $q$
$n_e$	number of displacement nodes of finite element $\Omega^e$
$N^{\alpha\beta}$	total, contra-variant, in-plane membrane stress components
$N_I$	displacement shape function of finite element node $I$
$\mathbf{n}$	surface normal of $\mathcal{S}$ at $\mathbf{x}$
$\mathbf{N}$	surface normal of $\mathcal{S}_0$ at $\mathbf{X}$
$\mathbf{N}$	array of the shape functions for element $\Omega^e$
$\boldsymbol{\nu}$	normal vector on $\partial\mathcal{S}$
$\xi^\alpha$	convective surface coordinates; $\alpha = 1, 2$
$\mathcal{P}$	parametric domain spanned by $\xi^1$ and $\xi^2$
$\mathbf{P}$	class of stabilization methods based on normal projection; projection matrix
$\psi$	Helmholtz free energy per unit mass
$\Psi_0$	Helmholtz free energy per reference area
$q$	Lagrange multiplier associated with area-incompressibility
$\mathbf{q}$	array of all Lagrange multipliers $q_I$ in the system; $I = 1, \dots, n_{\text{mo}}$
$\mathbf{q}_e$	array of all Lagrange multipliers $q_I$ for finite element $\Omega^e$ ; $I = 1, \dots, m_e$
$\mathcal{R}$	arbitrary subregion of $\mathcal{S}$
$\rho$	surface density of $\mathcal{S}$ at $\mathbf{x}$
$\rho_0$	surface density of $\mathcal{S}_0$ at $\mathbf{x}$
$S^\alpha$	contra-variant, out-of-plane shear stress components
$\mathcal{S}$	current configuration of the surface
$\mathcal{S}_0$	initial configuration of the surface
$\boldsymbol{\sigma}$	Cauchy stress tensor of the shell
$\sigma^{\alpha\beta}$	stretch-related, contra-variant, in-plane stress components

$\mathbf{t}$	effective traction acting on the boundary $\partial\mathcal{S}$ normal to $\boldsymbol{\nu}$
$\bar{\mathbf{t}}$	prescribed boundary tractions on Neumann boundary $\partial_t\mathcal{S}$
$\mathbf{T}$	traction acting on the boundary $\partial\mathcal{S}$ normal to $\boldsymbol{\nu}$
$\mathbf{T}^\alpha$	traction acting on the boundary $\partial\mathcal{S}$ normal to $\mathbf{a}^\alpha$
$\tau^{\alpha\beta}$	$= J\sigma^{\alpha\beta}$
$\mathcal{V}, \mathcal{Q}$	admissible function spaces
$\varphi$	deformation map of surface $\mathcal{S}$
$\bar{\varphi}$	prescribed boundary deformations on boundary $\partial_x\mathcal{S}$
$w$	hyperelastic stored surface energy density (per current surface area)
$W$	hyperelastic stored surface energy density (per reference surface area)
$\mathbf{x}$	current position of a surface point on $\mathcal{S}$
$\mathbf{X}$	initial position of $\mathbf{x}$ on the reference surface $\mathcal{S}_0$
$\mathbf{x}_I$	position vector of finite element node $I$ lying on $\mathcal{S}$
$\mathbf{X}_I$	initial position of finite element node $I$ on $\mathcal{S}_0$
$\mathbf{x}$	stacked array of all $\mathbf{x}_I$ of the discretized surface; $I = 1, \dots, n_{\text{no}}$
$\mathbf{x}_e$	stacked array of all $\mathbf{x}_I$ for finite element $\Omega^e$ ; $I = 1, \dots, n_e$
$\mathbf{X}_e$	stacked array of all $\mathbf{X}_I$ for finite element $\Omega_0^e$ ; $I = 1, \dots, n_e$
$\Omega^e$	current configuration of finite element $e$
$\Omega_0^e$	reference configuration of finite element $e$

## Part I: Introduction

The aim of this work is to present the computational treatment of lipid bilayers using the framework of isogeometric finite element analysis and non-linear shell theory. The presentation follows earlier work on membranes (Sauer et al., 2014) and shells (Sauer and Duong, 2017; Duong et al., 2017; Sauer et al., 2017). It thus presents a condensed and combined version of earlier work by focussing on the most important aspects that are required for the computational description of lipid bilayers. Additionally, several new parts have been incorporated into the presentation. Those are:

- a summary and discussion of the computational challenges
- an extension of the theory to include surface differential operators, surface contact and surface viscosity
- the discretization and linearization of the viscosity term
- an investigation of the LBB condition for mixed shell finite elements
- a computational example on lipid bilayer indentation

The remainder of Part I gives an overview of the ingredients and challenges of the computational modeling of lipid bilayers (Sec. 1), and surveys related literature (Sec. 2). Part II (Secs. 4–9) and Part III (Secs. 10–13) then discuss the theoretical background and the computational modeling in detail. Readers familiar with shell theory may directly jump to Part III and revisit relevant sections of Part II as they are addressed. Sec. 14 concludes this work.

# 1 Computational ingredients and challenges

The modeling of lipid bilayer shells is a challenging task due to a variety of reasons. Lipid bilayers are liquid shells that are characterized by in-plane flow and out-of-plane bending elasticity (Fig. 1a). The mechanics of such shells can lead to very complex surface shapes (Fig. 1b).

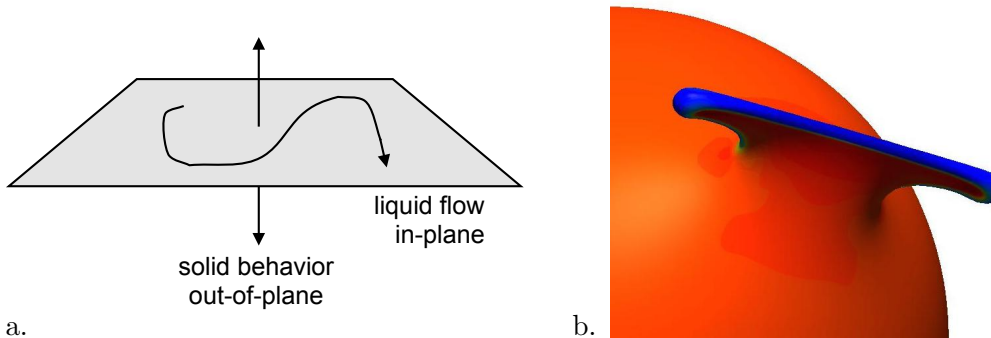


Figure 1: Lipid bilayer deformations: a. combined solid-like and liquid-like behavior; b. complex bud shapes (Sauer et al., 2017).

Tab. 1 gives an overview of the computational modeling challenges of lipid bilayers and lists corresponding ingredients to deal with them. The remainder of this section provides a short

challenge	ingredient	Sec.
surface description	curvilinear coordinates	3
liquid- & solid-like behavior	in-plane flow + out-of-plane bending	4
geometric PDE's	surface balance laws	5
bilayer constitution	Helfrich model + in-plane viscosity	6 & 7
non-linearity	consistent linearization	8 & 10
smooth discretization	NURBS-based surface finite elements	10
area-incompressibility	LBB-conforming mixed methods	11
zero shear stiffness	in-plane shear stabilization	12
complex surface flow	surface ALE	–
coupled problems	coupled balance laws	–
local refinement	LR-B-splines, LR-NURBS	–
tilt, inter-layer sliding	additional degrees-of-freedom	–

Table 1: Lipid bilayer modeling: computational challenges and corresponding model ingredients (and the sections where they are addressed).

discussion on those challenges.

In order to deal with the solid- and liquid-like behavior of lipid bilayers, a very general model formulation is required that is capable of describing the kinematics of large bending deformations and surface flows. This requires a very general surface description that can capture large deformations and rotations. Such a formulation is offered by curvilinear surface coordinates. It is presented in Secs. 3 and 4. Curvilinear coordinates offer the extra advantage that they can be used to define the finite element shape functions. In consequence this leads to a straight-forward finite element description of the problem.

The bilayer deformation is governed by so-called geometric PDE's. These are partial differential equations that live on evolving surfaces. For mechanical systems, these PDE's follow from the

balance laws of mass and momentum. This is presented in Sec. 5.

In order to solve the PDE's, the constitutive behavior of the bilayer has to be defined. A popular approach is to use the elastic bending model of Helfrich (1973) and combine it with in-plane viscosity. In general, constitution needs to be able to account for the full range of possible deformation. Therefore, the bilayer constitution should also be described in the curvilinear coordinate system of the evolving surface. This is presented in Secs. 6 and 7.

The PDE's and their corresponding weak form are strongly nonlinear. In order to solve such a system within implicit finite element methods, the consistent linearization of the formulation is required. This is presented in Secs. 8 and 10.

Lipid bilayers are very thin structures, and it is appropriate to describe them with thin-shell theory. Thin-shell theory leads to a high-order weak form that requires a surface description that is at least  $C^1$ -continuous. Such a formulation is provided by NURBS-based finite element spaces. They are presented in Sec. 10.

The surface flow of lipid bilayers can be considered to be area-incompressible. Area-incompressibility is a constraint that introduces new unknowns. The discretization of those needs to conform with the discretization of the surface and its velocity according to the LBB-condition. This is discussed in Sec. 11.

Under quasi-static conditions, the bilayer offers no resistance to shear deformations. To solve such cases computationally, numerical shear stabilization is required. Several stabilization techniques can be used, as is presented in Sec. 12.

Under dynamic conditions, viscosity offers resistance to shear flow. However, surface flow can lead to very large surface deformations that cannot be tracked by a pure Lagrangian (i.e. material) mesh. Also pure Eulerian (i.e. fixed) meshes cannot be used, since the surface shape can change. Thus an arbitrary Lagrangian-Eulerian (ALE) surface formulation is required.

The mechanics of lipid bilayers may be coupled to other phenomena, such as diffusion, phase transitions and protein binding reactions. To account for these, the surface balance laws have to be extended by the energy and mass balance of multiple species. A recent theory for this has been provided by Sahu et al. (2017).

The surface deformation can become very localized. For such cases local mesh refinement is desirable. Classical NURBS don't offer this, but there is recent work on locally refined NURBS (Zimmermann and Sauer, 2017).

Classical thin-shell theory does not account for tilting of the lipids. Also, they don't account for sliding between the two lipid layers. In order to describe these aspects the kinematic description of the bilayer deformation has to be generalized. This effectively adds degrees-of-freedom to the formulation. Lipid tilt and inter-layer sliding are addressed in other chapters of this book.

## 2 Literature survey

This section gives an overview of existing literature that is related to the computational modeling of lipid bilayers based on non-linear shell theory. The presentation focuses on finite element models and follows Sauer et al. (2017).

In the past, several computational models have been proposed for cell membranes. Depending on how the membrane is discretized, two categories can be distinguished: Models based on an explicit surface discretization, and models based on an implicit surface discretization. In

the second category, the surface is captured by a phase field (Du and Wang, 2007) or level set function (Salac and Miksis, 2011) that is defined on the surrounding volume mesh. In the first category, the surface is captured directly by a surface mesh. The approach is particularly suitable if only surface effects are studied, such that no surrounding volume mesh is needed. This is the approach taken here. An example is to use Galerkin surface finite elements: The first corresponding 3D FE model for lipid bilayer membranes seems to be the formulation of Feng and Klug (2006) and Ma and Klug (2008). Their FE formulation is based on so-called subdivision surfaces (Cirak and Ortiz, 2001), which provide  $C^1$ -continuous FE surface discretizations. Such discretizations are advantageous, since they do not require additional degrees of freedom as  $C^0$ -continuous FE formulations do. Still,  $C^0$ -continuous FEs have been considered to model red blood cell (RBC) membranes and their supporting protein skeleton (Dao et al., 2003; Peng et al., 2010), phase changes of lipid bilayers (Elliott and Stinner, 2010), and viscous cell membranes (Tasso and Buscaglia, 2013). Subdivision finite elements have been used to study confined cells (Kahraman et al., 2012). Lipid bilayers can also be modeled with so-called ‘solid shell’ (i.e. classical volume) elements instead of surface shell elements (Kloppel and Wall, 2011). Using solid elements,  $C^0$ -continuity is sufficient, but the formulation is generally less efficient. For two-dimensional and axisymmetric problems also  $C^1$ -continuous B-spline and Hermite finite elements have been used to study membrane surface flows (Arroyo and DeSimone, 2009; Rahimi and Arroyo, 2012), cell invaginations (Rim et al., 2014), and cell tethering and adhesion (Rangarajan and Gao, 2015). The latter work also discusses the generalization to three-dimensional B-spline FE. For some problems it is also possible to use specific, Monge-patch FE discretizations (Rangamani et al., 2013, 2014).

The computational framework considered here is based on isogeometric finite elements (Hughes et al., 2005; Cottrell et al., 2009). Those provide  $C^1$ -continuity through the use of splines. Isogeometric FE formulations have been applied to solid shells (Kiendl et al., 2009, 2010, 2015; Benson et al., 2011; Nguyen-Thanh et al., 2011) based on rotation-free FE discretizations (Flores and Estrada, 2007; Linhard et al., 2007; Dung and Wells, 2008). In Duong et al. (2017) a new isogeometric FE formulation is proposed using curvilinear shell theory (Naghdi, 1982; Pietraszkiewicz, 1989; Libai and Simmonds, 1998). The isogeometric shell model has been extended to liquid shells (Sauer et al., 2017) based on the shell formulation of Steigmann (1999) and the bilayer models of Canham (1970) and Helfrich (1973).

There are also several works that do not use finite element approaches. Examples are numerical ODE integration (Agrawal and Steigmann, 2009), Monte Carlo methods (Ramakrishnan et al., 2010), molecular dynamics (Li and Lykotrafitis, 2012), finite difference methods (Lau et al., 2012; Gu et al., 2014) and mesh-free methods (Rosolen et al., 2013). There are also non-Galerkin FE approaches that use triangulated surfaces, e.g. see Jarić et al. (1995); Jie et al. (1998).

Ideal liquids lack shear stiffness. Under quasi-static conditions, liquid membranes and shells therefore do not provide any resistance to in-plane shear deformations and thus need to be stabilized. Various stabilization methods have been proposed in the past, considering artificial viscosity (Ma and Klug, 2008; Sauer, 2014), artificial stiffness (Kahraman et al., 2012) and normal offsets – either as a projection of the solution (with intermediate mesh update steps) (Sauer, 2014), or as a restriction of the surface variation (Rangarajan and Gao, 2015). The instability problem is absent, if shear stiffness is present, e.g. due to an underlying cytoskeleton, like in RBCs (Dao et al., 2003; Peng et al., 2010; Kloppel and Wall, 2011).

## Part II: Theoretical Description

Part II discusses the theoretical description of lipid bilayers that is required for the computational formulation following in Part III.

### 3 Surface description

This section discusses the description of curved surfaces based on the general framework of curvilinear coordinates. The description is based on a surface parameterization (3.1), from which the surface decomposition (3.2), surface differentiation (3.3), surface curvature (3.4) and the surface Cayley-Hamilton theorem (3.5) follow.

#### 3.1 Surface parameterization

The bilayer surface, denoted by  $\mathcal{S}$ , can be described by the parametric description

$$\mathbf{x} = \mathbf{x}(\xi^\alpha), \quad (1)$$

where  $\xi^\alpha$ ,  $\alpha = 1, 2$  are coordinates associated with a parameter domain  $\mathcal{P}$ . Eq. (1) corresponds to a mapping from point  $(\xi^1, \xi^2) \in \mathcal{P}$  to the surface point  $\mathbf{x} \in \mathcal{S}$ , see Fig. 2. The mapping

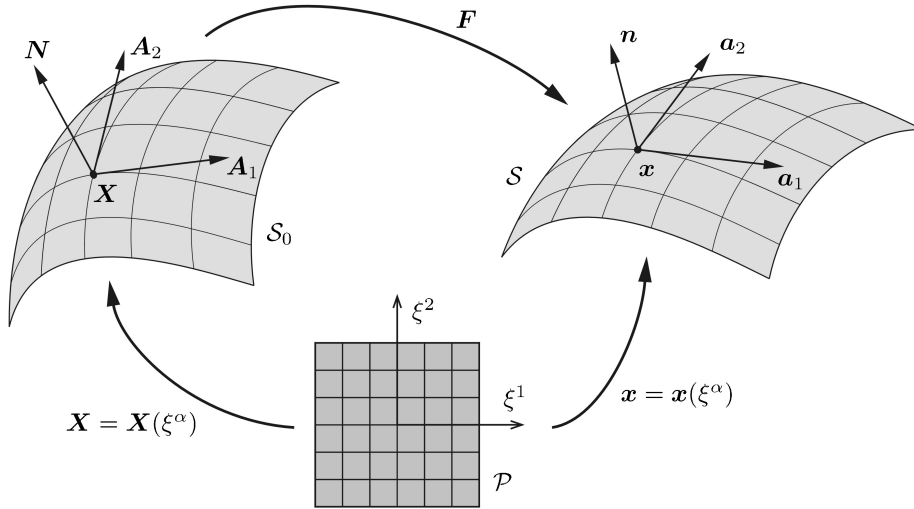


Figure 2: Mapping between parameter domain  $\mathcal{P}$ , reference surface  $\mathcal{S}_0$  and current surface  $\mathcal{S}$  (Sauer et al., 2014).

reflects the property that the surface is a 2D object embedded within 3D space. Mapping (1) fully characterizes the surface geometry. Coordinates  $\xi^\alpha$  are known as *curvilinear coordinates*. The tangent vector to coordinate  $\xi^\alpha$  is given by

$$\mathbf{a}_\alpha = \frac{\partial \mathbf{x}}{\partial \xi^\alpha}. \quad (2)$$

The two vectors  $\mathbf{a}_1$  and  $\mathbf{a}_2$  are generally not orthonormal, i.e. the four numbers

$$a_{\alpha\beta} = \mathbf{a}_\alpha \cdot \mathbf{a}_\beta, \quad (3)$$

generally give  $[a_{\alpha\beta}] \neq [1 \ 0; 0 \ 1]$ . The object  $a_{\alpha\beta}$  is an important characteristic of the surface, known as the *surface metric*. To restore orthonormality, a second set of tangent vectors  $\mathbf{a}^1$  and  $\mathbf{a}^2$  is introduced such that

$$\mathbf{a}_\alpha \cdot \mathbf{a}^\beta = \delta_\alpha^\beta, \quad (4)$$

where  $[\delta_\alpha^\beta] = [1 \ 0; 0 \ 1]$ .  $\delta_\alpha^\beta$  is known as the *Kronecker delta*. Multiplication by  $\delta_\alpha^\beta$  simply exchanges indices, e.g.  $\mathbf{a}^\alpha \delta_\alpha^\beta = \mathbf{a}^\beta$ . It follows that

$$\mathbf{a}^\alpha = a^{\alpha\beta} \mathbf{a}_\beta, \quad (5)$$

where  $[a^{\alpha\beta}] = [a_{\alpha\beta}]^{-1}$ . Tangent vectors  $\mathbf{a}_1$  and  $\mathbf{a}_2$  are also called the *co-variant tangent vectors*, while  $\mathbf{a}^1$  and  $\mathbf{a}^2$  are also known as the *contra-variant tangent vectors*. Analogously,  $a_{\alpha\beta}$  is called the *co-variant surface metric* and  $a^{\alpha\beta}$  the *contra-variant surface metric*. Eq. (5) uses index notation, i.e. summation is implied on repeated indices. By construction, repeated indices always appear as co-variant/contra-variant pairs.

The normal vector to surface  $\mathcal{S}$  can be defined as

$$\mathbf{n} = \frac{\mathbf{a}_1 \times \mathbf{a}_2}{\|\mathbf{a}_1 \times \mathbf{a}_2\|}. \quad (6)$$

The quantity  $J_a := \|\mathbf{a}_1 \times \mathbf{a}_2\|$  gives the area enclosed by vectors  $\mathbf{a}_1$  and  $\mathbf{a}_2$ . It can be shown that  $J_a = \sqrt{\det[a_{\alpha\beta}]}$ .

### 3.2 Surface decomposition

The triads  $\{\mathbf{a}_1, \mathbf{a}_2, \mathbf{n}\}$  and  $\{\mathbf{a}^1, \mathbf{a}^2, \mathbf{n}\}$  form bases that can be used to decompose vectors  $\mathbf{v} \in \mathbb{R}^3$  into their in-plane and out-of-plane components, i.e.

$$\mathbf{v} = \mathbf{v}_s + \mathbf{v}_n, \quad \mathbf{v}_s = v^\alpha \mathbf{a}_\alpha = v_\alpha \mathbf{a}^\alpha, \quad \mathbf{v}_n = v \mathbf{n}, \quad (7)$$

where  $v = \mathbf{v} \cdot \mathbf{n}$  is the vector component along  $\mathbf{n}$ , and  $v_\alpha = \mathbf{v} \cdot \mathbf{a}_\alpha$  and  $v^\alpha = \mathbf{v} \cdot \mathbf{a}^\alpha$  are the vector components along  $\mathbf{a}^\alpha$  and  $\mathbf{a}_\alpha$ , respectively.  $v_\alpha$  is also called the co-variant and  $v^\alpha$  the contra-variant vector component. Applying (5) to (7) yields  $v^\alpha = a^{\alpha\beta} v_\beta$ . Likewise  $v_\alpha = a_{\alpha\beta} v^\beta$ . Generally,  $a^{\alpha\beta}$  and  $a_{\alpha\beta}$  raise and lower indices, respectively.

Two important second order tensors are the surface identity tensor,

$$\mathbf{i} := \mathbf{a}_\alpha \otimes \mathbf{a}^\alpha = \mathbf{a}^\alpha \otimes \mathbf{a}_\alpha, \quad (8)$$

and the full identity in  $\mathbb{R}^3$ ,

$$\mathbf{1} := \mathbf{i} + \mathbf{n} \otimes \mathbf{n}. \quad (9)$$

With those follow,  $\mathbf{i}\mathbf{v} = \mathbf{v}_s$ ,  $\mathbf{i}\mathbf{v}_s = \mathbf{v}_s$ ,  $\mathbf{1}\mathbf{v} = \mathbf{v}$  and  $\mathbf{1}\mathbf{v}_s = \mathbf{v}_s$ . Thus  $\mathbf{i}$ , can be viewed as a projection operator, that extracts  $\mathbf{v}_s$  from  $\mathbf{v}$ . In the same fashion  $\mathbf{i}$  can be used to extract the in-plane contents of a tensor. For example, the surface part of the second order tensor  $\mathbf{c} \in \mathbb{R}^3 \times \mathbb{R}^3$  is

$$\mathbf{c}_s := \mathbf{i} \cdot \mathbf{c} \mathbf{i}. \quad (10)$$

From (8) follows

$$\begin{aligned}
\mathbf{c}_s &= c^{\alpha\beta} \mathbf{a}_\alpha \otimes \mathbf{a}_\beta, & c^{\alpha\beta} &= \mathbf{a}^\alpha \cdot \mathbf{c} \mathbf{a}^\beta, \\
&= c_\beta^\alpha \mathbf{a}_\alpha \otimes \mathbf{a}^\beta, & c_\beta^\alpha &= \mathbf{a}^\alpha \cdot \mathbf{c} \mathbf{a}_\beta, \\
&= c_{\alpha\beta} \mathbf{a}^\alpha \otimes \mathbf{a}^\beta, & c_{\alpha\beta} &= \mathbf{a}_\alpha \cdot \mathbf{c} \mathbf{a}_\beta, \\
&= c_\alpha^\beta \mathbf{a}^\alpha \otimes \mathbf{a}_\beta, & c_\alpha^\beta &= \mathbf{a}_\alpha \cdot \mathbf{c} \mathbf{a}^\beta.
\end{aligned} \tag{11}$$

If  $\mathbf{c}$  is symmetric, then  $c_\beta^\alpha = c_\alpha^\beta =: c_\beta^\alpha$ . Apart from  $\mathbf{c}_s$ , tensor  $\mathbf{c}$  also has components along  $\mathbf{n} \otimes \mathbf{n}$ ,  $\mathbf{a}_\alpha \otimes \mathbf{n}$  and  $\mathbf{n} \otimes \mathbf{a}_\alpha$ .

Based on these definitions, three important tensor functions can be defined. The first is the surface trace, defined by

$$\text{tr}_s \mathbf{c} := \mathbf{i} : \mathbf{c}. \tag{12}$$

It is related to the regular trace operator  $\text{tr} \mathbf{c} := \mathbf{1} : \mathbf{c}$ , by  $\text{tr}_s \mathbf{c} := \text{tr} \mathbf{c}_s$ . Further  $\text{tr}_s \mathbf{c} = c_\alpha^\alpha$ . The second important tensor function is the surface determinant, defined by

$$\det_s \mathbf{c} := \det[c_\beta^\alpha], \tag{13}$$

i.e. as the usual matrix-determinant<sup>3</sup> of the  $2 \times 2$  matrix  $[c_\beta^\alpha]$ . Since  $c_\beta^\alpha = a^{\alpha\gamma} c_{\gamma\beta}$ , the surface determinant can also be written as

$$\det_s \mathbf{c} := \det[a^{\alpha\beta}] \det[c_{\alpha\beta}] = \det[c_{\alpha\beta}] / \det[a_{\alpha\beta}]. \tag{14}$$

Note that this expression does not contain any summation on  $\alpha$  or  $\beta$ , since  $\det[\dots]$  is a scalar. The third tensor function is the surface inverse  $\mathbf{c}_s^{-1}$ , defined from

$$\mathbf{c}_s^{-1} \mathbf{c}_s = \mathbf{i}. \tag{15}$$

$\mathbf{c}_s^{-1}$  is a surface tensor with the contra-variant components

$$c_{\text{inv}}^{\alpha\beta} := \frac{1}{c} e^{\alpha\gamma} c_{\delta\gamma} e^{\beta\delta}, \quad c := \det[c_{\alpha\beta}], \tag{16}$$

since  $c_{\text{inv}}^{\alpha\beta} c_{\beta\gamma} = \delta_\gamma^\alpha$ . Here

$$[e^{\alpha\beta}] = \begin{bmatrix} 0 & 1 \\ -1 & 0 \end{bmatrix} \tag{17}$$

is the so-called unit alternator. In particular, (16) yields

$$a^{\alpha\beta} = \frac{1}{a} e^{\alpha\gamma} a_{\gamma\delta} e^{\beta\delta}, \quad a := \det[a_{\alpha\beta}]. \tag{18}$$

Note that in general  $\text{tr}_s \mathbf{c} \neq \text{tr} \mathbf{c}$ ,  $\det_s \mathbf{c} \neq \det \mathbf{c}$  and  $\mathbf{c}_s^{-1} \neq \mathbf{c}^{-1}$ . Multiplying (18) by  $a_{\alpha\beta}$ , one can further find

$$a = \frac{1}{2} e^{\alpha\gamma} e^{\beta\delta} a_{\alpha\beta} a_{\gamma\delta}. \tag{19}$$

### 3.3 Surface differentiation

The derivative encountered in (2) is called the *parametric derivative*. It is denoted by a comma. Taking another parametric derivative gives

$$\mathbf{a}_{\alpha,\beta} = \frac{\partial \mathbf{a}_\alpha}{\partial \xi^\beta} = \mathbf{x}_{,\alpha\beta}. \tag{20}$$

---

<sup>3</sup>Note that  $\det[c_\beta^\alpha] = \det[c_\beta^\alpha] = \det[c_\beta^\alpha]$  even if  $c_\beta^\alpha \neq c_\beta^\alpha$

Generally, vector  $\mathbf{a}_{\alpha,\beta}$  has both in-plane and out-of-plane components. But only the latter is needed in order to describe surface curvature. This motivates the introduction of another derivative, the so-called *co-variant derivative*. It is denoted by a semicolon. For basis vectors  $\mathbf{a}_\alpha$  and  $\mathbf{a}^\alpha$  it is defined by

$$\mathbf{a}_{\alpha;\beta} := (\mathbf{n} \otimes \mathbf{n}) \mathbf{a}_{\alpha,\beta} \quad (21)$$

and

$$\mathbf{a}^\alpha_{;\beta} := (\mathbf{n} \otimes \mathbf{n}) \mathbf{a}^\alpha_{,\beta}. \quad (22)$$

Using Eqs. (9) and (8), leads to

$$\mathbf{a}_{\alpha;\beta} = \mathbf{a}_{\alpha,\beta} - \Gamma_{\alpha\beta}^\gamma \mathbf{a}_\gamma \quad (23)$$

and

$$\mathbf{a}^\alpha_{;\beta} := \mathbf{a}^\alpha_{,\beta} + \Gamma_{\beta\gamma}^\alpha \mathbf{a}^\gamma. \quad (24)$$

where

$$\Gamma_{\alpha\beta}^\gamma := \mathbf{a}^\gamma \cdot \mathbf{a}_{\alpha,\beta} \quad (25)$$

are the so-called *Christoffel symbols*. For scalars  $\phi \in \mathbb{R}$  and general vectors  $\mathbf{v} \in \mathbb{R}^3$  (that are independent of the surface parameterization), such as the normal vector  $\mathbf{n}$ , the covariant derivative is defined to be equal to the parametric derivative. From (7) thus follow  $\mathbf{n}_{;\alpha} = \mathbf{n}_{,\alpha}$ ,  $v_{;\alpha} = v_{,\alpha}$ ,  $(v^\alpha \mathbf{a}_\alpha)_{;\beta} = (v^\alpha \mathbf{a}_\alpha)_{,\beta}$ ,  $(v_\alpha \mathbf{a}^\alpha)_{;\beta} = (v_\alpha \mathbf{a}^\alpha)_{,\beta}$ , and further

$$\begin{aligned} v_{\alpha;\beta} &= v_{\alpha,\beta} - \Gamma_{\alpha\beta}^\gamma v_\gamma, \\ v^\alpha_{;\beta} &= v^\alpha_{,\beta} + \Gamma_{\beta\gamma}^\alpha v^\gamma. \end{aligned} \quad (26)$$

In classical physics, the gradient, divergence and Laplacian are important differential operators. They can now be defined on the surface  $\mathcal{S}$ . The surface gradient of a scalar function  $\phi$  is defined through the regular gradient  $\nabla\phi$  as

$$\nabla_s \phi := \nabla\phi \cdot \mathbf{i}, \quad (27)$$

Inserting (8), gives  $\nabla_s \phi = \phi_{,\alpha} \mathbf{a}^\alpha$ . Likewise, the surface gradient for a vector function  $\mathbf{v}$  is defined as

$$\nabla_s \mathbf{v} := \nabla\mathbf{v} \cdot \mathbf{i}, \quad (28)$$

such that  $\nabla_s \mathbf{v} = \mathbf{v}_{,\alpha} \otimes \mathbf{a}^\alpha$ . The surface divergence follows from the gradient as

$$\text{div}_s \mathbf{v} := \text{tr} \nabla_s \mathbf{v}. \quad (29)$$

i.e.  $\text{div}_s \mathbf{v} = \mathbf{v}_{,\alpha} \cdot \mathbf{a}^\alpha$ . The surface Laplacian of a scalar  $\phi$  is then defined by

$$\Delta_s \phi := \text{div}_s \nabla_s \phi, \quad (30)$$

which leads to  $\Delta_s \phi = \phi_{;\alpha\beta} a^{\alpha\beta}$ . In the above expressions  $\phi_{;\alpha} = \phi_{,\alpha}$  and  $\mathbf{v}_{;\alpha} = \mathbf{v}_{,\alpha}$ . However,  $\phi_{;\alpha\beta} \neq \phi_{,\alpha\beta}$ . Instead

$$\phi_{;\alpha\beta} = \phi_{,\alpha\beta} - \Gamma_{\alpha\beta}^\gamma \phi_{,\gamma}. \quad (31)$$

### 3.4 Surface curvature

The surface curvature is characterized by the normal component of  $\mathbf{a}_{\alpha;\beta}$ , i.e. by the four numbers

$$b_{\alpha\beta} := \mathbf{n} \cdot \mathbf{a}_{\alpha;\beta} = \mathbf{n} \cdot \mathbf{a}_{\alpha;\beta}. \quad (32)$$

They are known as the co-variant components of the *curvature tensor*  $\mathbf{b} = b_{\alpha\beta} \mathbf{a}^\alpha \otimes \mathbf{a}^\beta$ . The curvature tensor is a surface tensor like  $\mathbf{i}$  and  $\mathbf{c}_s$ . It is symmetric and has the mixed components  $b_\beta^\alpha = a^{\alpha\gamma} b_{\gamma\beta}$  and the contra-variant components  $b^{\alpha\beta} = b_\gamma^\alpha a^{\gamma\beta}$ . It appears in the formulas of Gauss,

$$\mathbf{a}_{\alpha;\beta} = b_{\alpha\beta} \mathbf{n}, \quad (33)$$

and Weingarten,

$$\mathbf{n}_{,\alpha} = -b_\alpha^\beta \mathbf{a}_\beta. \quad (34)$$

Its two invariants

$$H := \frac{1}{2} \text{tr}_s \mathbf{b} \quad (35)$$

and

$$\kappa := \det_s \mathbf{b} \quad (36)$$

are known as the mean curvature and Gaussian curvature of surface  $\mathcal{S}$ . According to Sec. 3.2, those can also be written as  $H = \frac{1}{2} b_\alpha^\alpha = \frac{1}{2} a^{\alpha\beta} b_{\alpha\beta}$  and  $\kappa = b/a$ , where  $b := \det[b_{\alpha\beta}]$  and  $a := \det[a_{\alpha\beta}]$ . The eigenvalues of  $\mathbf{b}$ ,

$$\kappa_{1/2} = H \pm \sqrt{H^2 - \kappa}, \quad (37)$$

are the principal curvatures of  $\mathcal{S}$ . Note that  $2H = \kappa_1 + \kappa_2$  and  $\kappa = \kappa_1 \kappa_2$ . Using (7) and Weingarten's formula, the surface divergence of vector  $\mathbf{v}$  can also be written as

$$\text{div}_s \mathbf{v} = v_{;\alpha}^\alpha - 2Hv. \quad (38)$$

### 3.5 Surface Cayley-Hamilton

According to the surface Cayley-Hamilton theorem, a tensor  $\mathbf{c}$  satisfies the identity

$$c_\gamma^\alpha a^{\alpha\beta} - c^{\alpha\beta} = \tilde{c}^{\alpha\beta}, \quad (39)$$

where  $\tilde{c}^{\alpha\beta} := \frac{c}{a} c_{\text{inv}}^{\alpha\beta}$  are the contra-variant components of the adjugate tensor of  $\mathbf{c}$ . For the curvature tensor in particular, the Cayley-Hamilton-theorem becomes

$$2H a^{\alpha\beta} - b^{\alpha\beta} = \kappa b_{\text{inv}}^{\alpha\beta}. \quad (40)$$

Multiplying this by  $b_\beta^\gamma$  gives

$$b^{\alpha\gamma} b_\gamma^\beta = 2H b^{\alpha\beta} - \kappa a^{\alpha\beta}. \quad (41)$$

Lowering indices with  $a_{\alpha\beta}$ , then gives

$$b_\alpha^\gamma b_{\gamma\beta} = 2H b_{\alpha\beta} - \kappa a_{\alpha\beta}. \quad (42)$$

## 4 Surface kinematics

This section discusses the kinematics of deforming surfaces and examines its consequences. Important kinematical objects are the surface strain tensor (Sec. 4.1), the surface velocity gradient (Sec. 4.2) and the area-incompressibility constraint (Sec. 4.3). For the subsequent developments, all kinematical objects need to be varied (Sec. 4.4) and linearized (Sec. 4.5).

## 4.1 Surface deformation

In order to describe the deformation of surface  $\mathcal{S}$ , a reference configuration, denoted  $\mathcal{S}_0$ , is introduced. This could for example be a flat plane. But that is not a requirement. The only requirement for  $\mathcal{S}_0$  is that it is fixed in time. The reference surface  $\mathcal{S}_0$  can be described in the same form as  $\mathcal{S}$ . Therefore all the quantities introduced in Sec. 3 can be re-defined for  $\mathcal{S}_0$ . This is done by using upper-case letters, or adding subscript ‘0’. Surface  $\mathcal{S}_0$  is thus described by the mapping  $\mathbf{X} = \mathbf{X}(\xi^\alpha)$  and the tangent vectors  $\mathbf{A}_\alpha = \mathbf{X}_{,\alpha}$ , see Fig. 2. Further objects that follow in that fashion are  $A_{\alpha\beta}$ ,  $A^{\alpha\beta}$ ,  $\mathbf{N}$ ,  $\mathbf{A}_{\alpha,\beta}$  and so forth. In particular,

$$\mathbf{I} := \mathbf{A}_\alpha \otimes \mathbf{A}^\alpha = \mathbf{A}^\alpha \otimes \mathbf{A}_\alpha \quad (43)$$

denotes the surface identity tensor on  $\mathcal{S}_0$ , such that  $\mathbf{1} = \mathbf{I} + \mathbf{N} \otimes \mathbf{N}$ .

The mapping between  $\mathcal{S}_0$  and  $\mathcal{S}$ , denoted  $\mathbf{x} = \boldsymbol{\varphi}(\mathbf{X})$ , is characterized by the surface deformation gradient

$$\mathbf{F} := \mathbf{a}_\alpha \otimes \mathbf{A}^\alpha. \quad (44)$$

and the surface stretch

$$J := \frac{J_a}{J_A} = \frac{\sqrt{\det[a_{\alpha\beta}]}}{\sqrt{\det[A_{\alpha\beta}]}}. \quad (45)$$

They relate differential line and area elements according to  $d\mathbf{x} = \mathbf{F} d\mathbf{X}$  and  $da = J dA$ . If the number of surface particles is conserved during deformation, as will be considered here<sup>4</sup>, then

$$\rho da = \rho_0 dA, \quad (46)$$

such that

$$J = \frac{\rho_0}{\rho}, \quad (47)$$

where  $\rho$  and  $\rho_0$  are the surface densities at  $\mathbf{x} \in \mathcal{S}$  and  $\mathbf{X} \in \mathcal{S}_0$ , respectively.

Two important objects for describing in-plane deformation, are the left and right surface Cauchy-Green tensors, given by

$$\begin{aligned} \mathbf{C} &:= \mathbf{F}^T \mathbf{F} = a_{\alpha\beta} \mathbf{A}^\alpha \otimes \mathbf{A}^\beta, \\ \mathbf{B} &:= \mathbf{F} \mathbf{F}^T = A^{\alpha\beta} \mathbf{a}_\alpha \otimes \mathbf{a}_\beta. \end{aligned} \quad (48)$$

$\mathbf{C}$  is a surface tensor on  $\mathcal{S}_0$ , while  $\mathbf{B}$  is a surface tensor on  $\mathcal{S}$ . Their trace  $I_1 := \text{tr } \mathbf{C} = \mathbf{I} : \mathbf{C} = \text{tr } \mathbf{B} = \mathbf{i} : \mathbf{B}$  is equal to

$$I_1 = A^{\alpha\beta} a_{\alpha\beta}. \quad (49)$$

From  $\mathbf{C}$  follows the surface Green-Lagrange strain tensor

$$\mathbf{E} := (\mathbf{C} - \mathbf{I})/2. \quad (50)$$

Its surface components are

$$E_{\alpha\beta} := (a_{\alpha\beta} - A_{\alpha\beta})/2, \quad (51)$$

such that  $\mathbf{E} = E_{\alpha\beta} \mathbf{A}^\alpha \otimes \mathbf{A}^\beta$ . Likewise, the relative curvature tensor  $\mathbf{K} = K_{\alpha\beta} \mathbf{A}^\alpha \otimes \mathbf{A}^\beta$ , with the components

$$K_{\alpha\beta} := b_{\alpha\beta} - B_{\alpha\beta}, \quad (52)$$

is defined. It is an important object for describing bending.

<sup>4</sup>For an extension to changing mass, e.g. due to protein binding, see [Sahu et al. \(2017\)](#).

## 4.2 Surface motion

In general, the deformation of the surface is time-dependent. The consequences of this on the surface description and kinematics are discussed here. The velocity of a surface particle (e.g. a lipid molecule) at  $\mathbf{x} \in \mathcal{S}$ , is  $\mathbf{v} = \dot{\mathbf{x}}$ , where the notation

$$(\dot{\dots}) := \frac{D\dots}{Dt} := \frac{\partial\dots}{\partial t} \Big|_{\mathbf{X}=\text{fixed}} \quad (53)$$

denotes the so-called *material time derivative*. The time derivative of the tangent vectors and their parametric derivatives then follow as  $\dot{\mathbf{a}}_\alpha = \dot{\mathbf{x}}_{,\alpha} = \mathbf{v}_{,\alpha}$  and  $\dot{\mathbf{a}}_{\alpha,\beta} = \dot{\mathbf{x}}_{,\alpha\beta} = \mathbf{v}_{,\alpha\beta}$ . This then leads to

$$\dot{a}_{\alpha\beta} = \mathbf{a}_\alpha \cdot \dot{\mathbf{a}}_\beta + \dot{\mathbf{a}}_\alpha \cdot \mathbf{a}_\beta \quad (54)$$

and

$$\dot{b}_{\alpha\beta} = \mathbf{a}_{\alpha,\beta} \cdot \dot{\mathbf{n}} + \mathbf{n} \cdot \dot{\mathbf{a}}_{\alpha,\beta}. \quad (55)$$

Taking a time derivative of  $\mathbf{n} \cdot \mathbf{n} = 1$  and  $\mathbf{n} \cdot \mathbf{a}_\alpha = 0$ , one can find

$$\dot{\mathbf{n}} = -(\mathbf{a}^\alpha \otimes \mathbf{n}) \dot{\mathbf{a}}_\alpha = -\mathbf{a}^\alpha (\mathbf{n} \cdot \dot{\mathbf{a}}_\alpha), \quad (56)$$

such that

$$\dot{b}_{\alpha\beta} = (\dot{\mathbf{a}}_{\alpha,\beta} - \Gamma_{\alpha\beta}^\gamma \dot{\mathbf{a}}_\gamma) \cdot \mathbf{n}. \quad (57)$$

Taking a time derivative of (4) and  $\mathbf{n} \cdot \mathbf{a}^\alpha = 0$ , one can find

$$\dot{\mathbf{a}}^\alpha = (a^{\alpha\beta} \mathbf{n} \otimes \mathbf{n} - \mathbf{a}^\beta \otimes \mathbf{a}^\alpha) \dot{\mathbf{a}}_\beta. \quad (58)$$

From (19) follows

$$\dot{a} = a a^{\alpha\beta} \dot{a}_{\alpha\beta}, \quad (59)$$

and therefore

$$\dot{j} = \frac{\partial J}{\partial a_{\alpha\beta}} \dot{a}_{\alpha\beta} = \frac{J}{2} a^{\alpha\beta} \dot{a}_{\alpha\beta}. \quad (60)$$

From (18) follows

$$\dot{a}^{\alpha\beta} = a^{\alpha\beta\gamma\delta} \dot{a}_{\gamma\delta}, \quad (61)$$

with

$$a^{\alpha\beta\gamma\delta} := \frac{\partial a^{\alpha\beta}}{\partial a_{\gamma\delta}} = \frac{1}{2a} (e^{\alpha\gamma} e^{\beta\delta} + e^{\alpha\delta} e^{\beta\gamma}) - a^{\alpha\beta} a^{\gamma\delta}. \quad (62)$$

A component-wise comparison shows that

$$a^{\alpha\beta\gamma\delta} = -\frac{1}{2} (a^{\alpha\gamma} a^{\beta\delta} + a^{\alpha\delta} a^{\beta\gamma}), \quad (63)$$

i.e.  $a^{\alpha\beta\gamma\delta}$  corresponds to the contra-variant components of a fourth order identity tensor: Contracting  $a^{\alpha\beta\gamma\delta}$  with any symmetric tensor with components  $c_{\gamma\delta}$ , yields

$$a^{\alpha\beta\gamma\delta} c_{\gamma\delta} = -c^{\alpha\beta}. \quad (64)$$

It is noted that  $a^{\alpha\beta\gamma\delta}$  has major and minor symmetries. Given  $a^{\alpha\beta\gamma\delta}$ , Eq. (61) turns into

$$\dot{a}^{\alpha\beta} = -a^{\alpha\gamma} a^{\beta\delta} \dot{a}_{\gamma\delta}. \quad (65)$$

An important object for fluids is the symmetric surface velocity gradient

$$\mathbf{d} := (\mathbf{v}_{,\alpha} \otimes \mathbf{a}^\alpha + \mathbf{a}^\alpha \otimes \mathbf{v}_{,\alpha})/2. \quad (66)$$

Its co-variant and contra-variant components, according to (11), simply are  $d_{\alpha\beta} = \dot{a}_{\alpha\beta}/2$  and  $d^{\alpha\beta} = -\dot{a}^{\alpha\beta}/2$ . In terms of the velocity components  $v_\alpha := \mathbf{v} \cdot \mathbf{a}_\alpha$  and  $v := \mathbf{v} \cdot \mathbf{n}$ , also  $d^{\alpha\beta} = a^{\alpha\gamma} a^{\beta\delta} (v_{\gamma;\delta} + v_{\delta;\gamma})/2 - v b^{\alpha\beta}$  holds.

The time derivative of the mean curvature yields

$$\dot{H} = \frac{1}{2} \dot{a}^{\alpha\beta} b_{\alpha\beta} + \frac{1}{2} a^{\alpha\beta} \dot{b}_{\alpha\beta}. \quad (67)$$

Using Eqs. (61) and (64) gives

$$\dot{H} = \frac{\partial H}{\partial a_{\alpha\beta}} \dot{a}_{\alpha\beta} + \frac{\partial H}{\partial b_{\alpha\beta}} \dot{b}_{\alpha\beta}, \quad (68)$$

with

$$\begin{aligned} \frac{\partial H}{\partial a_{\alpha\beta}} &= -\frac{1}{2} b^{\alpha\beta}, \\ \frac{\partial H}{\partial b_{\alpha\beta}} &= \frac{1}{2} a^{\alpha\beta}. \end{aligned} \quad (69)$$

Analogously, the change of the Gaussian curvature is

$$\dot{\kappa} = \frac{\partial \kappa}{\partial a_{\alpha\beta}} \dot{a}_{\alpha\beta} + \frac{\partial \kappa}{\partial b_{\alpha\beta}} \dot{b}_{\alpha\beta}, \quad (70)$$

with

$$\begin{aligned} \frac{\partial \kappa}{\partial a_{\alpha\beta}} &= -\kappa a^{\alpha\beta}, \\ \frac{\partial \kappa}{\partial b_{\alpha\beta}} &= \kappa b_{\text{inv}}^{\alpha\beta} = \tilde{b}^{\alpha\beta}. \end{aligned} \quad (71)$$

e.g. see [Sauer and Duong \(2017\)](#).

The last object of interest is  $\dot{b}^{\alpha\beta}$ . Taking the time derivative of  $b^{\alpha\beta} = b_{\gamma\delta} a^{\gamma\alpha} a^{\delta\beta}$  yields

$$\dot{b}^{\alpha\beta} = \frac{\partial b^{\alpha\beta}}{\partial a_{\gamma\delta}} \dot{a}_{\gamma\delta} + \frac{\partial b^{\alpha\beta}}{\partial b_{\gamma\delta}} \dot{b}_{\gamma\delta}, \quad (72)$$

with

$$\begin{aligned} \frac{\partial b^{\alpha\beta}}{\partial a_{\gamma\delta}} &= b^{\alpha\beta\gamma\delta}, \\ \frac{\partial b^{\alpha\beta}}{\partial b_{\gamma\delta}} &= -a^{\alpha\beta\gamma\delta}, \end{aligned} \quad (73)$$

and

$$b^{\alpha\beta\gamma\delta} := -\frac{1}{2} \left( a^{\alpha\gamma} b^{\beta\delta} + b^{\alpha\gamma} a^{\beta\delta} + a^{\alpha\delta} b^{\beta\gamma} + b^{\alpha\delta} a^{\beta\gamma} \right) \quad (74)$$

([Sauer and Duong, 2017](#)). From a component-wise comparison, it can be shown that  $b^{\alpha\beta\gamma\delta}$  is also equal to

$$b^{\alpha\beta\gamma\delta} = 2H (a^{\alpha\beta} a^{\gamma\delta} + a^{\alpha\beta\gamma\delta}) - (a^{\alpha\beta} b^{\gamma\delta} + b^{\alpha\beta} a^{\gamma\delta}). \quad (75)$$

### 4.3 Surface incompressibility

An important constraint on the surface motion is surface- (or area-) incompressibility. During such motion

$$g := J - 1 = 0 \quad \forall t, \quad (76)$$

such that  $\dot{J} = 0$ . From (60) and (54) follows that area-incompressibility implies

$$\dot{\mathbf{a}}_\alpha \cdot \mathbf{a}^\alpha = 0, \quad (77)$$

which is equivalent to

$$\operatorname{div}_s \mathbf{v} = 0. \quad (78)$$

### 4.4 Surface variation

In order to derive the weak form, which is essential for the finite element method, the variation of several kinematical quantities is required. Therefore, a variation of position  $\mathbf{x} \in \mathcal{S}$  by the amount  $\delta \mathbf{x}$  is considered, and the effect on various kinematical quantities is examined. The variation of the tangent vectors and its parametric derivative are  $\delta \mathbf{a}_\alpha = \delta \mathbf{x}_{,\alpha}$  and  $\delta \mathbf{a}_{\alpha,\beta} = \delta \mathbf{x}_{,\alpha\beta}$ . Since the variation follows the laws of differentiation,  $\delta(\dots)$  has the same format as  $(\dots)$ , and one can immediately extract the expressions for  $\delta a_{\alpha\beta}$ ,  $\delta b_{\alpha\beta}$ ,  $\delta \mathbf{n}$ ,  $\delta \mathbf{a}^\alpha$ ,  $\delta J$ ,  $\delta H$ ,  $\delta \kappa$ ,  $\delta a^{\alpha\beta}$  and  $\delta b^{\alpha\beta}$  from the preceding section. In particular,

$$\delta a_{\alpha\beta} = \mathbf{a}_\alpha \cdot \delta \mathbf{a}_\beta + \delta \mathbf{a}_\alpha \cdot \mathbf{a}_\beta \quad (79)$$

$$\delta b_{\alpha\beta} = \mathbf{a}_{\alpha,\beta} \cdot \delta \mathbf{n} + \mathbf{n} \cdot \delta \mathbf{a}_{\alpha,\beta} \quad (80)$$

or

$$\delta b_{\alpha\beta} = (\delta \mathbf{a}_{\alpha,\beta} - \Gamma_{\alpha\beta}^\gamma \delta \mathbf{a}_\gamma) \cdot \mathbf{n} \quad (81)$$

and

$$\delta \mathbf{n} = -(\mathbf{a}^\alpha \otimes \mathbf{n}) \delta \mathbf{a}_\alpha. \quad (82)$$

### 4.5 Surface linearization

In order to employ Newton's method, as is considered for the solution of the resulting finite element equations, the weak form needs to be linearized w.r.t. configuration  $\mathbf{x}$ . Therefore an increment  $\Delta \mathbf{x}$  is considered and its effect on the system is examined. The change of  $\mathbf{a}_\alpha$  and  $\mathbf{a}_{\alpha,\beta}$ , due to  $\Delta \mathbf{x}$ , thus is  $\Delta \mathbf{a}_\alpha = \Delta \mathbf{x}_{,\alpha}$  and  $\Delta \mathbf{a}_{\alpha,\beta} = \Delta \mathbf{x}_{,\alpha\beta}$ . Since the linearization follows the laws of differentiation,  $\Delta(\dots)$  has the same format as  $(\dots)$ , and one can immediately extract the expressions for  $\Delta a_{\alpha\beta}$ ,  $\Delta b_{\alpha\beta}$ ,  $\Delta \mathbf{n}$ ,  $\Delta \mathbf{a}^\alpha$ ,  $\Delta J$ ,  $\Delta H$ ,  $\Delta \kappa$ ,  $\Delta a^{\alpha\beta}$  and  $\Delta b^{\alpha\beta}$  from Sec. 4.2. Since linearization follows after variation, the variations that still depend on  $\mathbf{x}$  (instead of just depending on  $\delta \mathbf{x}$ ), also need to be linearized. Linearizing (79) and (80), gives

$$\begin{aligned} \Delta \delta a_{\alpha\beta} &= \delta \mathbf{a}_\alpha \cdot \Delta \mathbf{a}_\beta + \delta \mathbf{a}_\beta \cdot \Delta \mathbf{a}_\alpha, \\ \Delta \delta b_{\alpha\beta} &= \delta \mathbf{a}_{\alpha,\beta} \cdot \Delta \mathbf{n} + \delta \mathbf{n} \cdot \Delta \mathbf{a}_{\alpha,\beta} + \mathbf{a}_{\alpha,\beta} \cdot \Delta \delta \mathbf{n}. \end{aligned} \quad (83)$$

From (82) and (58) follows

$$\Delta \delta \mathbf{n} = -(\delta \mathbf{a}_\alpha \cdot \mathbf{n})(\mathbf{n} \cdot \Delta \mathbf{a}_\beta) \mathbf{a}^{\alpha\beta} \mathbf{n} + (\delta \mathbf{a}_\alpha \cdot \mathbf{n})(\mathbf{a}^\alpha \cdot \Delta \mathbf{a}_\beta) \mathbf{a}^\beta + (\delta \mathbf{a}_\alpha \cdot \mathbf{a}^\beta)(\mathbf{n} \cdot \Delta \mathbf{a}_\beta) \mathbf{a}^\alpha, \quad (84)$$

such that

$$\mathbf{a}_{\alpha,\beta} \cdot \Delta \delta \mathbf{n} = \delta \mathbf{a}_\gamma \cdot (\Gamma_{\alpha\beta}^\gamma \mathbf{a}^\delta \otimes \mathbf{n} + \Gamma_{\alpha\beta}^\delta \mathbf{n} \otimes \mathbf{a}^\gamma - a^{\gamma\delta} b_{\alpha\beta} \mathbf{n} \otimes \mathbf{n}) \Delta \mathbf{a}_\delta. \quad (85)$$

Inserting (85) into (83) and using (82), then gives

$$\begin{aligned} \Delta \delta b_{\alpha\beta} &= -\delta \mathbf{a}_\gamma \cdot (\mathbf{n} \otimes \mathbf{a}^\gamma) \Delta \mathbf{a}_{\alpha,\beta} - \delta \mathbf{a}_{\alpha,\beta} \cdot (\mathbf{a}^\gamma \otimes \mathbf{n}) \Delta \mathbf{a}_\gamma \\ &+ \delta \mathbf{a}_\gamma \cdot (\Gamma_{\alpha\beta}^\gamma \mathbf{a}^\delta \otimes \mathbf{n} + \Gamma_{\alpha\beta}^\delta \mathbf{n} \otimes \mathbf{a}^\gamma - a^{\gamma\delta} b_{\alpha\beta} \mathbf{n} \otimes \mathbf{n}) \Delta \mathbf{a}_\delta. \end{aligned} \quad (86)$$

Note that all these expressions are symmetric w.r.t. linearization and variation.

## 5 Surface balance

This section presents the mechanical balance laws for shells. The sectional forces and sectional moments are introduced (Sec. 5.1), and then linear momentum (Sec. 5.2), angular momentum (Sec. 5.3) and mechanical power (Sec. 5.5) are discussed. Sec. 5.4 discusses boundary moments. The presentation follows [Sauer and Duong \(2017\)](#).

### 5.1 Sectional forces and moments

Consider an infinitesimal surface element  $da \subset \mathcal{S}$ , located at  $\mathbf{x}$  and aligned along  $\mathbf{a}_1$  and  $\mathbf{a}_2$  as is shown in Fig. 3. On the cut surfaces the distributed<sup>5</sup> sectional force and moment components  $N^{\alpha\beta}$ ,  $S^\alpha$  and  $M^{\alpha\beta}$  are defined as shown. The sectional forces are collected in the stress tensor

$$\boldsymbol{\sigma} := N^{\alpha\beta} \mathbf{a}_\alpha \otimes \mathbf{a}_\beta + S^\alpha \mathbf{a}_\alpha \otimes \mathbf{n}, \quad (87)$$

such that the traction vector on the cut normal to  $\boldsymbol{\nu}$  is given through Cauchy's formula

$$\mathbf{T} := \boldsymbol{\sigma}^T \boldsymbol{\nu}. \quad (88)$$

With  $\boldsymbol{\nu} = \nu_\alpha \mathbf{a}^\alpha$  one can write  $\mathbf{T} = \mathbf{T}^\alpha \nu_\alpha$ , where

$$\mathbf{T}^\alpha := \boldsymbol{\sigma}^T \mathbf{a}^\alpha = N^{\alpha\beta} \mathbf{a}_\beta + S^\alpha \mathbf{n}, \quad (89)$$

are then the tractions defined on the face normal to  $\mathbf{a}^\alpha$ , see Fig. 3.

The distributed section moments are collected in the moment tensor

$$\boldsymbol{\mu} := -M^{\alpha\beta} \mathbf{a}_\alpha \otimes \mathbf{a}_\beta, \quad (90)$$

such that one can define the distributed moment vector

$$\mathbf{M} := \boldsymbol{\mu}^T \boldsymbol{\nu} \quad (91)$$

on the cut normal to  $\boldsymbol{\nu}$ . Similar to before, one can write

$$\mathbf{M} = \mathbf{M}^\alpha \nu_\alpha, \quad (92)$$

with

$$\mathbf{M}^\alpha := \boldsymbol{\mu}^T \mathbf{a}^\alpha = -M^{\alpha\beta} \mathbf{a}_\beta. \quad (93)$$

---

<sup>5</sup>per current length of the cut face

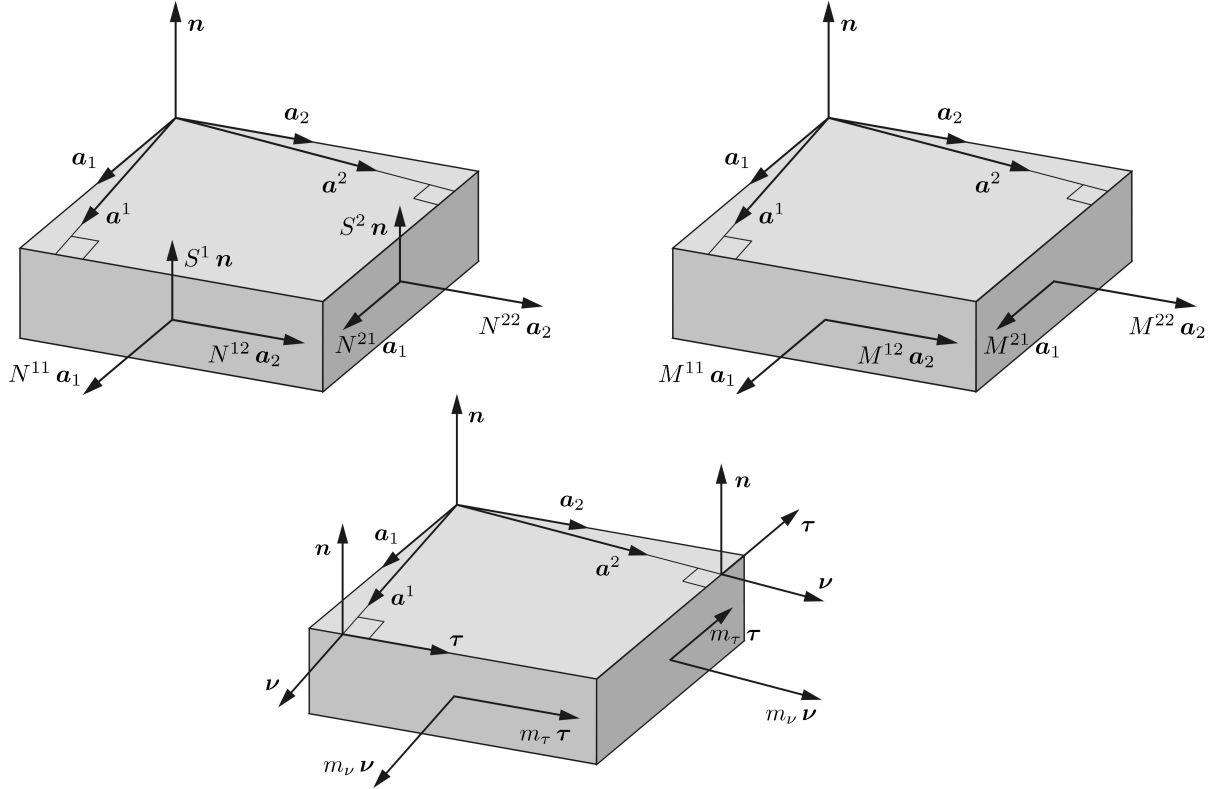


Figure 3: Sectional forces and moments (Sauer and Duong, 2017): Components of the traction and moment vectors  $\mathbf{T}^1$ ,  $\mathbf{T}^2$ ,  $\mathbf{M}^1$  and  $\mathbf{M}^2$  defined on the faces normal to  $\mathbf{a}^1$  and  $\mathbf{a}^2$  (top). Components of the physical moment vector  $\mathbf{m}$  acting on the same faces (bottom).

The components of  $-\mathbf{M}^\alpha$  are shown in the top right inset of Fig. 3. Vector  $\mathbf{M}$  can be associated with a force couple (Sahu et al., 2017). The moment vector physically acting on the element is given by the quantity

$$\mathbf{m} := \mathbf{n} \times \mathbf{M}. \quad (94)$$

Inserting (92) and (93), and using the identity

$$\mathbf{a}_\beta \times \mathbf{n} = \tau_\beta \boldsymbol{\nu} - \nu_\beta \boldsymbol{\tau}, \quad (95)$$

gives

$$\mathbf{m} = m_\nu \boldsymbol{\nu} + m_\tau \boldsymbol{\tau} \quad (96)$$

with the local Cartesian components

$$\begin{aligned} m_\nu &:= M^{\alpha\beta} \nu_\alpha \tau_\beta, \\ m_\tau &:= -M^{\alpha\beta} \nu_\alpha \nu_\beta. \end{aligned} \quad (97)$$

The vector  $\mathbf{M}$  can then also be written as

$$\mathbf{M} = m_\tau \boldsymbol{\nu} - m_\nu \boldsymbol{\tau}. \quad (98)$$

The bottom inset of Fig. 3 shows the vector  $\mathbf{m}$  acting on faces  $\mathbf{a}^\alpha$ .

## 5.2 Balance of linear momentum

Consider a part of the surface  $\mathcal{S}$ , denoted  $\mathcal{R}$  that is assumed to have a smooth boundary  $\partial\mathcal{R}$ . The ‘body’ force (per current surface area) acting on  $\mathcal{R}$  is denoted by  $\mathbf{f}$ . For every such surface part, the change of its linear momentum is equal to the external forces acting on it, i.e.

$$\frac{D}{Dt} \int_{\mathcal{R}} \rho \mathbf{v} \, da = \int_{\mathcal{R}} \mathbf{f} \, da + \int_{\partial\mathcal{R}} \mathbf{T} \, ds \quad \forall \mathcal{R} \subset \mathcal{S}. \quad (99)$$

Here,  $D/Dt$  denotes the material time derivative introduced in (53), and  $\mathbf{v}$  is the material velocity at  $\mathbf{x}$ . From the local conservation of mass (46) and the surface divergence theorem

$$\int_{\partial\mathcal{R}} \mathbf{T}^\alpha \nu_\alpha \, ds = \int_{\mathcal{R}} \mathbf{T}^\alpha_{;\alpha} \, da, \quad (100)$$

immediately follows the local form of (99),

$$\mathbf{T}^\alpha_{;\alpha} + \mathbf{f} = \rho \dot{\mathbf{v}} \quad \forall \mathbf{x} \in \mathcal{S}, \quad (101)$$

which is the strong form equilibrium equation at  $\mathbf{x} \in \mathcal{S}$ . If desired, it can be decomposed into in-plane and out-of-plane contributions (Jenkins, 1977; Sauer and Duong, 2017).

## 5.3 Balance of angular momentum

For every surface part  $\mathcal{R} \subset \mathcal{S}$ , the change of angular momentum is equal to the moment of the external forces, i.e.

$$\frac{D}{Dt} \int_{\mathcal{R}} \rho \mathbf{x} \times \mathbf{v} \, da = \int_{\mathcal{R}} \mathbf{x} \times \mathbf{f} \, da + \int_{\partial\mathcal{R}} \mathbf{x} \times \mathbf{T} \, ds + \int_{\partial\mathcal{R}} \mathbf{m} \, ds \quad \forall \mathcal{R} \subset \mathcal{S}. \quad (102)$$

Sauer and Duong (2017) show that this is satisfied if and only if

$$\sigma^{\alpha\beta} := N^{\alpha\beta} - b_\gamma^\beta M^{\gamma\alpha} \quad (103)$$

is symmetric and

$$S^\alpha = -M^{\beta\alpha}_{;\beta}. \quad (104)$$

The last equation expresses the well known Kirchhoff-Love result that the out-of-plane shear component follows as the derivative of the bending moments. It turns out that apart from  $\sigma^{\alpha\beta}$  also  $M^{\alpha\beta}$  is symmetric, see Sec. 6.2. According to relation (103), the in-plane stress component

$$N^{\alpha\beta} = \sigma^{\alpha\beta} + b_\gamma^\beta M^{\gamma\alpha} \quad (105)$$

is influenced by bending, and consequently  $N^{\alpha\beta}$  is generally non-symmetric.

## 5.4 Boundary conditions

At the boundary of the surface,  $\partial\mathcal{S}$ , the boundary conditions

$$\begin{aligned} \mathbf{x} &= \bar{\varphi} & \text{on } \partial_x \mathcal{S}, \\ \mathbf{t} &= \bar{\mathbf{t}} & \text{on } \partial_t \mathcal{S}, \\ m_\tau &= \bar{m}_\tau & \text{on } \partial_m \mathcal{S} \end{aligned} \quad (106)$$

can be prescribed. Here,  $m_\tau$  is the bending moment component parallel to boundary  $\partial\mathcal{S}$ . For Kirchhoff-Love shells, bending moments perpendicular to boundary  $\partial\mathcal{S}$ , denoted  $m_\nu$ , affect the boundary traction. Therefore the effective traction

$$\mathbf{t} := \mathbf{T} - (m_\nu \mathbf{n})' \quad (107)$$

is introduced, e.g. see Sauer and Duong (2017). In the following examples,  $m_\nu = 0$  is considered.

## 5.5 Mechanical power balance

The mechanical power balance follows from equilibrium. Contracting the equilibrium equation (101) with the velocity  $\mathbf{v}$  and integrating over  $\mathcal{R} \subset \mathcal{S}$ , gives

$$\int_{\mathcal{R}} \mathbf{v} \cdot (\mathbf{T}_{;\alpha}^\alpha + \mathbf{f} - \rho \dot{\mathbf{v}}) da = 0 \quad \forall \mathcal{R} \subset \mathcal{S}. \quad (108)$$

In here, the last term corresponds to the change of the kinetic energy

$$K := \frac{1}{2} \int_{\mathcal{R}} \rho \mathbf{v} \cdot \mathbf{v} da, \quad (109)$$

which, due to mass conservation, is given by

$$\dot{K} := \int_{\mathcal{R}} \rho \mathbf{v} \cdot \dot{\mathbf{v}} da. \quad (110)$$

Applying the surface divergence theorem to the first term, rearranging terms and applying the surface divergence theorem again, leads to the mechanical power balance (Sauer and Duong, 2017)

$$\dot{K} + P_{\text{int}} = P_{\text{ext}} \quad \forall \mathcal{R} \subset \mathcal{S}, \quad (111)$$

where

$$P_{\text{int}} = \frac{1}{2} \int_{\mathcal{R}} \sigma^{\alpha\beta} \dot{a}_{\alpha\beta} da + \int_{\mathcal{R}} M^{\alpha\beta} \dot{b}_{\alpha\beta} da \quad (112)$$

is the interal stress power of  $\mathcal{R}$  and

$$P_{\text{ext}} = \int_{\mathcal{R}} \mathbf{v} \cdot \mathbf{f} da + \int_{\partial\mathcal{R}} \mathbf{v} \cdot \mathbf{T} ds + \int_{\partial\mathcal{R}} \dot{\mathbf{n}} \cdot \mathbf{M} ds \quad (113)$$

is the power of the external forces acting on  $\mathcal{R}$  and  $\partial\mathcal{R}$ . Using definition (107),  $P_{\text{ext}}$  can be rewritten into (Sauer and Duong, 2017)

$$P_{\text{ext}} = \int_{\mathcal{R}} \mathbf{v} \cdot \mathbf{f} da + \int_{\partial\mathcal{R}} (\mathbf{v} \cdot \mathbf{t} + \dot{\mathbf{n}} \cdot m_\tau \boldsymbol{\nu}) ds + [\mathbf{v} \cdot m_\nu \mathbf{n}], \quad (114)$$

where the last term denotes the power of the point loads  $m_\nu \mathbf{n}$  that are present at corners of boundary  $\partial\mathcal{R}$ . For smooth boundaries, or for  $m_\nu = 0$ , the last term vanishes.

The derivation of the weak form of Eq. (101), considered in Sec. 8, is analogous to the derivation of the mechanical power balance.

## 6 Surface constitution

This section discusses the constitutive framework of lipid bilayers, accounting for elastic bending, (near-) area-incompressibility and viscous shear. The framework follows from the dissipation inequality (Sec. 6.1) using classical thermodynamical arguments (Sec. 6.2). For later use, linearization (Sec. 6.3) and stability (Sec. 6.4) are also discussed briefly.

## 6.1 Dissipation inequality

The local power density  $\sigma^{\alpha\beta} \dot{a}_{\alpha\beta}/2 + M^{\alpha\beta} \dot{b}_{\alpha\beta}$ , appearing within (112), also appears in the mechanical dissipation inequality

$$\mathcal{D} := \frac{1}{2} \sigma^{\alpha\beta} \dot{a}_{\alpha\beta} + M^{\alpha\beta} \dot{b}_{\alpha\beta} - \rho \dot{T}s - \rho \dot{\psi} \geq 0, \quad (115)$$

where  $T$  is the temperature,  $s$  is specific entropy, and  $\psi$  is the specific Helmholtz free energy (per unit mass). (115) is a consequence of the second law of thermodynamics for surfaces, e.g. see Sahu et al. (2017). Under isothermal conditions, considered here, the  $\rho \dot{T}s$  term vanishes. The dissipation  $\mathcal{D}$  has units of power per current area. Multiplying by  $J$ ,  $\mathcal{D}$  can be related to the reference area. Introducing

$$\begin{aligned} \tau^{\alpha\beta} &:= J \sigma^{\alpha\beta}, \\ M_0^{\alpha\beta} &:= J M^{\alpha\beta}, \end{aligned} \quad (116)$$

the isothermal dissipation inequality can thus be written as

$$\mathcal{D}_0 := \frac{1}{2} \tau^{\alpha\beta} \dot{a}_{\alpha\beta} + M_0^{\alpha\beta} \dot{b}_{\alpha\beta} - \dot{\Psi}_0 \geq 0, \quad (117)$$

where  $\Psi_0 := \rho_0 \psi$  is the Helmholtz free energy per reference area. Here, (47) and mass conservation have been used.

## 6.2 Constrained visco-elasticity

The free energy  $\Psi_0$  is a function of the deformation, which, for thin shells, is fully characterized by  $a_{\alpha\beta}$  and  $b_{\alpha\beta}$ . In order to account for constraints on  $a_{\alpha\beta}$ , such as area-incompressibility,  $\Psi_0$  is expressed as

$$\Psi_0 = \Psi_{0x} + \Psi_{0g}, \quad (118)$$

where

$$\Psi_{0x} = \Psi_{0x}(a_{\alpha\beta}, b_{\alpha\beta}) \quad (119)$$

denotes the contribution from deformation, and

$$\Psi_{0g} = q g(a_{\alpha\beta}) \quad (120)$$

denotes the contribution associated with a constraint  $g = 0$ .  $q$  denotes the Lagrange multiplier associated with the constraint. Applying chain rule then yields

$$\dot{\Psi}_0 = \frac{\partial \Psi_0}{\partial a_{\alpha\beta}} \dot{a}_{\alpha\beta} + \frac{\partial \Psi_0}{\partial b_{\alpha\beta}} \dot{b}_{\alpha\beta} + g \dot{q}, \quad (121)$$

so that (117) yields

$$\left( \frac{1}{2} \tau^{\alpha\beta} - \frac{\partial \Psi_0}{\partial a^{\alpha\beta}} \right) \dot{a}_{\alpha\beta} + \left( M_0^{\alpha\beta} - \frac{\partial \Psi_0}{\partial b^{\alpha\beta}} \right) \dot{b}_{\alpha\beta} - g \dot{q} \geq 0. \quad (122)$$

The surface stress  $\sigma^{\alpha\beta}$  is considered to contain elastic and viscous contributions in the form

$$\sigma^{\alpha\beta} = \sigma_{\text{elas}}^{\alpha\beta} + \sigma_{\text{visc}}^{\alpha\beta}. \quad (123)$$

The elastic contribution is independent of the rate  $\dot{a}_{\alpha\beta}$ , while the viscous contribution depends on the rate  $\dot{a}_{\alpha\beta}$  such that  $\dot{a}_{\alpha\beta} \rightarrow 0$  implies  $\sigma_{\text{visc}}^{\alpha\beta} \rightarrow 0$ . The moment  $M^{\alpha\beta}$  is considered to be purely elastic.

Since (122) applies to all thermodynamic processes (with general  $\dot{a}_{\alpha\beta}$ ,  $\dot{b}_{\alpha\beta}$  and  $\dot{q}$ ), the classical argument by Coleman and Noll (1964) (based on considering a set of special  $\dot{a}_{\alpha\beta}$ ,  $\dot{b}_{\alpha\beta}$  and  $\dot{q}$ ) leads to the constitutive equations

$$\begin{aligned}\sigma_{\text{elas}}^{\alpha\beta} &= \frac{2}{J} \frac{\partial \Psi_0}{\partial a_{\alpha\beta}}, \\ M^{\alpha\beta} &= \frac{1}{J} \frac{\partial \Psi_0}{\partial b_{\alpha\beta}}, \\ g &= 0, \\ \sigma_{\text{visc}}^{\alpha\beta} \dot{a}_{\alpha\beta} &\geq 0.\end{aligned}\tag{124}$$

The first two relations correspond to classical hyperelasticity, the third is just the constraint, and the fourth implies that viscous stresses are dissipative. A simple expression that satisfies this<sup>6</sup> is

$$\sigma_{\text{visc}}^{\alpha\beta} = -\eta \dot{a}^{\alpha\beta}.\tag{125}$$

where  $\eta \geq 0$  is a constant. Comparing to 3D fluids,  $\eta$  can be identified as the dynamic surface viscosity. An extension considering more general viscous stresses, as well as thermal fields and changing mass is provided by Sahu et al. (2017).

For the later developments, the variation of  $\Psi_0$  is required. Similar to (121), this can be written as

$$\delta \Psi_0 = \delta_x \Psi_0 + g \delta q,\tag{126}$$

with

$$\delta_x \Psi_0 := \frac{\partial \Psi_0}{\partial a_{\alpha\beta}} \delta a_{\alpha\beta} + \frac{\partial \Psi_0}{\partial b_{\alpha\beta}} \delta b_{\alpha\beta}.\tag{127}$$

From (124) follows

$$\delta_x \Psi_0 = \frac{1}{2} \tau^{\alpha\beta} \delta a_{\alpha\beta} + M_0^{\alpha\beta} \delta b_{\alpha\beta}.\tag{128}$$

If no constraint is present  $q$  and  $\delta q$  are zero.

### 6.3 Linearization of $\delta \Psi_0$

Linearizing (126), gives

$$\Delta \delta \Psi_0 = \Delta_x \delta_x \Psi_0 + \delta g \Delta q + \delta q \Delta g,\tag{129}$$

with

$$\delta g = \frac{\partial g}{\partial a_{\alpha\beta}} \delta a_{\alpha\beta}, \quad \Delta g = \frac{\partial g}{\partial a_{\alpha\beta}} \Delta a_{\alpha\beta},\tag{130}$$

and

$$\begin{aligned}\Delta_x \delta_x \Psi_0 &= \delta a_{\alpha\beta} \frac{\partial^2 \Psi_0}{\partial a_{\alpha\beta} \partial a_{\gamma\delta}} \Delta a_{\gamma\delta} + \delta a_{\alpha\beta} \frac{\partial^2 \Psi_0}{\partial a_{\alpha\beta} \partial b_{\gamma\delta}} \Delta b_{\gamma\delta} + \frac{\partial \Psi_0}{\partial a_{\alpha\beta}} \Delta \delta a_{\alpha\beta} \\ &+ \delta b_{\alpha\beta} \frac{\partial^2 \Psi_0}{\partial b_{\alpha\beta} \partial a_{\gamma\delta}} \Delta a_{\gamma\delta} + \delta b_{\alpha\beta} \frac{\partial^2 \Psi_0}{\partial b_{\alpha\beta} \partial b_{\gamma\delta}} \Delta b_{\gamma\delta} + \frac{\partial \Psi_0}{\partial b_{\alpha\beta}} \Delta \delta b_{\alpha\beta}.\end{aligned}\tag{131}$$

<sup>6</sup>Since  $\sigma_{\text{visc}}^{\alpha\beta} \dot{a}_{\alpha\beta} = 4\eta \mathbf{d} : \mathbf{d} = 4\eta \|\mathbf{d}\|^2 > 0$  due to (65) and (66).

Introducing the material tangents

$$\begin{aligned}
c^{\alpha\beta\gamma\delta} &:= 4 \frac{\partial^2 \Psi_0}{\partial a_{\alpha\beta} \partial a_{\gamma\delta}} = 2 \frac{\partial \tau^{\alpha\beta}}{\partial a_{\gamma\delta}}, \\
d^{\alpha\beta\gamma\delta} &:= 2 \frac{\partial^2 \Psi_0}{\partial a_{\alpha\beta} \partial b_{\gamma\delta}} = \frac{\partial \tau^{\alpha\beta}}{\partial b_{\gamma\delta}}, \\
e^{\alpha\beta\gamma\delta} &:= 2 \frac{\partial^2 \Psi_0}{\partial b_{\alpha\beta} \partial a_{\gamma\delta}} = 2 \frac{\partial M_0^{\alpha\beta}}{\partial a_{\gamma\delta}}, \\
f^{\alpha\beta\gamma\delta} &:= \frac{\partial^2 \Psi_0}{\partial b_{\alpha\beta} \partial b_{\gamma\delta}} = \frac{\partial M_0^{\alpha\beta}}{\partial b_{\gamma\delta}},
\end{aligned} \tag{132}$$

gives

$$\begin{aligned}
\Delta_x \delta_x \Psi_0 &= c^{\alpha\beta\gamma\delta} \frac{1}{2} \delta a_{\alpha\beta} \frac{1}{2} \Delta a_{\gamma\delta} + d^{\alpha\beta\gamma\delta} \frac{1}{2} \delta a_{\alpha\beta} \Delta b_{\gamma\delta} + \tau^{\alpha\beta} \frac{1}{2} \Delta \delta a_{\alpha\beta} \\
&+ e^{\alpha\beta\gamma\delta} \delta b_{\alpha\beta} \frac{1}{2} \Delta a_{\gamma\delta} + f^{\alpha\beta\gamma\delta} \delta b_{\alpha\beta} \Delta b_{\gamma\delta} + M_0^{\alpha\beta} \Delta \delta b_{\alpha\beta}.
\end{aligned} \tag{133}$$

Note that  $c^{\alpha\beta\gamma\delta}$  and  $f^{\alpha\beta\gamma\delta}$  possess both minor and major symmetries;  $d^{\alpha\beta\gamma\delta}$  and  $e^{\alpha\beta\gamma\delta}$  possess only minor symmetries, but additionally satisfy

$$d^{\alpha\beta\gamma\delta} = e^{\gamma\delta\alpha\beta}. \tag{134}$$

Due to the symmetries of  $c$ ,  $d$  and  $e$ , and due to Eqs. (79) and (81), one finds

$$\begin{aligned}
c^{\alpha\beta\gamma\delta} \frac{1}{2} \delta a_{\alpha\beta} \frac{1}{2} \Delta a_{\gamma\delta} &= \delta \mathbf{a}_\alpha \cdot \mathbf{a}_\beta c^{\alpha\beta\gamma\delta} \mathbf{a}_\gamma \cdot \Delta \mathbf{a}_\delta, \\
d^{\alpha\beta\gamma\delta} \frac{1}{2} \delta a_{\alpha\beta} \Delta b_{\gamma\delta} &= \delta \mathbf{a}_\alpha \cdot \mathbf{a}_\beta d^{\alpha\beta\gamma\delta} \mathbf{n} \cdot \Delta \tilde{\mathbf{a}}_{\alpha,\beta}, \\
e^{\alpha\beta\gamma\delta} \delta b_{\alpha\beta} \frac{1}{2} \Delta a_{\gamma\delta} &= \delta \tilde{\mathbf{a}}_{\alpha,\beta} \cdot \mathbf{n} e^{\alpha\beta\gamma\delta} \mathbf{a}_\gamma \cdot \Delta \mathbf{a}_\delta, \\
f^{\alpha\beta\gamma\delta} \delta b_{\alpha\beta} \Delta b_{\gamma\delta} &= \delta \tilde{\mathbf{a}}_{\alpha,\beta} \cdot \mathbf{n} f^{\alpha\beta\gamma\delta} \mathbf{n} \cdot \Delta \tilde{\mathbf{a}}_{\alpha,\beta},
\end{aligned} \tag{135}$$

where

$$\begin{aligned}
\delta \tilde{\mathbf{a}}_{\alpha,\beta} &:= \delta \mathbf{a}_{\alpha,\beta} - \Gamma_{\alpha\beta}^\epsilon \delta \mathbf{a}_\epsilon, \\
\Delta \tilde{\mathbf{a}}_{\alpha,\beta} &:= \Delta \mathbf{a}_{\alpha,\beta} - \Gamma_{\alpha\beta}^\epsilon \Delta \mathbf{a}_\epsilon.
\end{aligned} \tag{136}$$

Expressions for  $\Delta \delta a_{\alpha\beta}$  and  $\Delta \delta b_{\alpha\beta}$  are given in (83) and (86).

## 6.4 Material stability

For many material models, the four tangent matrices introduced in (132) can be written in the format

$$\hat{c}^{\alpha\beta\gamma\delta} = \hat{c}_{aa} a^{\alpha\beta} a^{\gamma\delta} + \hat{c}_a a^{\alpha\beta\gamma\delta} + \hat{c}_{ab} a^{\alpha\beta} b^{\gamma\delta} + \hat{c}_{ba} b^{\alpha\beta} a^{\gamma\delta} + \hat{c}_{bb} b^{\alpha\beta} b^{\gamma\delta}, \tag{137}$$

with suitable definitions of coefficients  $\hat{c}_{aa}$ ,  $\hat{c}_a$ ,  $\hat{c}_{ab}$ ,  $\hat{c}_{ba}$  and  $\hat{c}_{bb}$ . Sauer and Duong (2017) show that material stability requires

$$2\hat{c}_{aa} - \hat{c}_a > 0 \quad \& \quad \hat{c}_a < 0. \tag{138}$$

## 7 The Helfrich energy

In order to fully characterize the constitutive behavior, the Helmholtz free energy  $\Psi_0$  needs to be specified. The bending behavior of lipid bilayers is commonly described by the bending model of Helfrich (1973)

$$w = k(H - H_0)^2 + k_g \kappa. \tag{139}$$

Here  $k$  is the bending modulus,  $k_g$  is the Gaussian modulus and  $H_0$  denotes the so-called spontaneous curvature that can be used to model the presence of certain proteins embedded within the lipid bilayer.

This section presents the Helfrich energy for the cases of area-compressibility (Sec. 7.1) and area-incompressibility (Sec. 7.2), and discussed its properties (Sec. 7.3) and tangent matrices (Sec. 7.4). Sec. 7.5 discusses the relation between the models of Helfrich and Canham. The presentation follows [Sauer et al. \(2017\)](#) and [Sauer and Duong \(2017\)](#).

## 7.1 Area-compressible lipid bilayer

The Helfrich energy is an energy density per current surface area. Multiplying it by  $J$  and adding a quadratic energy term for the surface area change, gives the Helmholtz free energy

$$\Psi_0 = J w + \frac{K}{2}(J - 1)^2, \quad (140)$$

where  $K$  is the surface bulk modulus. A quadratic energy term is suitable for small area changes. For lipid bilayers, typically  $|J - 1| < 4\%$  before rupture occurs. According to (123), (124), (125) and (105), the stress and moment components then become

$$\begin{aligned} \sigma^{\alpha\beta} &= (K(J - 1) + k \Delta H^2 - k_g \kappa) a^{\alpha\beta} - 2k \Delta H b^{\alpha\beta} - \eta \dot{a}^{\alpha\beta}, \\ M^{\alpha\beta} &= (k \Delta H + 2k_g H) a^{\alpha\beta} - k_g b^{\alpha\beta}, \\ N^{\alpha\beta} &= (K(J - 1) + k \Delta H^2) a^{\alpha\beta} - k \Delta H b^{\alpha\beta} - \eta \dot{a}^{\alpha\beta}, \end{aligned} \quad (141)$$

where  $\Delta H := H - H_0$ .

## 7.2 Area-incompressible lipid bilayer

Since  $K$  is usually very large for lipid-bilayers, one may as well consider the surface to be fully area-incompressible. Using the Lagrange multiplier approach, one now has

$$\Psi_0 = J w + q g, \quad (142)$$

where the incompressibility constraint (76) is enforced by the Lagrange multiplier  $q$ .  $q$  is an independent variable that needs to be accounted for in the solution procedure (see Sec. 11). Physically,  $q$  corresponds to a surface tension. The stress and moment components now become

$$\begin{aligned} \sigma^{\alpha\beta} &= (q + k \Delta H^2 - k_g \kappa) a^{\alpha\beta} - 2k \Delta H b^{\alpha\beta} - \eta \dot{a}^{\alpha\beta}, \\ M^{\alpha\beta} &= (k \Delta H + 2k_g H) a^{\alpha\beta} - k_g b^{\alpha\beta}, \\ N^{\alpha\beta} &= (q + k \Delta H^2) a^{\alpha\beta} - k \Delta H b^{\alpha\beta} - \eta \dot{a}^{\alpha\beta}. \end{aligned} \quad (143)$$

They are identical to (141) for  $q = K g$ .

As  $K$  becomes larger and larger, both models approach the same solution. So from a physical point of view it may not make a big difference which model is used. Computationally, model (140) is easier to handle but can become inaccurate for large  $K$ , as is shown in [Sauer et al. \(2017\)](#). In analytical approaches, often (142) is preferred as it usually simplifies the solution. Examples for (142) are found in [Baesu et al. \(2004\)](#) and [Agrawal and Steigmann \(2009\)](#); (140) is considered in the original work of [Helfrich \(1973\)](#).

### 7.3 Model properties

In both preceding models, the membrane part only provides bulk stiffness, but lacks shear stiffness. For quasi-static computations the model can thus become unstable and should be stabilized, as is discussed in Sec. 12. Interestingly, the bending part of the Helfrich model can contribute an in-plane shear stiffness, which is shown in the following.

To this end, the surface tension

$$\gamma := \frac{1}{2} \boldsymbol{\sigma} : \mathbf{i} = \frac{1}{2} N_\alpha^\alpha, \quad (144)$$

is first introduced. For both (141) and (143) one finds

$$\gamma = q - k H_0 \Delta H, \quad (145)$$

where  $q = Kg$  in the former case. It can be seen that for  $H_0 \neq 0$ , the bending part contributes to the surface tension. This dependency has also been noted by Lipowsky (2013) and Rangamani et al. (2014). The surface tension is therefore not given by the membrane part alone. For the compressible case, the effective bulk modulus can then be determined from

$$K_{\text{eff}} := \frac{\partial \gamma}{\partial J}, \quad (146)$$

i.e. as the change of  $\gamma$  w.r.t.  $J$ . One finds

$$K_{\text{eff}} = K + k H_0 H/J, \quad (147)$$

since  $\partial H/\partial J = -H/J$ . Likewise, the effective shear modulus can be defined from

$$\mu_{\text{eff}} := J a_{\alpha\gamma} \frac{\partial N_{\text{dev}}^{\alpha\beta}}{2 \partial a_{\gamma\delta}} a_{\beta\delta}, \quad (148)$$

i.e. as the change of the deviatoric stress w.r.t. the deviatoric deformation (characterized by  $a_{\gamma\delta}/J$ ). The deviatoric in-plane stress is given by

$$N_{\text{dev}}^{\alpha\beta} := N^{\alpha\beta} - \gamma a^{\alpha\beta}. \quad (149)$$

One finds

$$N_{\text{dev}}^{\alpha\beta} = k \Delta H (H a^{\alpha\beta} - b^{\alpha\beta}) \quad (150)$$

for both (141) and (143). Evaluating (148) thus gives

$$\mu_{\text{eff}} = Jk (3H^2 - 2HH_0 - \kappa)/2. \quad (151)$$

The model therefore provides stabilizing shear stiffness if  $3H^2 > 2HH_0 + \kappa$ . Since this is not always the case (e.g. for flat surface regions), additional shear stabilization should be provided for quasi-static computations. This is discussed in Sec. 12. The value of  $\mu_{\text{eff}}$  is discussed further in the examples of Sec. 13. It is shown that  $\mu_{\text{eff}}$  can sufficiently stabilize the problem such that no additional shear stabilization is needed. It is also shown that  $\mu_{\text{eff}}$  does not necessarily need to be positive to avoid instabilities. Geometric stiffening, arising in large deformations, can also stabilize the surface.

### 7.4 Material tangent

In the following, the material tangents of Eq. (132) are evaluated and assessed. This is done by examining the contributions to (141) and (143) piecewise.

### 7.4.1 Area-compressibility

For the area-compressible case, the elastic membrane stress is characterized by

$$\tau^{\alpha\beta} = KJ(J-1)a^{\alpha\beta}. \quad (152)$$

From (132) thus follows

$$c^{\alpha\beta\gamma\delta} = KJ(2J-1)a^{\alpha\beta}a^{\gamma\delta} + 2KJ(J-1)a^{\alpha\beta\gamma\delta}. \quad (153)$$

Since  $c_a = 2KJ(J-1) \geq 1$  for  $J \geq 1$ , this model does not satisfy criteria (138) and therefore is unstable by itself.

### 7.4.2 Area-incompressibility

For the area-incompressible case, the elastic membrane stress is characterized by

$$\tau^{\alpha\beta} = -qJ a^{\alpha\beta}, \quad (154)$$

so that

$$c^{\alpha\beta\gamma\delta} = -qJ a^{\alpha\beta}a^{\gamma\delta} - 2qJ a^{\alpha\beta\gamma\delta}. \quad (155)$$

Since  $2c_{aa} - c_a = 0$ , this model does not satisfy criteria (138) and therefore is unstable by itself.

### 7.4.3 Bending part

The bending contribution, characterized by

$$\begin{aligned} \tau^{\alpha\beta} &= J(k\Delta H^2 - k_g\kappa)a^{\alpha\beta} - 2kJ\Delta H b^{\alpha\beta}, \\ M_0^{\alpha\beta} &= J(k\Delta H + 2k_g H)a^{\alpha\beta} - k_g J b^{\alpha\beta}, \end{aligned} \quad (156)$$

leads to

$$\begin{aligned} c^{\alpha\beta\gamma\delta} &= c_{aa}a^{\alpha\beta}a^{\gamma\delta} + c_a a^{\alpha\beta\gamma\delta} + c_{bb}b^{\alpha\beta}b^{\gamma\delta} + c_{ab}(a^{\alpha\beta}b^{\gamma\delta} + b^{\alpha\beta}a^{\gamma\delta}), \\ d^{\alpha\beta\gamma\delta} &= d_{aa}a^{\alpha\beta}a^{\gamma\delta} + d_a a^{\alpha\beta\gamma\delta} + d_{ab}a^{\alpha\beta}b^{\gamma\delta} + d_{ba}b^{\alpha\beta}a^{\gamma\delta} = e^{\gamma\delta\alpha\beta}, \\ f^{\alpha\beta\gamma\delta} &= f_{aa}a^{\alpha\beta}a^{\gamma\delta} + f_a a^{\alpha\beta\gamma\delta}, \end{aligned} \quad (157)$$

with

$$\begin{aligned} c_{aa} &= J(k\Delta H(\Delta H - 8H) + k_g\kappa), \\ c_a &= 2J(k\Delta H(\Delta H - 4H) - k_g\kappa), \\ c_{bb} &= 2kJ, \\ c_{ab} &= c_{ba} = 2kJ\Delta H, \\ d_{aa} &= J(k\Delta H - 2k_g H), \\ d_a &= 2Jk\Delta H, \\ d_{ab} &= Jk_g, \\ d_{ba} &= -Jk, \\ f_{aa} &= J(k/2 + k_g), \\ f_a &= Jk_g. \end{aligned} \quad (158)$$

The stability can be assessed by examining the bending tangent  $f^{\alpha\beta\gamma\delta}$ . According to (138), it is easy to see that stability requires

$$0 < -k_g < k. \quad (159)$$

## 7.5 The Canham model

A special case of the Helfrich model is the bending model of [Canham \(1970\)](#). It can be expressed as

$$\Psi_0 = J w, \quad w := \frac{c}{2} (\kappa_1^2 + \kappa_2^2). \quad (160)$$

Here,  $w$  can also be written as  $w = c b_\beta^\alpha b_\alpha^\beta / 2$  or  $w = c (2H^2 - \kappa)$ , so that the Canham model follows from the Helfrich model with  $k = 2c$ ,  $k_g = -c$  and  $H_0 = 0$ . Since this satisfies (159), the model is stable in bending. In particular, the Canham model gives

$$\sigma^{\alpha\beta} = c (2H^2 + \kappa) a^{\alpha\beta} - 4c H b^{\alpha\beta} - \eta \dot{a}^{\alpha\beta} \quad (161)$$

and

$$M^{\alpha\beta} = c b^{\alpha\beta}. \quad (162)$$

## 8 Weak form

This section presents the weak form of the thin shell equation (101), considering the area-compressible case (Sec. 8.1) and the area-incompressible case (Sec. 8.2). The decomposition into in-plane and out-of-plane contributions (Sec. 8.3) and the linearization (Sec. 8.4) follow. The presentation follows [Sauer and Duong \(2017\)](#) and [Sauer et al. \(2017\)](#).

### 8.1 Unconstrained system

The weak form of equilibrium equation (101) can be derived analogously to the mechanical power balance in Sec. 5.5 by simply replacing the velocity  $\mathbf{v}$  with the admissible variation  $\delta \mathbf{x} \in \mathcal{V}$ . Immediately one obtains

$$G_{\text{in}} + G_{\text{int}} - G_{\text{ext}} = 0 \quad \forall \delta \mathbf{x} \in \mathcal{V}, \quad (163)$$

with

$$\begin{aligned} G_{\text{in}} &= \int_{S_0} \delta \mathbf{x} \cdot \rho_0 \dot{\mathbf{v}} \, dA, \\ G_{\text{int}} &= \int_{S_0} \delta_x \Psi_0 \, dA = \int_{S_0} \frac{1}{2} \delta a_{\alpha\beta} \tau^{\alpha\beta} \, dA + \int_{S_0} \delta b_{\alpha\beta} M_0^{\alpha\beta} \, dA, \\ G_{\text{ext}} &= \int_S \delta \mathbf{x} \cdot \mathbf{f} \, da + \int_{\partial S} \delta \mathbf{x} \cdot \mathbf{T} \, ds + \int_{\partial S} \delta \mathbf{n} \cdot \mathbf{M} \, ds, \end{aligned} \quad (164)$$

according to Eqs. (110)–(113). As noted in (123), stress  $\tau^{\alpha\beta} = J \sigma^{\alpha\beta}$ , and hence also  $G_{\text{int}}$ , has elastic and viscous contributions. Due to Eq. (128), the elastic part of  $G_{\text{int}}$  can also be obtained as the variation of

$$\Pi_{\text{int}} = \int_{S_0} \Psi_0 \, dA \quad (165)$$

w.r.t.  $\mathbf{x}$ , i.e.  $G_{\text{int,el}} = \delta_x \Pi_{\text{int}}$ . Thus, if  $G_{\text{ext}}$  is also derivable from a potential, the quasi-static weak form  $G_{\text{int}} - G_{\text{ext}} = 0 \quad \forall \delta \mathbf{x} \in \mathcal{V}$  is the result of the principle of stationary potential energy.

## 8.2 Constrained system

For the constrained problem, the constraint  $g = 0$  needs to be included. The weak form of that is simply

$$G_g = \int_{S_0} \delta q g \, dA = 0 \quad \forall \delta q \in \mathcal{Q}, \quad (166)$$

where  $\delta q \in \mathcal{Q}$  is a suitably chosen variation of the Lagrange multiplier  $q$ . The weak form problem statement is then given by solving the two equations

$$\begin{aligned} G_{\text{in}} + G_{\text{int}} - G_{\text{ext}} &= 0 \quad \forall \delta \mathbf{x} \in \mathcal{V}, \\ G_g &= 0 \quad \forall \delta q \in \mathcal{Q}, \end{aligned} \quad (167)$$

for  $\mathbf{x}$  and  $q$ . Due to Eq. (126), one can find  $G_{\text{int,el}} + G_g = \delta \Pi_{\text{int}}$ , such that the static version of weak form (167), for suitable  $G_{\text{ext}}$ , is still the result of the principle of stationary potential energy.

## 8.3 Decomposition

As noted in Sauer et al. (2014), the weak form can be decomposed into in-plane and out-of-plane contributions. Denoting the in-plane and out-of-plane components of  $\delta \mathbf{x}$  by  $w_\alpha$  and  $w$ , such that  $\delta \mathbf{x} := w_\alpha \mathbf{a}^\alpha + w \mathbf{n}$ , one finds that

$$\delta a_{\alpha\beta} = w_{\alpha;\beta} + w_{\beta;\alpha} - 2w b_{\alpha\beta}. \quad (168)$$

Thus, the first part of  $G_{\text{int}}$  can be split into in-plane and out-of-plane contributions as

$$\int_S \frac{1}{2} \delta a_{\alpha\beta} \sigma^{\alpha\beta} \, da = G_\sigma^{\text{in}} + G_\sigma^{\text{out}}, \quad (169)$$

with

$$G_\sigma^{\text{in}} = \int_S w_{\alpha;\beta} \sigma^{\alpha\beta} \, da \quad (170)$$

and

$$G_\sigma^{\text{out}} = - \int_S w b_{\alpha\beta} \sigma^{\alpha\beta} \, da. \quad (171)$$

In principle – although not needed here – the second part of  $G_{\text{int}}$  can also be split into in-plane and out-of-plane contributions (Sauer and Duong, 2017).

## 8.4 Linearization

In the following, the linearization of the quasi-static case is discussed, where inertia and viscosity are absent. Inertia is linearly dependent on acceleration and thus easy to linearize. Viscosity can be conveniently treated within the framework of the implicit Euler time discretization scheme discussed in Sec. 10.4 and linearized in Sec. 10.5. The quasi-static case of weak form (167) can be written in the combined form

$$\delta \Pi_{\text{int}} - G_{\text{ext}} = 0 \quad \forall \delta \mathbf{x} \in \mathcal{V} \ \& \ \delta q \in \mathcal{Q}, \quad (172)$$

where  $\delta \Pi_{\text{int}} = G_{\text{int}} + G_g$ . Linearizing the internal virtual work gives, according to (129),

$$\Delta \delta \Pi_{\text{int}} = \int_{S_0} \Delta \mathbf{x} \delta \mathbf{x} \Psi_0 \, dA + \int_{S_0} \delta g \Delta q \, dA + \int_{S_0} \delta q \Delta g \, dA, \quad (173)$$

where  $\Delta_{\mathbf{x}}\delta_{\mathbf{x}}\Psi_0$  is given by (133). In order to linearize  $G_{\text{ext}}$ , dead loading for  $\mathbf{f}$ ,  $\mathbf{t}$  and  $\mathbf{M}$  is considered. The case of live pressure loading is given in Sauer et al. (2014). For dead loading, Sauer and Duong (2017) show that

$$\Delta G_{\text{ext}} = \int_{\partial S} m_{\tau} \delta \mathbf{a}_{\alpha} \cdot (\nu^{\beta} \mathbf{n} \otimes \mathbf{a}^{\alpha} + \nu^{\alpha} \mathbf{a}^{\beta} \otimes \mathbf{n}) \Delta \mathbf{a}_{\beta} \, ds, \quad (174)$$

which is symmetric w.r.t. variation and linearization.

## 9 Analytical solutions

This section presents two analytical solutions that describe simple bilayer deformations. They are useful for the verification of numerical results. Considered are pure bending and stretching of a flat sheet (Sec. 9.1), and the inflation of a sphere (Sec. 9.2).

### 9.1 Pure bending and stretching of a flat sheet

The first example considers the pure bending and stretching of a flat sheet. It is taken from Sauer and Duong (2017) and Sauer et al. (2017). The sheet has the dimension  $S \times L$  and is parameterized by the coordinates  $\xi^1 \in [0, S]$  and  $\xi^2 \in [0, L]$ . The sheet is deformed into a curved sheet with dimension  $s \times \ell$  by applying the homogeneous curvature  $\kappa_1$  and the homogeneous stretches  $\lambda_1 = s/S$  and  $\lambda_2 = \ell/L$  as is shown in Fig. 4. The deformed sheet thus forms a

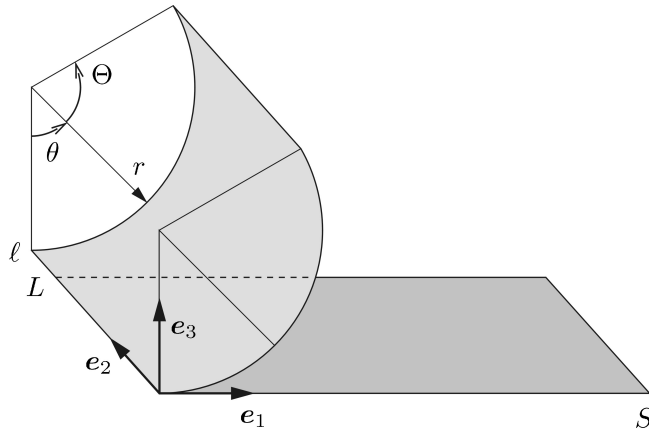


Figure 4: Pure bending and stretching of a sheet (Sauer and Duong, 2017): Deformation of a flat sheet into a curved sheet with constant radius.

circular arc with radius  $r = 1/\kappa_1$ . The parameters  $S$ ,  $L$ ,  $\kappa_1$ ,  $\lambda_1$  and  $\lambda_2$  are considered given, unless specified otherwise. According to the figure, the surface in its initial configuration can be described by

$$\mathbf{X}(\xi^1, \xi^2) = \xi^1 \mathbf{e}_1 + \xi^2 \mathbf{e}_2, \quad (175)$$

while its current surface can be described by

$$\mathbf{x}(\xi^1, \xi^2) = r \sin \theta \mathbf{e}_1 + \lambda_2 \xi^2 \mathbf{e}_2 + r (1 - \cos \theta) \mathbf{e}_3, \quad (176)$$

with  $\theta := \kappa_1 \lambda_1 \xi^1$  and  $r := 1/\kappa_1$ . The rotation at the end thus is  $\Theta = \kappa_1 \lambda_1 S$ . From these relations follow the initial tangent vectors

$$\begin{aligned} \mathbf{A}_1 &= \frac{\partial \mathbf{X}}{\partial \xi^1} = \mathbf{e}_1, \\ \mathbf{A}_2 &= \frac{\partial \mathbf{X}}{\partial \xi^2} = \mathbf{e}_2, \end{aligned} \tag{177}$$

the current tangent vectors

$$\begin{aligned} \mathbf{a}_1 &= \frac{\partial \mathbf{x}}{\partial \xi^1} = \lambda_1 (\cos \theta \mathbf{e}_1 + \sin \theta \mathbf{e}_3), \\ \mathbf{a}_2 &= \frac{\partial \mathbf{x}}{\partial \xi^2} = \lambda_2 \mathbf{e}_2, \end{aligned} \tag{178}$$

and the current surface normal

$$\mathbf{n} = -\sin \theta \mathbf{e}_1 + \cos \theta \mathbf{e}_3. \tag{179}$$

This results in the kinematic quantities

$$[A_{\alpha\beta}] = \begin{bmatrix} 1 & 0 \\ 0 & 1 \end{bmatrix}, \quad [A^{\alpha\beta}] = \begin{bmatrix} 1 & 0 \\ 0 & 1 \end{bmatrix}, \tag{180}$$

$$[a_{\alpha\beta}] = \begin{bmatrix} \lambda_1^2 & 0 \\ 0 & \lambda_2^2 \end{bmatrix}, \quad [a^{\alpha\beta}] = \begin{bmatrix} \lambda_1^{-2} & 0 \\ 0 & \lambda_2^{-2} \end{bmatrix}, \quad J = \lambda_1 \lambda_2, \tag{181}$$

and

$$\begin{aligned} [b_{\alpha\beta}] &= \begin{bmatrix} \kappa_1 \lambda_1^2 & 0 \\ 0 & 0 \end{bmatrix}, \quad [b_{\beta}^{\alpha}] = \begin{bmatrix} \kappa_1 & 0 \\ 0 & 0 \end{bmatrix}, \\ [b^{\alpha\beta}] &= \begin{bmatrix} \kappa_1 \lambda_1^{-2} & 0 \\ 0 & 0 \end{bmatrix}, \quad H = \frac{\kappa_1}{2}, \quad \kappa = 0. \end{aligned} \tag{182}$$

With this, the in-plane stress components become

$$\begin{aligned} N_1^1 &= q - k H^2, \\ N_2^2 &= q + k H^2, \end{aligned} \tag{183}$$

both for the area-incompressible model of (143) and the area-compressible model of (141) with  $q = K(J - 1)$ .

Now consider a cut at  $\theta$  that is perpendicular to the normal

$$\boldsymbol{\nu} = \mathbf{a}_1 / \lambda_1, \tag{184}$$

such that

$$\nu_1 = \mathbf{a}_1 \cdot \boldsymbol{\nu} = \lambda_1 \quad \text{and} \quad \nu_2 = \mathbf{a}_2 \cdot \boldsymbol{\nu} = 0. \tag{185}$$

The distributed bending moment acting on the cut is given by  $M = M^{\alpha\beta} \nu_\alpha \nu_\beta$ . Both models, (141) and (143), lead to the simple linear relation

$$M = k H, \tag{186}$$

between the prescribed curvature and the resulting bending moment. At  $\theta = 0$  and  $\theta = \Theta$ ,  $M$  corresponds to the boundary moment (per current length of the support). Measured per reference length, the boundary moment is  $M_0 = \lambda_2 M$ .

If the boundaries at  $\xi^1 = 0$  and  $\xi^1 = S$  are considered stress-free,  $N_1^1 = 0$ , so that

$$q = k H^2, \quad (187)$$

and consequently the support reaction (per current length) along  $\xi^2 = 0$  and  $\xi^2 = L$  is  $N := N_2^2 = 2k H^2$ . Per reference length this becomes  $N_0 = \lambda_1 N$ .

For the area-incompressible model of (142), one has  $\lambda_1 = 1/\lambda_2$ , such that the sheet is in a state of pure shear. For the area-compressible case according to model (140), one can determine  $\lambda_1$  from (187) with  $J = \lambda_1 \lambda_2$ , giving

$$\lambda_1 = \frac{1}{\lambda_2} \left[ \frac{k}{K} H^2 + 1 \right]. \quad (188)$$

## 9.2 Inflation of a sphere

The second example considers the inflation of a spherical vesicle. It is taken from [Sauer et al. \(2017\)](#). Since the surface area increases during inflation, the area-incompressible model (140) has to be considered. For this model, the in-plane traction component, given in (141), is

$$N^{\alpha\beta} = N_a a^{\alpha\beta} + N_b b^{\alpha\beta}, \quad (189)$$

with

$$\begin{aligned} N_a &:= k \Delta H^2 + K (J - 1), \\ N_b &:= -k \Delta H. \end{aligned} \quad (190)$$

The initial radius of the sphere is denoted by  $R$ , the initial volume is denoted by  $V_0 = 4\pi R^3/3$ . The vesicle remains spherical during inflation. The current radius during inflation is denoted by  $r$ , the current volume by  $V = 4\pi r^3/3$ . Considering the surface parameterization

$$\mathbf{x}(\phi, \theta) = \begin{bmatrix} r \cos \phi \sin \theta \\ r \sin \phi \sin \theta \\ -r \cos \theta \end{bmatrix}, \quad (191)$$

one finds

$$[a^{\alpha\beta}] = \frac{1}{r^2} \begin{bmatrix} 1/\sin^2 \theta & 0 \\ 0 & 1 \end{bmatrix}, \quad (192)$$

$b^{\alpha\beta} = -a^{\alpha\beta}/r$  and  $H = -1/r$ . The traction vector  $\mathbf{T} = \nu_\alpha \mathbf{T}^\alpha$  on a cut  $\perp \boldsymbol{\nu}$  thus becomes

$$\mathbf{T} = (N_a - N_b/r) \boldsymbol{\nu} + S^\alpha \nu_\alpha \mathbf{n} \quad (193)$$

according to (89). The in-plane component  $T_\nu := N_a - N_b/r$  must equilibrate the current pressure according to the well-known relation

$$p = \frac{2T_\nu}{r}. \quad (194)$$

One can thus establish the analytical pressure-volume relation

$$\bar{p}(\bar{V}) = 2\bar{H}_0 \bar{V}^{-\frac{2}{3}} - 2\bar{H}_0^2 \bar{V}^{-\frac{1}{3}} + 2\bar{K} \left( \bar{V}^{\frac{1}{3}} - \bar{V}^{-\frac{1}{3}} \right), \quad (195)$$

normalized according to the definitions  $\bar{p} := pR^3/k$ ,  $\bar{V} := V/V_0$ ,  $\bar{H}_0 := H_0 R$  and  $\bar{K} := KR^2/k$ .

## Part III: Computational formulation

Part III discusses the computational formulation based on the theory described in Part II. The finite element equations are presented for the shell PDE (Sec. 10) and the incompressibility constraint (Sec. 11). Stabilization is addressed (Sec. 12) and several numerical examples are presented (Sec. 13). Part III follows the developments in [Duong et al. \(2017\)](#) and [Sauer et al. \(2017\)](#).

### 10 Rotation-free shell FE

The shell theory presented in Part II results in a fourth order, nonlinear partial differential equation (PDE), which involves displacement degrees of freedom, but no rotations. In order to solve its weak form, a  $C^1$ -continuous finite element discretization is required.<sup>7</sup> Such a discretization is provided by isogeometric finite elements. In [Duong et al. \(2017\)](#) a new isogeometric FE formulation is presented for thin shells. The formulation is suitable for a wide range of materials, and it accounts for large deformations and rotations as Fig. 5 demonstrates. This section presents the formulation (Sec. 10.1-10.3) and discussed how to treat surface vis-

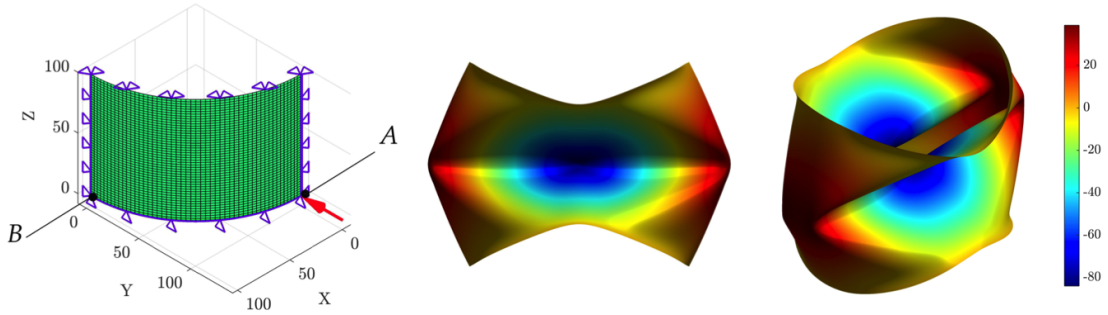


Figure 5: Pinching of a cylindrical shell ([Duong et al., 2017](#)).

cosity (Sec. 10.4),  $C^1$ -continuity (Sec. 10.6) and patch boundaries (Sec. 10.7). Linearization is addressed in Sec. 10.5.

#### 10.1 FE approximation

The surface geometry of the reference and current configuration (see Fig. 2) is discretized into  $n_{el}$  finite elements  $\Omega_e$ ,  $e = 1, \dots, n_{el}$ . Within each element, the surface is approximated by the finite element interpolations

$$\mathbf{X}^h = \mathbf{N} \mathbf{X}_e \quad (196)$$

and

$$\mathbf{x}^h = \mathbf{N} \mathbf{x}_e, \quad (197)$$

where  $\mathbf{N} := [N_1 \mathbf{1}, \dots, N_{n_e} \mathbf{1}]$  is a  $(3 \times 3n_e)$  array containing the  $n_e$  nodal shape functions  $N_I = N_I(\xi^1, \xi^2)$  of element  $\Omega^e$  defined in parameter space  $\mathcal{P}$ .  $\mathbf{X}_e := [\mathbf{X}_1^T, \dots, \mathbf{X}_{n_e}^T]^T$  and  $\mathbf{x}_e := [\mathbf{x}_1^T, \dots, \mathbf{x}_{n_e}^T]^T$  contain the  $n_e$  nodal position vectors of  $\Omega^e$ . The tangent vectors of the

<sup>7</sup>Strictly,  $G^1$ -continuity (i.e. continuity in  $\mathbf{n}$  but not necessary in  $\mathbf{a}_\alpha$ ) is sufficient.

surface are thus approximated by

$$\mathbf{A}_\alpha^h = \frac{\partial \mathbf{X}^h}{\partial \xi^\alpha} = \mathbf{N}_{,\alpha} \mathbf{X}_e \quad (198)$$

and

$$\mathbf{a}_\alpha^h = \frac{\partial \mathbf{x}^h}{\partial \xi^\alpha} = \mathbf{N}_{,\alpha} \mathbf{x}_e. \quad (199)$$

Likewise, the the tangent derivative  $\mathbf{a}_{\alpha,\beta}$  and the variations  $\delta \mathbf{x}$  and  $\delta \mathbf{a}_\alpha$  are approximated by

$$\mathbf{a}_{\alpha,\beta}^h = \mathbf{N}_{,\alpha\beta} \mathbf{x}_e, \quad (200)$$

$$\delta \mathbf{x}^h = \mathbf{N} \delta \mathbf{x}_e \quad (201)$$

and

$$\delta \mathbf{a}_\alpha^h = \mathbf{N}_{,\alpha} \delta \mathbf{x}_e. \quad (202)$$

According to (6), the surface normals  $\mathbf{N}$  and  $\mathbf{n}$  are thus approximated by

$$\mathbf{N}^h = \frac{\mathbf{A}_1^h \times \mathbf{A}_2^h}{\|\mathbf{A}_1^h \times \mathbf{A}_2^h\|} \quad (203)$$

and

$$\mathbf{n}^h = \frac{\mathbf{a}_1^h \times \mathbf{a}_2^h}{\|\mathbf{a}_1^h \times \mathbf{a}_2^h\|}. \quad (204)$$

With these approximations, all the kinematical quantities of Sec. 4, like  $a_{\alpha\beta}$ ,  $a^{\alpha\beta}$ ,  $\mathbf{a}^\alpha$  and  $b_{\alpha\beta}$ , can be approximated.

## 10.2 Discretization of kinematical variations

Based on the above expressions, all the variations appearing within weak form (163) can be evaluated. According to (79) and (81), the discretization of  $\delta a_{\alpha\beta}$  and  $\delta b_{\alpha\beta}$  follow as

$$\begin{aligned} \delta a_{\alpha\beta}^h &= \delta \mathbf{x}_e^T \left[ \mathbf{N}_{,\alpha}^T \mathbf{N}_{,\beta} + \mathbf{N}_{,\beta}^T \mathbf{N}_{,\alpha} \right] \mathbf{x}_e, \\ \delta b_{\alpha\beta}^h &= \delta \mathbf{x}_e^T \mathbf{N}_{;\alpha\beta}^T \mathbf{n}^h, \end{aligned} \quad (205)$$

where

$$\mathbf{N}_{;\alpha\beta} := \mathbf{N}_{,\alpha\beta} - \Gamma_{\alpha\beta}^\gamma \mathbf{N}_{,\gamma} \quad (206)$$

has been introduced. In the same fashion, the increments  $\Delta a_{\alpha\beta}$  and  $\Delta b_{\alpha\beta}$  are discretized by

$$\begin{aligned} \Delta a_{\alpha\beta}^h &= \Delta \mathbf{x}_e^T \left[ \mathbf{N}_{,\alpha}^T \mathbf{N}_{,\beta} + \mathbf{N}_{,\beta}^T \mathbf{N}_{,\alpha} \right] \mathbf{x}_e, \\ \Delta b_{\alpha\beta}^h &= \Delta \mathbf{x}_e^T \mathbf{N}_{;\alpha\beta}^T \mathbf{n}^h. \end{aligned} \quad (207)$$

For the increments of  $\delta a_{\alpha\beta}$  and  $\delta b_{\alpha\beta}$ , given in (83) and (86), the approximations

$$\begin{aligned} \Delta \delta a_{\alpha\beta}^h &= \delta \mathbf{x}_e^T \left[ \mathbf{N}_{,\alpha}^T \mathbf{N}_{,\beta} + \mathbf{N}_{,\beta}^T \mathbf{N}_{,\alpha} \right] \Delta \mathbf{x}_e \\ \Delta \delta b_{\alpha\beta}^h &= -\delta \mathbf{x}_e^T \left[ \mathbf{N}_{,\gamma}^T (\mathbf{n} \otimes \mathbf{a}^\gamma) \mathbf{N}_{;\alpha\beta} + \mathbf{N}_{;\alpha\beta}^T (\mathbf{a}^\gamma \otimes \mathbf{n}) \mathbf{N}_{,\gamma} + \mathbf{N}_{,\gamma}^T a^{\gamma\delta} b_{\alpha\beta} (\mathbf{n} \otimes \mathbf{n}) \mathbf{N}_{,\delta} \right] \Delta \mathbf{x}_e \end{aligned} \quad (208)$$

then follow. Here, superscript  $h$  has been omitted from  $\mathbf{n}$ ,  $\mathbf{a}^\gamma$ ,  $a^{\gamma\delta}$  and  $b_{\alpha\beta}$  for simplicity. For the rest of the paper, all quantities are understood to be discrete even without explicit use of superscript  $h$ .

### 10.3 Discretized weak form

In the discrete system the weak form of Sec. 8 takes the form

$$G = \sum_{e=1}^{n_{\text{el}}} G^e = \sum_{e=1}^{n_{\text{el}}} (G_{\text{in}}^e + G_{\text{int}}^e + G_{\text{c}}^e - G_{\text{ext}}^e), \quad (209)$$

where  $G_{\bullet}^e$  are the elemental contributions to the expressions in (164). Inserting the above interpolations into (209) leads to

$$G^e = \delta \mathbf{x}_e^{\text{T}} \mathbf{f}^e, \quad (210)$$

with

$$\mathbf{f}^e := \mathbf{f}_{\text{in}}^e + \mathbf{f}_{\text{int}}^e + \mathbf{f}_{\text{c}}^e - \mathbf{f}_{\text{ext}}^e. \quad (211)$$

The first term,

$$\mathbf{f}_{\text{in}}^e := - \int_{\Omega^e} \rho \mathbf{N}^{\text{T}} \mathbf{N} \, da \, \dot{\mathbf{v}}_e, \quad (212)$$

defines the inertia forces acting on the nodes of element  $\Omega^e$ . The second term,  $\mathbf{f}_{\text{int}}^e := \mathbf{f}_{\sigma}^e + \mathbf{f}_M^e$ , defines the internal forces of element  $\Omega^e$  caused by the membrane stress  $\sigma^{\alpha\beta}$  and the bending moment  $M^{\alpha\beta}$ . The two contributions are given by

$$\mathbf{f}_{\sigma}^e := \int_{\Omega^e} \sigma^{\alpha\beta} \mathbf{N}_{,\alpha}^{\text{T}} \mathbf{a}_{\beta} \, da, \quad (213)$$

and

$$\mathbf{f}_M^e := \int_{\Omega^e} M^{\alpha\beta} \mathbf{N}_{,\alpha\beta}^{\text{T}} \mathbf{n} \, da. \quad (214)$$

Following decomposition (169),  $\mathbf{f}_{\sigma}^e$  can be split into the in-plane and out-of-plane contributions (Sauer et al., 2014)

$$\begin{aligned} \mathbf{f}_{\sigma\text{in}}^e &:= \mathbf{f}_{\sigma}^e - \mathbf{f}_{\sigma\text{out}}^e, \\ \mathbf{f}_{\sigma\text{out}}^e &:= - \int_{\Omega^e} \sigma^{\alpha\beta} b_{\alpha\beta} \mathbf{N}^{\text{T}} \mathbf{n} \, da. \end{aligned} \quad (215)$$

The third term,

$$\mathbf{f}_{\text{c}}^e = \int_{\Omega^e} \mathbf{N}^{\text{T}} p_{\text{c}} \mathbf{n} \, da, \quad (216)$$

defines the FE contact forces due to the contact pressure  $p_{\text{c}}$ . The last term,  $\mathbf{f}_{\text{ext}}^e := \mathbf{f}_f^e + \mathbf{f}_t^e + \mathbf{f}_m^e$ , defines the FE forces due to the external loads  $\mathbf{f}$ ,  $\mathbf{t}$  and  $m_{\tau}$ . The three pieces are given by

$$\begin{aligned} \mathbf{f}_f^e &:= \int_{\Omega^e} \mathbf{N}^{\text{T}} \mathbf{f} \, da, \\ \mathbf{f}_t^e &:= \int_{\partial_t \Omega^e} \mathbf{N}^{\text{T}} \mathbf{t} \, ds, \\ \mathbf{f}_m^e &:= \int_{\partial_m \Omega^e} \mathbf{N}_{,\alpha}^{\text{T}} \nu^{\alpha} m_{\tau} \mathbf{n} \, ds. \end{aligned} \quad (217)$$

In the examples considered here, the external forces are zero.

The discretized system is in equilibrium if all nodal forces sum up to zero (see Sec. 11.2 for details). This force balance is a second order system of ordinary differential equations due to the inertia term. If inertia is neglected, as is considered in the remainder of this paper, the force balance is a first order system of ODEs due to the viscosity term. The temporal discretization of the viscosity term is discussed next.

## 10.4 Temporal discretization of the viscosity term

In order to solve the time-dependent problem, time is discretized into a set of  $n_t$  steps and the solution is advanced from step  $t_n$  to  $t_{n+1}$ . The viscosity dependant stress  $\sigma_{\text{visc}}^{\alpha\beta} = -\eta \dot{a}^{\alpha\beta}$  can be discretized at  $t_{n+1}$  by the first order rate approximation

$$\dot{a}_{n+1}^{\alpha\beta} \approx \frac{1}{\Delta t_{n+1}} (a_{n+1}^{\alpha\beta} - a_n^{\alpha\beta}), \quad (218)$$

where  $\bullet_n := \bullet(t_n)$  and  $\Delta t_{n+1} := t_{n+1} - t_n$ . At the new step  $t_{n+1}$ , the problem is then solved implicitly for the current nodal positions  $\mathbf{x}_I(t_{n+1})$ , given the previous positions  $\mathbf{x}_I(t_n)$ . The reference configuration is taken as the initial configuration at time  $t_0 = 0$ , i.e.  $\mathbf{X}_I = \mathbf{x}_I(t_0)$ . This temporal discretization approach corresponds to the implicit Euler scheme.

## 10.5 Linearization

The resulting non-linear equations at the current time step are solved with the Newton-Raphson method. This requires the linearization of the discretized weak form. The most important contribution is the linearization of the internal virtual work. The linearization of inertia and the external forces is not required for the later examples, and they are therefore omitted here. The interested reader can find them in [Duong et al. \(2017\)](#). The linearization of the contact forces can be found in the contact literature, e.g. see [Sauer and De Lorenzis \(2013\)](#) and [Sauer and De Lorenzis \(2015\)](#).

According to (173) and (133), the linearization of  $G_{\text{int}}^e$  (in the absence of the incompressibility constraint) leads to

$$\begin{aligned} \Delta G_{\text{int}}^e = \int_{\Omega_0^e} & \left( c^{\alpha\beta\gamma\delta} \frac{1}{2} \delta a_{\alpha\beta} \frac{1}{2} \Delta a_{\gamma\delta} \quad + d^{\alpha\beta\gamma\delta} \frac{1}{2} \delta a_{\alpha\beta} \Delta b_{\gamma\delta} \right. \\ & + e^{\alpha\beta\gamma\delta} \delta b_{\alpha\beta} \frac{1}{2} \Delta a_{\gamma\delta} \quad + f^{\alpha\beta\gamma\delta} \delta b_{\alpha\beta} \Delta b_{\gamma\delta}^h \\ & + J \sigma^{\alpha\beta} \frac{1}{2} \Delta \delta a_{\alpha\beta} \quad + J M^{\alpha\beta} \Delta \delta b_{\alpha\beta} \\ & \left. - \frac{J\eta}{4\Delta t} \delta a_{\alpha\beta} \left[ (a^{\alpha\beta} - a_n^{\alpha\beta}) a^{\gamma\delta} + 2a^{\alpha\beta\gamma\delta} \right] \Delta a_{\alpha\beta}^{\square} \right) dA, \end{aligned} \quad (219)$$

where subscript  $n + 1$  has been omitted. The tangent matrices  $c^{\alpha\beta\gamma\delta}$ ,  $d^{\alpha\beta\gamma\delta}$ ,  $e^{\alpha\beta\gamma\delta}$  and  $f^{\alpha\beta\gamma\delta}$  have been given in Sec. 7.4. The last term arises from the viscosity approximation of (218). It can be absorbed into  $c^{\alpha\beta\gamma\delta}$  if one replaces

$$c^{\alpha\beta\gamma\delta} \leftarrow c^{\alpha\beta\gamma\delta} - \frac{J\eta}{\Delta t} \left[ (a^{\alpha\beta} - a_n^{\alpha\beta}) a^{\gamma\delta} + 2a^{\alpha\beta\gamma\delta} \right]. \quad (220)$$

Using (135), and exploiting the minor symmetries in the tangent matrices, one finds

$$\begin{aligned} c^{\alpha\beta\gamma\delta} \frac{1}{2} \delta a_{\alpha\beta} \frac{1}{2} \Delta a_{\gamma\delta} &= c^{\alpha\beta\gamma\delta} \delta \mathbf{x}_e^T \mathbf{N}_{;\alpha}^T (\mathbf{a}_\beta \otimes \mathbf{a}_\gamma) \mathbf{N}_{;\delta} \Delta \mathbf{x}_e, \\ d^{\alpha\beta\gamma\delta} \frac{1}{2} \delta a_{\alpha\beta} \Delta b_{\gamma\delta} &= d^{\alpha\beta\gamma\delta} \delta \mathbf{x}_e^T \mathbf{N}_{;\alpha}^T (\mathbf{a}_\beta \otimes \mathbf{n}) \mathbf{N}_{;\gamma\delta} \Delta \mathbf{x}_e, \\ e^{\alpha\beta\gamma\delta} \delta b_{\alpha\beta} \frac{1}{2} \Delta a_{\gamma\delta} &= e^{\alpha\beta\gamma\delta} \delta \mathbf{x}_e^T \mathbf{N}_{;\alpha\beta}^T (\mathbf{n} \otimes \mathbf{a}_\gamma) \mathbf{N}_{;\delta} \Delta \mathbf{x}_e, \\ f^{\alpha\beta\gamma\delta} \delta b_{\alpha\beta} \Delta b_{\gamma\delta} &= f^{\alpha\beta\gamma\delta} \delta \mathbf{x}_e^T \mathbf{N}_{;\alpha\beta}^T (\mathbf{n} \otimes \mathbf{n}) \mathbf{N}_{;\gamma\delta} \Delta \mathbf{x}_e, \end{aligned} \quad (221)$$

such that

$$\Delta G_{\text{int}}^e = \delta \mathbf{x}_e^T \left[ \mathbf{k}_{\sigma\sigma}^e + \mathbf{k}_{\sigma M}^e + \mathbf{k}_{M\sigma}^e + \mathbf{k}_{MM}^e + \mathbf{k}_\sigma^e + \mathbf{k}_M^e \right] \Delta \mathbf{x}_e, \quad (222)$$

with

$$\begin{aligned}
\mathbf{k}_{\sigma\sigma}^e &:= \int_{\Omega_0^e} c^{\alpha\beta\gamma\delta} \mathbf{N}_{,\alpha}^T (\mathbf{a}_\beta \otimes \mathbf{a}_\gamma) \mathbf{N}_{,\delta} dA, \\
\mathbf{k}_{\sigma M}^e &:= \int_{\Omega_0^e} d^{\alpha\beta\gamma\delta} \mathbf{N}_{,\alpha}^T (\mathbf{a}_\beta \otimes \mathbf{n}) \mathbf{N}_{,\gamma\delta} dA, \\
\mathbf{k}_{M\sigma}^e &:= \int_{\Omega_0^e} e^{\alpha\beta\gamma\delta} \mathbf{N}_{;\alpha\beta}^T (\mathbf{n} \otimes \mathbf{a}_\gamma) \mathbf{N}_{,\delta} dA, \\
\mathbf{k}_{MM}^e &:= \int_{\Omega_0^e} f^{\alpha\beta\gamma\delta} \mathbf{N}_{;\alpha\beta}^T (\mathbf{n} \otimes \mathbf{n}) \mathbf{N}_{;\gamma\delta} dA,
\end{aligned} \tag{223}$$

and

$$\begin{aligned}
\mathbf{k}_\sigma^e &= \int_{\Omega^e} \mathbf{N}_{,\alpha}^T \sigma^{\alpha\beta} \mathbf{N}_{,\beta} da, \\
\mathbf{k}_M^e &= \mathbf{k}_{M1}^e + \mathbf{k}_{M2}^e + (\mathbf{k}_{M2}^e)^T,
\end{aligned} \tag{224}$$

and

$$\begin{aligned}
\mathbf{k}_{M1}^e &:= - \int_{\Omega^e} b_{\alpha\beta} M^{\alpha\beta} a^{\gamma\delta} \mathbf{N}_{,\gamma}^T (\mathbf{n} \otimes \mathbf{n}) \mathbf{N}_{,\delta} da, \\
\mathbf{k}_{M2}^e &:= - \int_{\Omega^e} M^{\alpha\beta} \mathbf{N}_{,\gamma}^T (\mathbf{n} \otimes \mathbf{a}^\gamma) \mathbf{N}_{;\alpha\beta} da.
\end{aligned} \tag{225}$$

The first four  $\mathbf{k}^e$  are the material tangent matrices of element  $\Omega^e$ . In order for those to be positive definite, stability criterion (138) needs to be satisfied.  $\mathbf{k}_\sigma^e$  and  $\mathbf{k}_M^e$  are the geometric tangent matrices of element  $\Omega^e$ .

## 10.6 C1-continuous shape functions

As noted before, the FE shape function have to be at least  $C^1$ -continuous everywhere in the domain, including element boundaries. This property is provided by the shape functions used in isogeometric analysis (Hughes et al., 2005; Cottrell et al., 2009). An example are NURBS (Non-uniform rational B-splines). Thanks to the Bézier extraction operator  $\mathbf{C}^e$  introduced by Borden et al. (2011), the usual finite element structure can be used for NURBS basis functions. The NURBS shape function of node (= control point)  $A$  is given by

$$N_A(\xi^\alpha) = \frac{w_A \hat{N}_A^e(\xi^\alpha)}{\sum_{A=1}^{n_e} w_A \hat{N}_A^e(\xi^\alpha)}. \tag{226}$$

Here,  $n_e$  is the number of control points defining element  $\Omega^e$ ,  $w_A$  is a weight, and  $\hat{N}_A^e$  is the B-spline basis function expressed in terms of Bernstein polynomials according to

$$\hat{\mathbf{N}}^e(\xi^\alpha) = \mathbf{C}_1^e \mathbf{B}(\xi^1) \otimes \mathbf{C}_2^e \mathbf{B}(\xi^2), \tag{227}$$

with  $\hat{N}_A^e$  being the corresponding entries of matrix  $\hat{\mathbf{N}}^e$ . Further details can be found in Borden et al. (2011). Fig. 6 shows the basis function  $\hat{N}_A^e$  for a one-dimensional example with five control points. The tensor-based structure of (227) provides a simple extension to two dimensions, as long as the surface  $\mathcal{S}$  can be globally defined from a rectangular parameter domain. If this is not the case, alternatives exists. One possibility is to use T-spline basis functions (Scott et al., 2011). Another option is to construct the surface from multiple NURBS patches (e.g. see the example in Fig. 16). In this case, the relative rotation between neighboring patches has to be suppressed. This is discussed in the following section. It is also possible to apply local refinement to the patches (Johannessen et al., 2014; Zimmermann and Sauer, 2017).

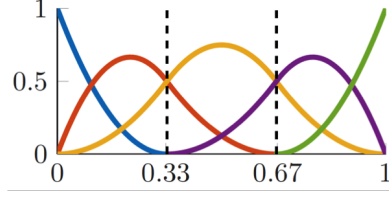


Figure 6: The B-spline basis functions for a patch of three elements and five control points (Corbett, 2016).

## 10.7 Patch interfaces

To constrain rotations between patches, the constraint potential

$$\Pi_n = \int_{\mathcal{L}_0} \frac{\epsilon}{2} (\mathbf{n} - \tilde{\mathbf{n}}) \cdot (\mathbf{n} - \tilde{\mathbf{n}}) dS \quad (228)$$

is added to the formulation.  $\mathcal{L}_0$  denotes the patch interface in the reference configuration,  $\epsilon$  is a penalty parameter, and  $\mathbf{n}$  and  $\tilde{\mathbf{n}}$  are the normal vectors on the two sides of the patch interface. The variation, linearization and FE discretization of (228) is discussed in Duong et al. (2017). Careful implementation of the approach leads to no loss in accuracy compared to single patches as Fig. 7 shows.

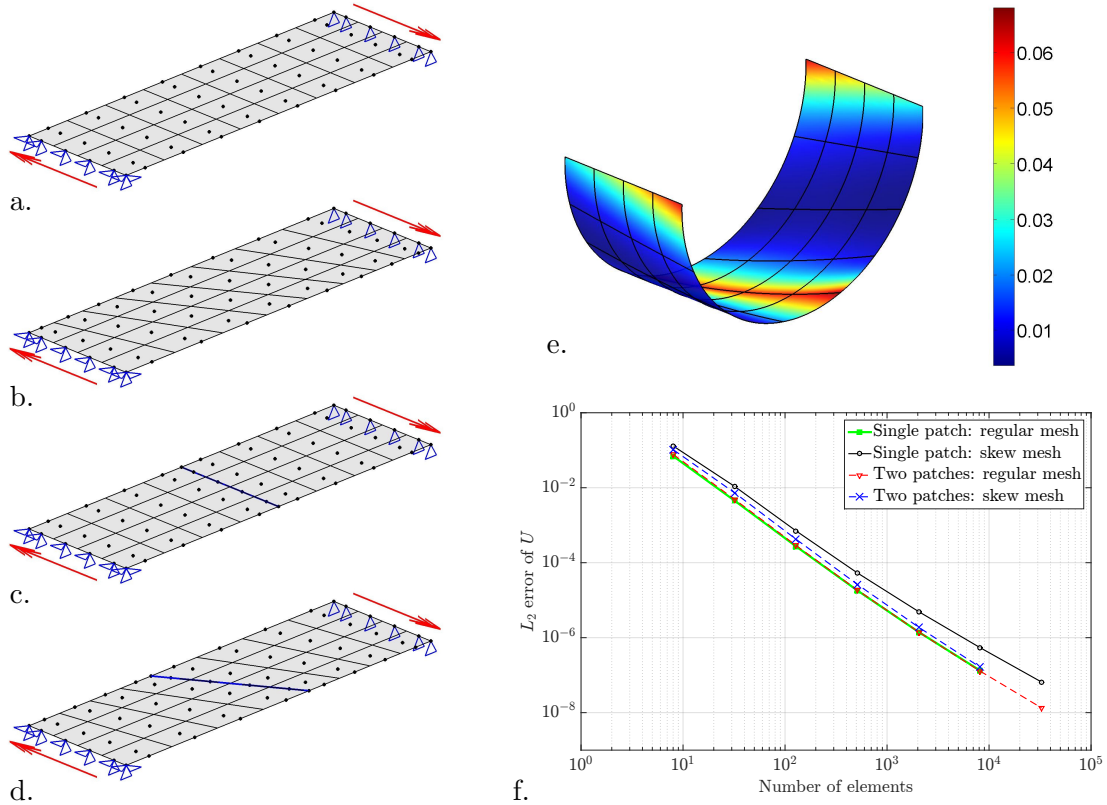


Figure 7: Pure bending of a flat sheet (cf. Sec. 9) considering: a. single patch with regular mesh, b. single patch with skew mesh, c. two patches with regular mesh, and d. two patches with skew mesh. e. Deformed configuration coloured by the relative error in mean curvature  $H$ . f.  $L_2$  error of the solution w.r.t. mesh refinement (Duong et al., 2017).

## 11 Mixed finite elements

For the area-incompressible case of Eq. (142), the Lagrange multiplier  $q$  and the corresponding weak form equation have to be discretized as well. This is discussed in the following (Sec. 11.1) using LBB-conforming finite elements (Sec. 11.3). The resulting solution procedure is presented in Sec. 11.2 using the normalization scheme of Sec. 11.4

### 11.1 Discretization of the area constraint

The Lagrange multiplier is approximated by the interpolation

$$q^h = \mathbf{L} \mathbf{q}_e, \quad (229)$$

analogously to the deformation in Eq. (197). Here  $\mathbf{L} := [L_1, \dots, L_{m_e}]$  is a  $(1 \times m_e)$  array containing the  $m_e$  nodal shape functions  $L_I = L_I(\xi^\alpha)$  of surface element  $\Omega^e$ , and  $\mathbf{q}_e := [q_1, \dots, q_{m_e}]^T$  contains the  $m_e$  nodal Lagrange multipliers of the element. It follows that

$$\delta q^h = \mathbf{L} \delta \mathbf{q}_e, \quad (230)$$

such that weak form (166) becomes

$$G_g = \sum_{e=1}^{n_{el}} G_g^e, \quad (231)$$

where

$$G_g^e = \delta \mathbf{q}_e^T \mathbf{g}^e, \quad (232)$$

with

$$\mathbf{g}^e := \int_{\Omega_0^e} \mathbf{L}^T g \, dA. \quad (233)$$

### 11.2 Solution procedure

The mixed problem is characterized by the two unknown fields  $\mathbf{x}$  and  $q$ , or their discrete counterparts  $\mathbf{x}$  and  $\mathbf{q}$ . The combined weak form of the discrete problem is given by

$$\delta \mathbf{x}^T \mathbf{f}(\mathbf{x}, \mathbf{q}) + \delta \mathbf{q}^T \mathbf{g}(\mathbf{x}) = 0, \quad \forall \delta \mathbf{x} \in \mathcal{V}^h \ \& \ \delta \mathbf{q} \in \mathcal{Q}^h, \quad (234)$$

which follows from adding the elemental contributions of  $G^e$  and  $G_g^e$  given in (210) and (232). Here  $\mathbf{x}$ ,  $\mathbf{q}$ ,  $\delta \mathbf{x}$  and  $\delta \mathbf{q}$  are global vectors containing all nodal deformations, Lagrange multipliers and their variations.  $\mathcal{V}^h$  and  $\mathcal{Q}^h$  are the discrete counterparts to spaces  $\mathcal{V}$  and  $\mathcal{Q}$ . The global vectors  $\mathbf{f}$  and  $\mathbf{g}$  are assembled from the elemental contributions  $\mathbf{f}_{\text{int}}^e$ ,  $\mathbf{f}_c^e$ ,  $\mathbf{f}_{\text{ext}}^e$  and  $\mathbf{g}^e$  by adding corresponding entries. Eq. (234) is satisfied if  $\mathbf{f} = \mathbf{0}$  and  $\mathbf{g} = \mathbf{0}$  at nodes where no Dirichlet BC apply. These two nonlinear equations are then solved with Newton's method for the unknowns  $\mathbf{x}$  and  $\mathbf{q}$ .

If no constraint is present (like in model (140)), the parts containing  $\mathbf{q}$  and  $\mathbf{g}$  are simply skipped.

### 11.3 LBB condition

For mixed FE problems, the discretization of  $\boldsymbol{x}$  and  $q$  cannot be chosen independently. Instead,  $\boldsymbol{x}^h$  and  $q^h$  should satisfy the LBB-condition<sup>8</sup>

$$\inf_{q^h \in \mathcal{Q}^h} \sup_{\boldsymbol{v}^h \in \mathcal{V}^h} \frac{\int_{\mathcal{S}} q^h \operatorname{div}_s \boldsymbol{v}^h \, dA}{\|\boldsymbol{v}^h\|_{H^1} \|q^h\|_{L^2}} = \gamma^h \geq \gamma > 0 \quad (235)$$

(Babuška, 1973; Bathe, 1996). For the presented shell discretization, the inf-sup value  $\gamma^h$  corresponds to the smallest eigenvalue of

$$\mathbf{G} \boldsymbol{\phi} = \lambda \mathbf{S} \boldsymbol{\phi}, \quad (236)$$

(Bathe, 2001), where

$$\begin{aligned} \mathbf{G} &:= \mathbf{k}_g^T \mathbf{T}^{-1} \mathbf{k}_g, \\ \mathbf{k}_g &:= \int_{\mathcal{S}^h} \mathbf{L}^T \mathbf{a}^\alpha \cdot \mathbf{N}_{,\alpha} \, da, \\ \mathbf{T} &:= \int_{\mathcal{S}^h} \mathbf{L}^T \mathbf{L} \, da, \\ \mathbf{S} &:= \int_{\mathcal{S}^h} \left( \mathbf{N}^T \mathbf{N} + a^{\alpha\beta} \mathbf{N}_{,\alpha}^T \mathbf{N}_{,\beta} \right) da, \end{aligned} \quad (237)$$

and  $(\lambda, \boldsymbol{\phi})$  denotes the eigenvalue/eigenvector pair. Eigenvalue problem (236) is defined on the entire system, and hence the integrals are taken over the entire surface  $\mathcal{S}^h$  and the arrays  $\mathbf{N}$  and  $\mathbf{L}$  now extended to all nodes. The LBB-condition can be satisfied if  $\boldsymbol{x}$  is interpolated by  $C^1$ -continuous, bi-quadratic NURBS and  $q$  is interpolated by  $C^0$ -continuous, bi-linear Lagrange shape functions (Loc et al., 2013). This is demonstrated in Fig. 8. If the LBB-condition is

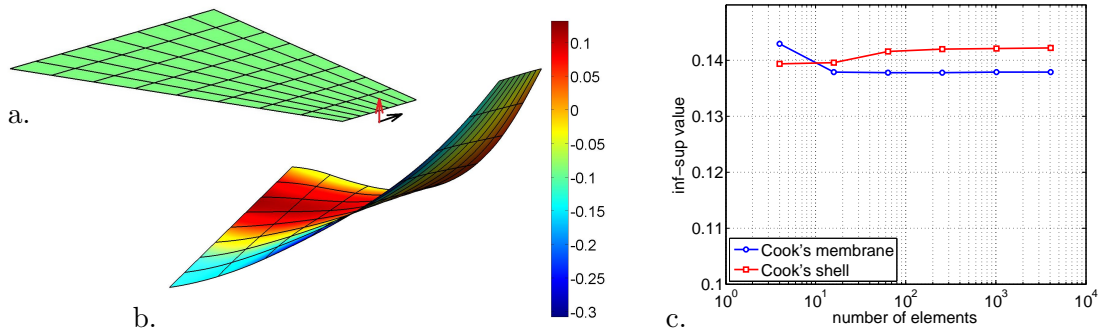


Figure 8: Cook’s membrane test for mixed displacement/pressure FE (here for NURBS-based bi-quadratic displacement and Lagrange-based bi-linear pressure interpolation): initial configuration (a.), deformed configuration (b.), inf-sup value (c.). The left boundary is fully clamped, while on the right boundary a distributed force is applied considering two cases: only an in-plane force (‘Cook’s membrane’) and a force with an out-of-plane component (‘Cook’s shell’). Area-incompressibility together with shear model ‘A-st’ with  $\bar{\mu} = 5$  is considered. The color in the middle figure shows the Lagrange multiplier. Since the inf-sup value is bounded the formulation is LBB-stable.

violated, oscillations in the Lagrange multiplier appear. Such oscillations do not appear in this example. Also the multi-patch example in Sec. 13.2 does not exhibit such oscillations if it is

<sup>8</sup>Named after Ladyzhenskaya, Babuška & Brezzi

discretized by the mixed approach described above. However, If a penalty regularization of constraint (76) is used, oscillations appear as the penalty parameter (i.e. the bulk modulus  $K$ ) is increased (Sauer et al., 2017).

## 11.4 Normalization

For a numerical implementation, the preceding expressions need to be normalized. For this purpose a length scale  $L_0$ , time scale  $T_0$  and force  $F_0$  are chosen, and used to normalize all lengths, times and forces in the system. Velocities, surface densities, surface pressures, membrane stiffness and membrane viscosity are then normalized by the scales

$$v_0 := \frac{L_0}{T_0}, \quad \rho_0 := \frac{F_0 T_0^2}{L_0^3}, \quad p_0 := \frac{F_0}{L_0^2}, \quad \mu_0 := \frac{F_0}{L_0}, \quad \eta_0 := \frac{F_0 T_0}{L_0}. \quad (238)$$

Weak form (234) can then be expressed in the normalized form

$$\delta \bar{\mathbf{x}}^T \bar{\mathbf{f}}(\bar{\mathbf{x}}, \bar{\mathbf{q}}) + \delta \bar{\mathbf{q}}^T \bar{\mathbf{g}}(\bar{\mathbf{x}}) = 0, \quad (239)$$

where a bar denotes normalization with the corresponding scale from above, e.g.

$$\bar{\mathbf{f}}_\sigma^e := \int_{\bar{\Omega}^e} \bar{\sigma}^{\alpha\beta} \bar{\mathbf{N}}_{,\alpha}^T \mathbf{a}_\beta d\bar{a}, \quad (240)$$

with  $\bar{\sigma}^{\alpha\beta} = \sigma^{\alpha\beta}/\mu_0$ ,  $\bar{\mathbf{N}}_{,\alpha} = \mathbf{N}_{,\alpha} L_0$  and  $d\bar{a} = da/L_0^2$ . By choice, parameter  $\xi^\alpha$  is supposed to carry units of length, so that  $\mathbf{a}_\alpha$  and  $a^{\alpha\beta}$  become dimensionless. All the other quantities appearing in (234) are normalized in the same fashion.

If  $F_0$  is defined through  $k = F_0 L_0$  (the bending modulus  $k$  has the unit [force  $\times$  length]), the system is effectively normalized by  $k$ . The non-dimensional material parameters thus are

$$\begin{aligned} \bar{k} &= 1, \\ \bar{k}_g &= k_g/k, \\ \bar{K} &= K L^2/k, \\ \bar{\mu} &= \mu L^2/k, \\ \bar{\epsilon} &= \epsilon L/k, \end{aligned} \quad (241)$$

while the normalization of stress and moment components become

$$\begin{aligned} \bar{q} &= q L^2/k, \\ \bar{\sigma}^{\alpha\beta} &= \sigma^{\alpha\beta} L^2/k, \\ \bar{M}^{\alpha\beta} &= M^{\alpha\beta} L/k. \end{aligned} \quad (242)$$

## 12 Lipid bilayer stabilization

As noted in Secs. 1, 7.4 and 10.5, the lipid bilayer is unstable for quasi-static computations (i.e. when no inertia and viscosity is considered). There are two principal ways to stabilize the system without modifying and affecting the original problem. They are discussed in the following two sections and then summarized in Sec. 12.3. The presentation is taken from Sauer et al. (2017).

## 12.1 Adding stiffness

One way to stabilize the system is to add a stabilization stress  $\sigma_{\text{sta}}^{\alpha\beta}$  to  $\sigma^{\alpha\beta}$  in order to provide additional stiffness. This stress can be defined from a (convex) shear energy or from numerical viscosity. An elegant and accurate option is to add the stabilization stress only to the in-plane contribution (170) while leaving the out-of-plane contribution (171) unchanged. The advantage of this approach is that the out-of-plane part, responsible for the shape of the bilayer, is not affected by the stabilization, at least not in the continuum limit of the discretization. There are several different ways to define the stabilization stress, and they are grouped into two categories. An overview of all the options is then summarized in Tab. 2.

### 12.1.1 In-plane shear and bulk stabilization

The first category goes back to Sauer (2014), who used it to stabilize liquid membranes governed by constant surface tension. The stabilization stress for such membranes requires shear and bulk contributions. Those are given for example by the stabilization stress

$$\sigma_{\text{sta}}^{\alpha\beta} = \mu/J(A^{\alpha\beta} - a^{\alpha\beta}), \quad (243)$$

based on numerical stiffness, and

$$\sigma_{\text{sta}}^{\alpha\beta} = \mu/J(a_{\text{pre}}^{\alpha\beta} - a^{\alpha\beta}), \quad (244)$$

based on numerical viscosity. Here  $a_{\text{pre}}^{\alpha\beta}$  denotes the value of  $a^{\alpha\beta}$  at the preceding computational step. These stabilization stresses are then only included within Eq. (170) and not in Eq. (171), and the resulting two stabilization schemes are denoted ‘A’ (for (243)) and ‘a’ (for (244)) following Sauer (2014). This reference shows that scheme ‘a’ is highly accurate and performs much better than scheme ‘A’. It also shows that applying the stabilization stresses (243) and (244) only to the in-plane part is much more accurate than applying it throughout the system (i.e. in both Eqs. (170) and (171)), which we denote as schemes ‘A-t’ and ‘a-t’.

### 12.1.2 Sole in-plane shear stabilization

If the surface tension is not constant, as in the lipid bilayer models introduced above, only shear stabilization is required. A suitable stabilization stress can be derived from the shear energy

$$\Psi_0 = \frac{\mu}{2}(\widehat{I}_1 - 2), \quad (245)$$

where  $\widehat{I}_1 = I_1/J$  (Sauer et al., 2017). Eqs. (124) and (116) then give

$$\tau_{\text{sta}}^{\alpha\beta} = \frac{\mu}{J}\left(A^{\alpha\beta} - \frac{I_1}{2}a^{\alpha\beta}\right). \quad (246)$$

As before, this stress will only be applied to Eq. (170) and not to Eq. (171), even though it has been derived from a potential and should theoretically apply to both terms. Following earlier nomenclature, this scheme is denoted by ‘A-s’. Replacing  $A^{\alpha\beta}$  by  $a_{\text{pre}}^{\alpha\beta}$  in (246) gives

$$\tau_{\text{sta}}^{\alpha\beta} = \frac{\mu}{J^*}\left(a_{\text{pre}}^{\alpha\beta} - \frac{I_1^*}{2}a^{\alpha\beta}\right), \quad (247)$$

with  $J^* := \sqrt{\det a_{\alpha\beta} / \det a_{\alpha\beta}^{\text{pre}}}$  and  $I_1^* := a_{\text{pre}}^{\alpha\beta} a_{\alpha\beta}$ , which is an alternative shear-stabilization scheme based on numerical viscosity. It is denoted ‘a-s’. If stresses (246) and (247) are applied

throughout the system (i.e. to both (170) and (171)), the corresponding schemes are denoted ‘A-st’ and ‘a-st’.

If the shell is (nearly) area-incompressible the two stabilization methods of Sec. 12.1.1 and 12.1.2 can behave identical, as can be seen by the example in Sec. 12.4.

## 12.2 Normal projection

The second principal way to stabilize the system consists of a simple projection of the formulation onto the solution space defined by the normal surface direction. This step can be applied directly to the discretized formulation as was proposed by Sauer (2014). According to this, for the discrete system of linear equations for displacement increment  $\Delta \mathbf{u}$ , which is given by  $\mathbf{K} \Delta \mathbf{u} = -\mathbf{f}$ , the reduced system for increment  $\Delta \mathbf{u}_{\text{red}} = \mathbf{P} \Delta \mathbf{u}$  is simply obtained as

$$\mathbf{K}_{\text{red}} \Delta \mathbf{u}_{\text{red}} = -\mathbf{f}_{\text{red}}, \quad \mathbf{K}_{\text{red}} := \mathbf{P} \mathbf{K} \mathbf{P}^T, \quad \mathbf{f}_{\text{red}} := \mathbf{P} \mathbf{f}, \quad (248)$$

where

$$\mathbf{P} := \begin{bmatrix} \mathbf{n}_1^T & \mathbf{0}^T & \cdots & \mathbf{0}^T \\ \mathbf{0}^T & \mathbf{n}_2^T & \cdots & \mathbf{0}^T \\ \vdots & \vdots & \ddots & \vdots \\ \mathbf{0}^T & \mathbf{0}^T & \cdots & \mathbf{n}_{n_{\text{no}}}^T \end{bmatrix} \quad (249)$$

is a projection matrix defined by the nodal normal vectors  $\mathbf{n}_I$ . Since this method can lead to distorted FE meshes, a mesh update can be performed by applying any of the stabilization techniques discussed above. If this is followed by a projection step at the same load level, a dependency on parameter  $\mu$  is avoided.

As noted in Sauer et al. (2017), the projection approach does not work very well for surfaces with (near) area-incompressibility, but it does work very well for area-compressible surfaces (Sauer, 2014).

## 12.3 Summary of the stabilization schemes

The nine stabilization schemes presented above are summarized in Tab. 2. They can be grouped

class	scheme	stab. stress $\sigma_{\text{sta}}^{\alpha\beta}/\mu$	application of $\sigma_{\text{sta}}^{\alpha\beta}$	dependence
<b>A</b>	A	$(A^{\alpha\beta} - a^{\alpha\beta})/J$	only in (170)	only on $\mu$
	A-t	$(A^{\alpha\beta} - a^{\alpha\beta})/J$	in (170) & (171)	only on $\mu$
	A-s	$(A^{\alpha\beta} - \frac{1}{2}I_1 a^{\alpha\beta})/J^2$	only in (170)	only on $\mu$
	A-st	$(A^{\alpha\beta} - \frac{1}{2}I_1 a^{\alpha\beta})/J^2$	in (170) & (171)	only on $\mu$
<b>a</b>	a	$(a_{\text{pre}}^{\alpha\beta} - a^{\alpha\beta})/J$	only in (170)	on $\mu$ and $n_t$
	a-t	$(a_{\text{pre}}^{\alpha\beta} - a^{\alpha\beta})/J$	in (170) & (171)	on $\mu$ and $n_t$
	a-s	$(a_{\text{pre}}^{\alpha\beta} - \frac{1}{2}I_1^* a^{\alpha\beta})/J^{*2}$	only in (170)	on $\mu$ and $n_t$
	a-st	$(a_{\text{pre}}^{\alpha\beta} - \frac{1}{2}I_1^* a^{\alpha\beta})/J^{*2}$	in (170) & (171)	on $\mu$ and $n_t$
<b>P</b>	P	0	–	on nodal $\mathbf{n}_I$

Table 2: Summary of the stabilization schemes presented in Secs. 12.1 and 12.2 (Sauer et al., 2017).

into three classes: **A**, **a** and **P**. The schemes of class **A** depend only on  $\mu$  but require this value

to be quite low. The schemes of class **a** also depend on the number of computational steps,  $n_t$ . If this number is high, the schemes provide stiffness without adding much stress. The shell is then stabilized without modifying the solution much, even when  $\mu$  is high. Scheme ‘P’ depends on the nodal projection vector  $\mathbf{n}_I$ , which is usually taken as the surface normal. The performance of the different stabilization schemes is investigated in the following section.

## 12.4 Performance of the stabilization schemes

Two examples are considered in order to examine the performance of the proposed stabilization schemes. They are based on the two analytical examples presented in Sec. 9.

### 12.4.1 Pure bending and stretching of a flat sheet

The first example considers the pure bending and stretching of a flat sheet. The analytical solution for this problem is given in Sec. 9.1. The problem is solved numerically using the

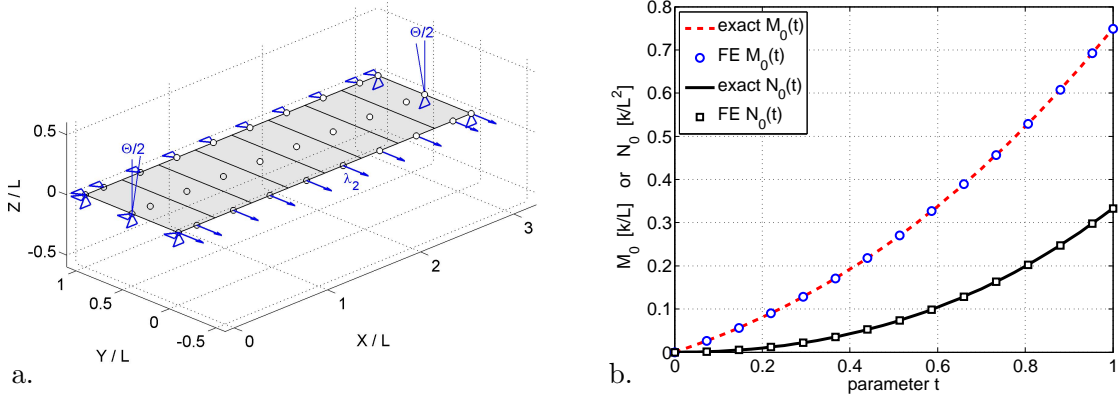


Figure 9: Pure bending and stretching of a sheet (Sauer et al., 2017): a. initial FE configuration and boundary conditions (discretized with  $m = 8$  elements); b. distributed boundary moment  $M_0(t)$  and normal traction  $N_0(t)$  as obtained analytically and computationally for the area-incompressible model (142).

computational setup shown in Fig. 9. The FE mesh is discretized by  $m$  elements along  $X$ . The parameter  $t$  is introduced to apply the rotation  $\Theta = t\pi/6$  and stretch  $\lambda_2 = 1 + t/2$  by increasing  $t$  linearly from 0 to 1 in  $n_t$  steps, where  $n_t$  is chosen as a multiple of  $m$ . The mean curvature then follows as  $H = \Theta/(2\lambda_1 S)$ . Numerically, the rotation is applied according to (228) considering the penalty parameter  $\epsilon = 100 m k/L$ . Fig. 9b shows the FE solution and analytical solution for the bending moment  $M_0(t)$  and the stress  $N_0(t)$ , normalizing  $M_0$  by  $k/L$  and  $N_0$  by  $k/L^2$ .

Next, the accuracy of the different stability schemes is studied in detail by examining the  $L_2$ -error of the solution, defined by

$$L_2 := \sqrt{\frac{1}{SL} \int_{S_0} \|\mathbf{u}_{\text{exact}} - \mathbf{u}_{\text{FE}}\|^2 dA}, \quad (250)$$

and the error in  $M$  and  $N$ , defined by

$$E_{MN} := \frac{|M_{\text{exact}} - M_{\text{FE}}|}{M_{\text{exact}}} + \frac{|N_{\text{exact}} - N_{\text{FE}}|}{N_{\text{exact}}}, \quad (251)$$

where  $M_{FE}$  and  $N_{FE}$  are the computed mean values along the respective boundaries. The first error is a measure of the kinematic accuracy, while the second is a measure of the kinetic accuracy. Fig. 10 shows the two errors for the area-incompressible model of Eq. (142). Looking

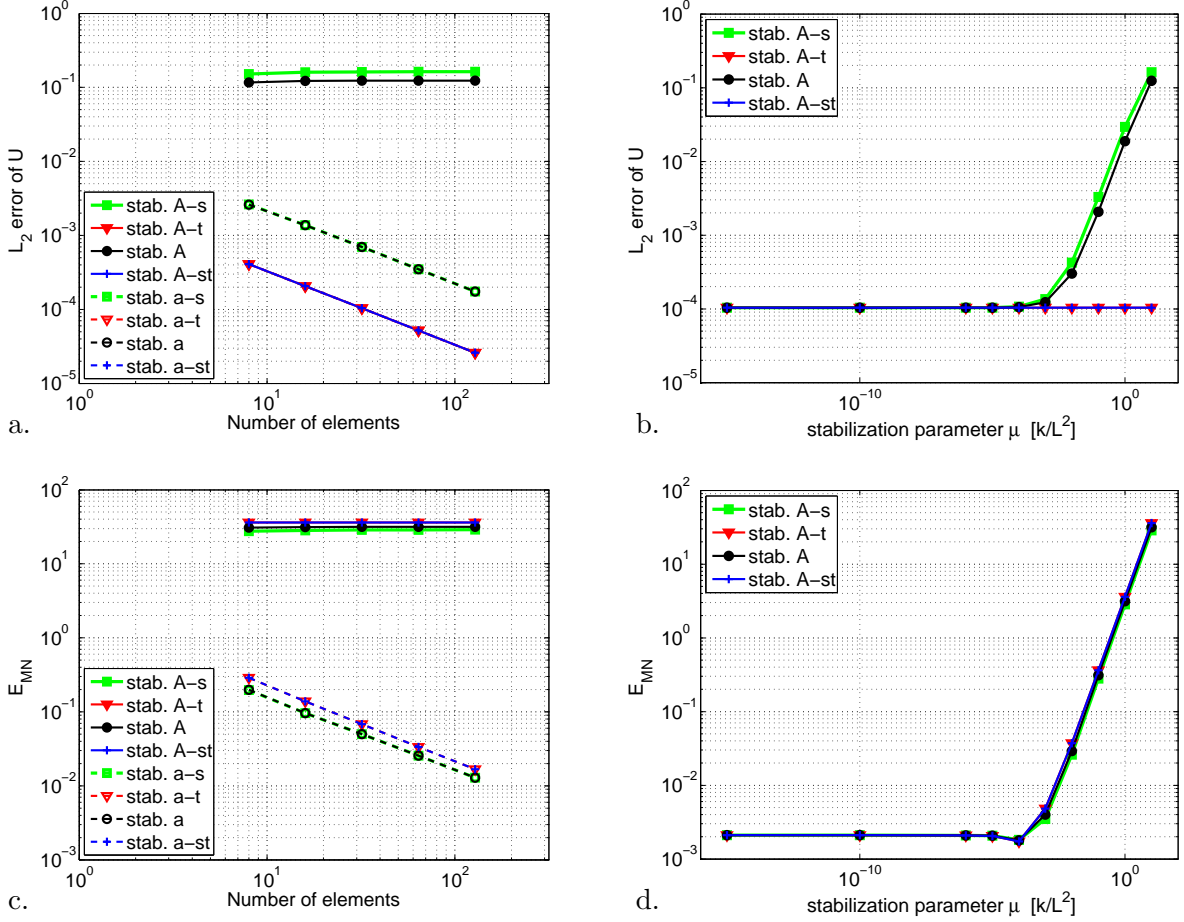


Figure 10: Pure bending and stretching of a sheet (Sauer et al., 2017): accuracy for the area-incompressible model (142): a.  $L_2$ -error vs.  $m$  considering stabilization classes **A** and **a** with  $\bar{\mu} = 10$  and  $n_t = 12.5m$ ; b.  $L_2$ -error vs.  $\mu$  considering stabilization class **A** with  $m = 32$ ; c.-d. same as a.-b., but now for error  $E_{MN}$ . Considered is  $\Theta/2 = \pi/3$  and  $\lambda_2 = 1.5$ .

at the  $L_2$ -error, schemes ‘A-t’, ‘A-st’, ‘a-t’ and ‘a-st’ perform best. In case of error  $E_{NM}$ , schemes ‘a’ and ‘a-s’ perform best. Class **A** generally converges with  $\mu$ , but it may not converge with the number of elements for high values of  $\mu$ . Interestingly, the  $L_2$ -error of scheme ‘A-t’ and ‘A-st’ is not affected by  $\mu$ , as schemes ‘A’ and ‘A-s’ are. For sufficiently low  $\mu$  (for  $m = 32$  about  $\bar{\mu} < 10^{-3}$ ), the accuracy of class **A** (both in  $L_2$  and  $E_{MN}$ ) reaches that of class **a** and then only improves with mesh refinement. Class **A** with low  $\mu$  may even surpass class **a** with high  $\mu$ . But generally, class **a** is more accurate and robust (as  $\mu$  does not need to be very small). There is no clear favorite in class **a** for this test case.

As the plots show, not a single stabilization scheme stands out here and the accuracy depends both on the model and the error measure. In general, all schemes are suitable to solve the problem. If class **A** is used, the value of  $\mu$  needs to be suitably low. For class **a** even large values for  $\mu$  can be used. In this example it is even possible to set  $\mu = 0$  in the code. This works since the effective shear stiffness according to (151) is positive here, i.e.  $\mu_{\text{eff}} = 3JkH^2/2 > 0$ . For other problems  $\mu_{\text{eff}}$  can be negative, and stabilization is required.

## 12.4.2 Inflation of a sphere

The second example considers the inflation of a spherical cell. Contrary to the previous example, the FE mesh now also contains interfaces between NURBS patches. Since the surface area increases during inflation, potential (140) is considered. Fig. 11 shows the computational setup of the problem. The computational domain consists of a quarter sphere discretized with four

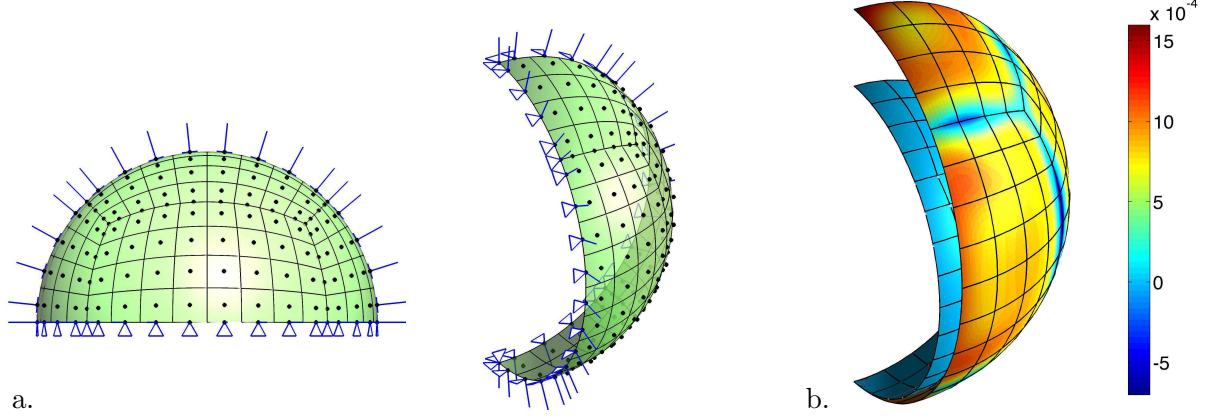


Figure 11: Sphere inflation (Sauer et al., 2017): a. initial FE configuration and boundary conditions (for mesh  $m = 8$ ); b. current FE configuration for an imposed volume of  $\bar{V} = 2$  compared to the initial configuration; the colors show the relative error in the surface tension  $T_\nu$ .

NURBS patches. The quarter sphere contains  $3m^2/2$  elements where  $m$  is the number of elements along the equator of the quarter sphere. At the boundaries and at the patch interfaces  $C^1$ -continuity is enforced using (228) with  $\epsilon = 4000mk/R$ . The area bulk modulus is taken as  $K = 5k/R^2$ , while  $k_g$  is taken as zero. Two cases are considered:  $H_0 = 0$  and  $H_0 = 1/R$ . Fig. 12 shows that the computational  $p(V)$ -data converge to the exact analytical result of (195). Here

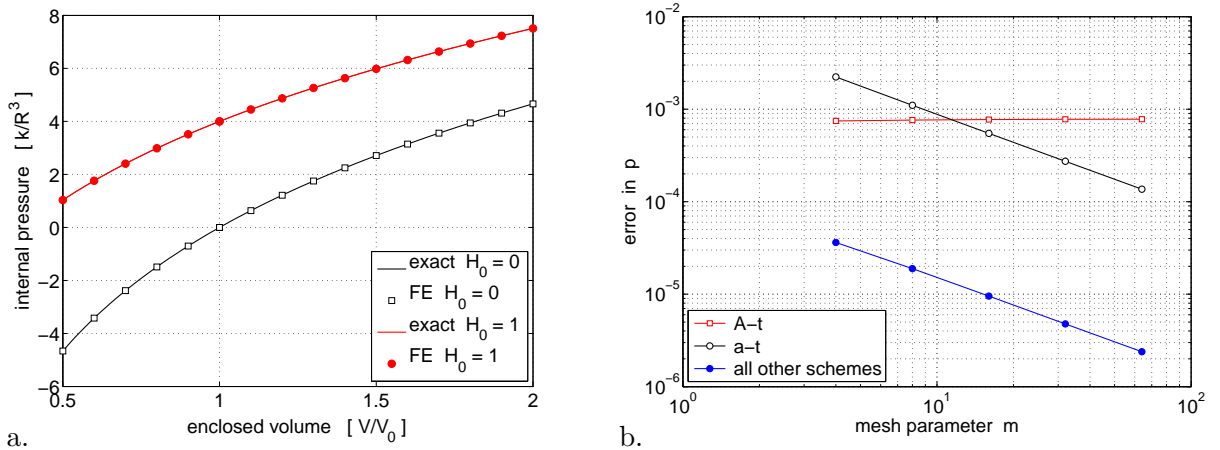


Figure 12: Sphere inflation (Sauer et al., 2017): a. pressure-volume relation; b. FE convergence for the different stabilization schemes.

the pressure error

$$e_p = \frac{|p_{\text{exact}} - p_{\text{FE}}|}{p_{\text{exact}}} \quad (252)$$

is examined for  $H_0 = 1/R$  and  $\bar{V} = 2$  considering the 9 stabilization schemes of Tab. 2 with  $\bar{\mu} = 0.01$  for class **A** and  $\bar{\mu} = 1$  and  $n_t = 5m$  for class **a**. For schemes ‘A’, ‘A-s’, ‘A-st’, ‘a’, ‘a-s’, ‘a-st’ and ‘P’ this error converges nicely (and is indistinguishable in the figure). Only schemes ‘A-t’ and ‘a-t’ behave significantly different. They introduce further errors that only converge if  $\mu$  is decreased or  $n_t$  is increased. The reason why all other schemes have equal error, is that here the error is actually determined by the penalty parameter  $\epsilon$  used within patch constraint (228). The error stemming from the stabilization methods (apart from ‘A-t’ and ‘a-t’) is insignificant compared to that. It is interesting to note that ‘A-st’ and ‘a-st’ perform much better than ‘A-t’ and ‘a-t’, even though no shear is present in the analytical solution. ‘A-st’ and ‘a-st’ can therefore be considered as the best choices here, since they are the most efficient schemes to implement.

We finally note that for a sphere  $\mu_{\text{eff}} = JkH(H - H_0)$ , where  $H = -1/r$ . Thus  $\mu_{\text{eff}} > 0$  for  $H < H_0$ , which is the case here.

## 13 Numerical examples

This section presents three numerical examples based on the computational formulation presented in the preceding three sections. The first two examples are taken from Sauer et al. (2017). The third example is new.

### 13.1 Bilayer tethering

If a surface point of the bilayer is pulled in normal direction  $\mathbf{n}$ , a thin tether forms, e.g. see Cuvelier et al. (2005). In order to simulate the tether drawing process, the setup of Fig. 13 is considered. The bilayer membrane is modeled as a circular, initially flat disc with initial radius

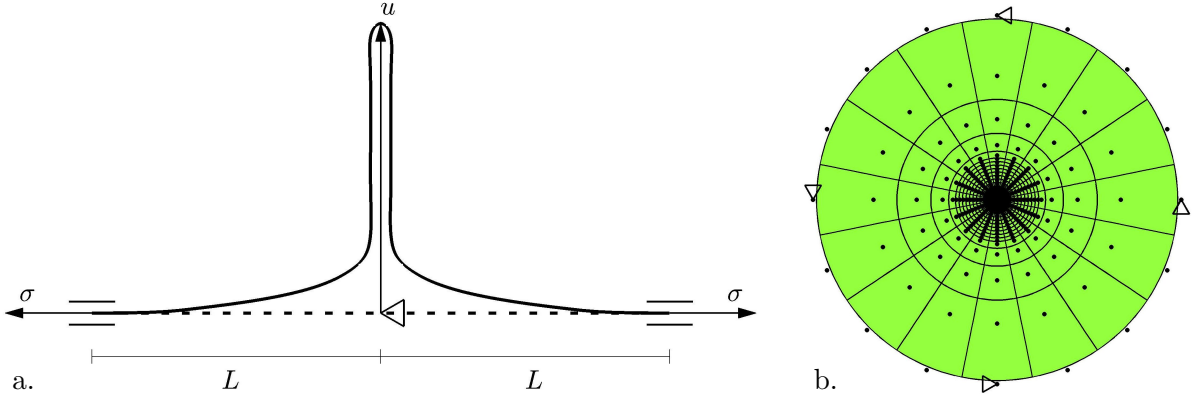


Figure 13: Bilayer tethering (Sauer et al., 2017): a. boundary conditions and b. coarse FE mesh of the initial configuration.

$L$ . The effect of the surrounding membrane is captured by the boundary tension  $\sigma$  (measured w.r.t. the current boundary length). The surface is described by material model (140).  $L$  and  $k$  are used for normalization. The remaining material parameters are chosen as  $k_g = -0.7k$  and  $K = 20,000k/L^2$ . The cases  $\sigma \in \{100, 200, 400, 800\}k/L^2$  are considered. Stabilization scheme ‘A-s’ is used with  $\mu = 0.1k/L^2$ . The bilayer is clamped at the boundary, but free to move in the in-plane direction. The traction  $\mathbf{t} = \sigma\boldsymbol{\nu}$  is imposed and applied numerically via (217.2). Even though  $\mathbf{t}$  is constant during deformation, the boundary length  $ds$  appearing in  $\mathbf{f}_t^e$

changes and has to be linearized (Sauer, 2014). At the center, the displacement  $u$  is imposed on the initially flat, circular surface.

Fig. 13b also shows one of the chosen finite element discretizations of the initial configuration. Quadratic, NURBS-based,  $C^1$ -continuous finite elements are used. A finer discretization is chosen at the center, where the tube is going to form. The chosen NURBS discretization degenerates at the center, such that the  $C^1$ -continuity is lost there. It is regained if displacement  $u$  is applied not only to the central control point but also to the first ring of control points around the center. This ensures that the tangent plane remains horizontal at the tip. Likewise, a horizontal tangent is enforced at the outer boundary by fixing the height of the outer two rings of control points.

Fig. 14 shows the deformed surface for  $u = L$  with  $\bar{\sigma} = 100$  and  $\bar{\sigma} = 800$ . Further cases are

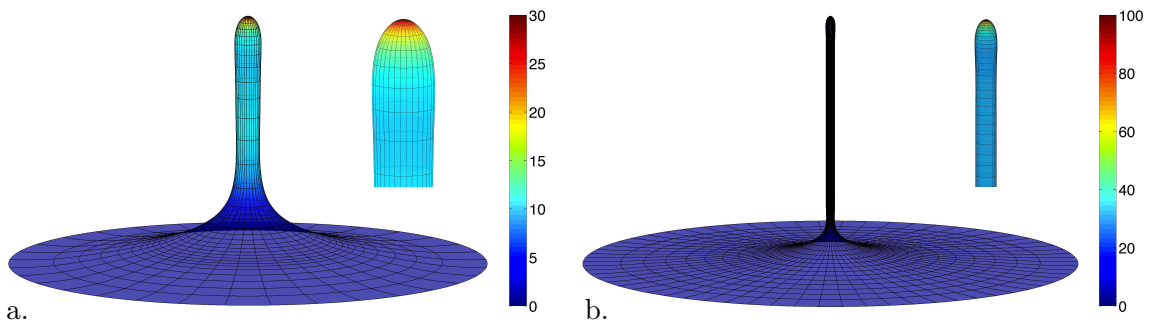


Figure 14: Bilayer tethering (Sauer et al., 2017): Results for a.  $\sigma = 100k/L^2$  and b.  $\sigma = 800k/L^2$ ; the colors show the mean curvature  $H$  normalized by  $L^{-1}$ .

shown in Sauer et al. (2017). The surface tension affects the slenderness of the appearing tube. Derényi et al. (2002) showed from theoretical considerations<sup>9</sup> that the tube radius is

$$a = \frac{1}{2} \sqrt{\frac{k}{\sigma}}, \quad (253)$$

while the steady force during tube drawing is

$$P_0 = 2\pi\sqrt{\sigma k}. \quad (254)$$

These values are confirmed by the computations, as is shown in Fig. 15. The left side shows the force-displacement relation during drawing. Oscillations appear in the numerical solution due to the mesh discretization error. They are more pronounced for more slender tubes, as the black curve in Fig. 15a shows. They disappear upon mesh refinement, as the solution converges. The convergence of  $P_0$  for  $\sigma = 200k/L^2$  and  $u = L$  ( $= 28.28a$ ) is shown in Fig. 15b by examining the error

$$e(P_0^{\text{FE}}) := \frac{|P_0^{\text{ref}} - P_0^{\text{FE}}|}{P_0^{\text{ref}}}, \quad (255)$$

where  $P_0^{\text{ref}}$  is the FE solution for  $m = 256$  and  $\mu = 0$ . Different values of stability parameter  $\mu$  are considered. Even the case  $\mu = 0$  works, due to the inherent shear stiffness of the Helfrich model given in (151). In all cases, the error reported in Fig. 15b is assessed by comparison to the finest FE mesh. From this one can find that the analytical solution itself has an error of about 0.2%, due to its underlying assumptions.

<sup>9</sup>Assuming that the tube is sufficiently long and can be idealized by a perfect cylinder.

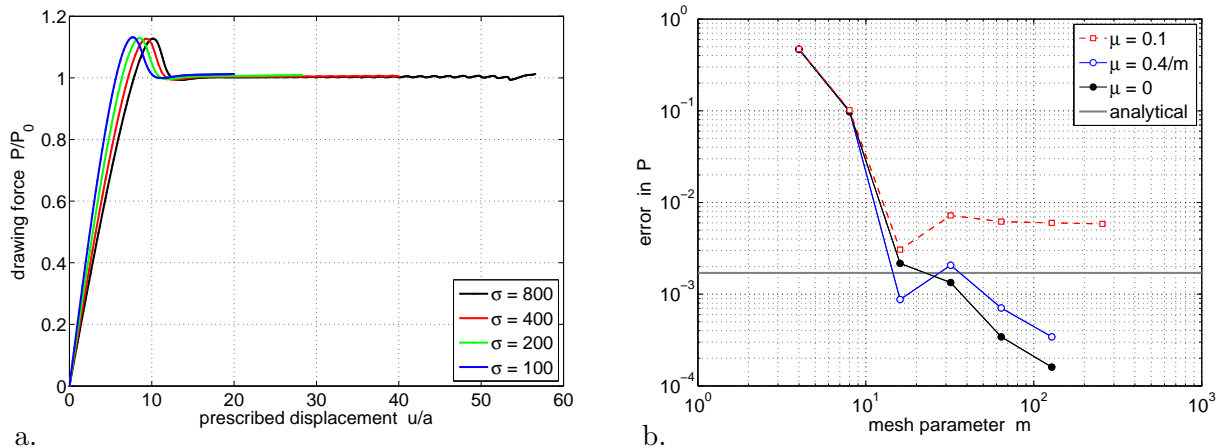


Figure 15: Bilayer tethering (Sauer et al., 2017): a. load-displacement curve; b. FE convergence.

### 13.2 Bilayer budding

The adsorption of proteins can lead to shape change in lipid bilayers (Zimmerberg and Kozlov, 2006; McMahon and Gallop, 2005; Kozlov et al., 2014; Shi and Baumgart, 2015). The lipid membrane deforms whenever its curvature is incompatible with the inherent structure of a protein, giving rise to a spontaneous curvature. In order to study this, a hemi-spherical cell with initial radius  $R$  and curvature  $H = -1/R$  is considered. The cell surface is clamped at the boundary, but free to expand radially as is shown in Fig. 16. On the top of the cell,

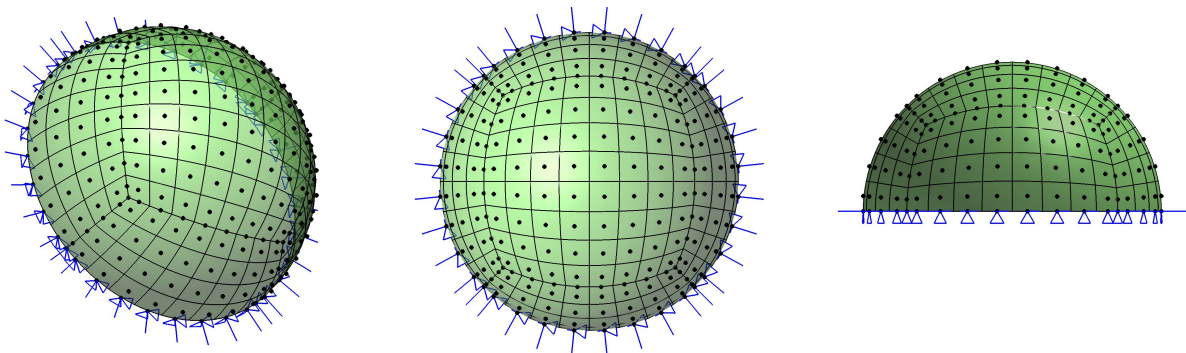


Figure 16: Bilayer budding (Sauer et al., 2017): Considered setup showing the initial configuration, FE discretization and boundary conditions. The surface normal at the boundary is fixed and the boundary nodes are only free to move in the radial direction.

within the circular region of radius  $0.2R$ , a constant spontaneous curvature  $\bar{H}_0$  is prescribed in a Lagrangian fashion, such that the proteins causing  $H_0$  move along with the lipid bilayer and no diffusion occurs. Unless otherwise specified, model (140) is used with the material parameters  $\bar{k}_g = -0.7$  and  $\bar{K} = 10,000$ , while  $k$  and  $R$  are used for normalization according to Sec. 11.4 and remain unspecified. Further, stabilization scheme ‘A-s’ is used with  $\bar{\mu} = 0.01$ . The FE discretization shown in Fig. 16, consisting of five NURBS patches, is used. Where the patches meet, constraint (228) is added to ensure rotational continuity and moment transfer. Constraint (228) is also used to fix the surface normal at the boundary. The actual FE mesh is much finer than in Fig. 16 and uses 12288 elements (64 times more than in the figure).

In past numerical studies, axisymmetric bud shapes have been reported, e.g. Walani et al. (2015).

These shapes should be a natural solution due to the axisymmetry of the problem. However, as is shown below, non-axisymmetric solutions are also possible, and can be energetically favorable, indicating that axisymmetric solutions can become unfavored. This is illustrated by considering

case	bud shape	$H_0$ region	stabilization	$\bar{\mu}$	in-plane stress
a	axisym.	circle	A-s	0.01	hydro-static
b	general	ellipse	A-st	10	elastic shear
c	general	ellipse	a-st	1250	viscous shear

Table 3: Bilayer budding: different physical test cases considered.

the three different test cases listed in Tab. 3 and discussed in the following:

**Case a.** (Fig. 17a): Here, the deformation is constrained to remain axisymmetric (i.e. the FE nodes are only allowed to move in radial direction). The resulting deformation at  $\bar{H}_0 = -25$  is shown in Fig. 17a.

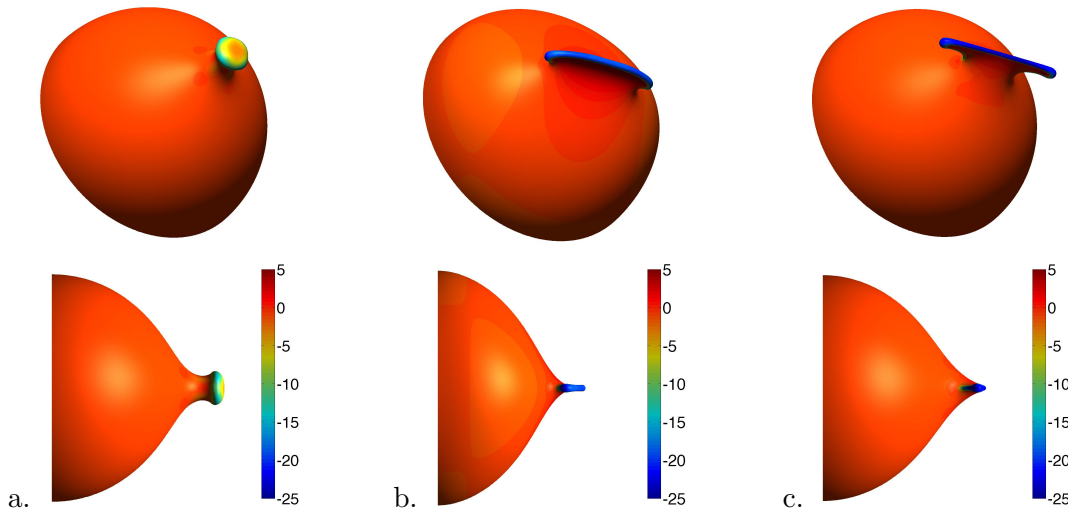


Figure 17: Bilayer budding (Sauer et al., 2017): a. axisymmetric case, b. shear stiff case, and c. viscous case at  $\bar{H}_0 = -25$ . The colors show the mean curvature  $\bar{H}$ .

**Case b.** (Fig. 17b): Here, the deformation is not constrained to remain axisymmetric. Consequently, a non-axisymmetric bud shape appears. To induce it,  $H_0$  is prescribed within an imperfect circle, i.e. an ellipse with half-axes  $a = 0.22R$  and  $b = 0.18R$ . It is energetically favorable for the bud to evade into an elongated plate-like shape (see Fig. 17b). To counter this, shear resistance is provided by elastic shear stresses according to model ‘A-st’<sup>10</sup>.

**Case c.** (Fig. 17c): Here, the deformation is also not constrained to remain axisymmetric.  $H_0$  is again prescribed within an imperfect circle ( $a = 0.22R$  and  $b = 0.18R$ ). But now shear resistance is provided through physical viscosity. This is captured through model ‘a-st’ using the relation  $\eta = \mu \Delta t$  with  $\bar{\mu} = 1250$  and a load stepping increment for  $H_0$  of  $\Delta \bar{H}_0 = 0.02$  (such that  $\eta = 25k/L^3/\dot{H}_0$ , where  $\dot{H}_0$  is the rate with which the spontaneous curvature is prescribed). As Fig. 17c shows, the bud splits into two separate buds.

In Sauer et al. (2017) movies can be found that animate the bud growth for the three cases. One of the advantages of the proposed finite element formulation is that the surface tension  $\gamma$  can be studied. This is shown in Fig. 18. As seen the surface tension is not a constant. At extreme

<sup>10</sup>The shear stresses are now physical and need to be applied both in-plane and out-of-plane.

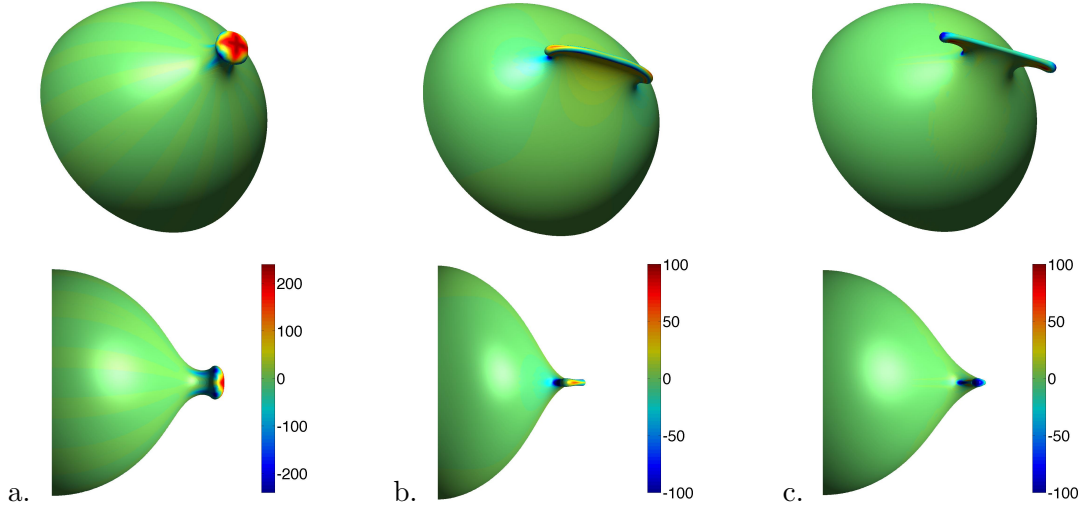


Figure 18: Bilayer budding (Sauer et al., 2017): a. axisymmetric case, b. shear stiff case, and c. viscous case at  $\bar{H}_0 = -25$ . The colors show the normalized surface tension  $\bar{\gamma}$ .

values of  $\gamma$ , rupture might occur, depending on the strength of the lipid bilayer. Further details on bilayer budding are discussed Sauer et al. (2017).

### 13.3 Bilayer indentation

The preceding two examples show that liquid shells, such as lipid bilayers, exhibit out-of-plane deformations that are very different to those observed for solid shells. This is also seen during indentation, which is considered in the following. An initially flat, square bilayer sheet with size  $2L \times 2L$  is brought into normal contact with a spherical indenter. The sheet is considered to be area-extensible such that it can be clamped at the edge. The considered model parameters are  $\bar{k}_g = -0.83$  and  $\bar{K} = 7.60 \cdot 10^5$ , using stabilization scheme ‘a-s’ with  $\bar{\mu} = 12.20$ . Contact is described by the penalty method, according to which the contact pressure is given by

$$p_c = \begin{cases} -\epsilon_n g_n & \text{if } g_n < 0, \\ 0 & \text{else,} \end{cases} \quad (256)$$

where  $\epsilon_n$  is the contact penalty parameter and

$$g_n = (\mathbf{x} - \mathbf{x}_0) \cdot \mathbf{n}_0 - R_0 \quad (257)$$

denotes the normal gap between sphere and bilayer surface. Here,  $\mathbf{x} \in \mathcal{S}$  denotes a surface point, while  $R_0$ ,  $\mathbf{x}_0$  and  $\mathbf{n}_0$  denote radius, center and surface normal of the sphere. In the example,  $\bar{R}_0 = 0.1$  and  $\bar{\epsilon}_n = 7.60 \cdot 10^8$  is used.

Fig. 19 shows the deformation of the bilayer sheet for an indentation depth of  $0.4L$ . The problem is symmetric, and therefore the finite element computations are performed on one quarter of the sheet. Along the symmetry boundaries, constraint (228) is used in order to enforce continuity of  $\mathbf{n}$ . The continuity of  $\mathbf{n}$  across the symmetry boundary is confirmed by the inset shown on the right.

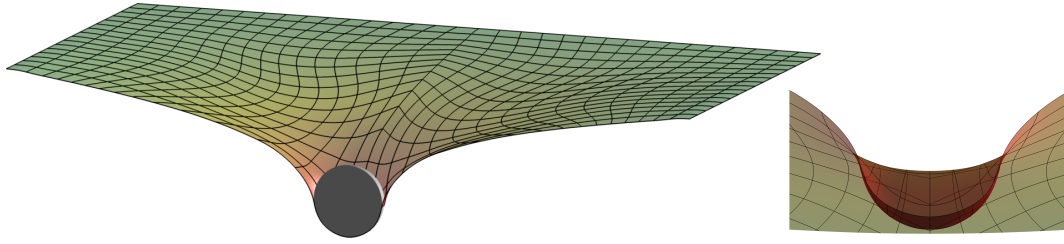


Figure 19: Indentation of a square bilayer sheet by a spherical indenter. The inset on the right shows that the surface remains smooth during deformation. Only half of the system is shown.

## 14 Conclusion

This chapter discusses the computational modeling of lipid bilayers based on thin-shell theory. Various model ingredients are presented in order to address the challenges of this. Those ingredients range from theoretical approaches that provide a general description of balance laws, constitution, kinematics and weak form based on curvilinear coordinates, to computational methods, such as nonlinear finite element analysis, NURBS-based surface discretizations, LBB-conforming mixed methods, and shear stabilization. A necessary component of this is the consistent linearization of the formulation. The proposed formulation is illustrated by several analytical and numerical examples. The analytical examples are used to examine the behavior of the proposed shear stabilization schemes. The constitutive behavior of the bilayer is based on the Helfrich bending model combined with in-plane viscosity and (near) area-incompressibility. Neglecting inertia leads to a nonlinear PDE that is fourth order in space and first order in time. The corresponding weak form is second order in space and first order in time. This requires globally  $C^1$ -continuous surface discretizations. Those are provided by NURBS-based FE shape functions together with rotational constraints at patch interfaces.

The generality of the proposed formulation admits many possible extensions. One is the generalization of the bilayer kinematics to account for tilt and inter-layer sliding. Another is the consideration of mass-varying systems (Sahu et al., 2017). Further extension are the development of surface-ALE formulations, and local mesh refinement in the framework of LR-NURBS (Zimmermann and Sauer, 2017).

## Acknowledgements

The author is grateful to the German Research Foundation (DFG) for supporting this research under grants GSC 111 and SA1822/5-1. The author also wishes to thank Kranthi Mandadapu, Thang Duong and Amaresh Sahu for their valuable comments, and Yannick Omar for his help with the example in Sec. 13.3. Special thanks also go to David Steigmann for organizing the CISM summer school that led to this article.

## References

- Agrawal, A. and Steigmann, D. (2009). Modeling protein-mediated morphology in biomembranes. *Biomech. Model. Mechanobiol.*, **8**(5):371–379.
- Arroyo, M. and DeSimone, A. (2009). Relaxation dynamics of fluid membranes. *Phys. Rev. E*, **79**:031915.

- Babuška, I. (1973). The finite element method with Lagrangian multipliers. *Num. Math.*, **20**:179–192.
- Baesu, E., Rudd, R. E., Belak, J., and McElfresh, M. (2004). Continuum modeling of cell membranes. *Int. J. Non-lin. Mech.*, **39**:369–377.
- Bathe, K.-J. (1996). *Finite Element Procedures*. Prentice-Hall, New Jersey.
- Bathe, K.-J. (2001). The inf-sup condition and its evaluation for mixed finite element methods. *Comput. Struct.*, **79**:243–252.
- Benson, D. J., Bazilevs, Y., Hsu, M.-C., and Hughes, T. J. R. (2011). A large deformation, rotation-free, isogeometric shell. *Comput. Methods Appl. Mech. Engrg.*, **200**(13-16):1367–1378.
- Borden, M. J., Scott, M. A., Evans, J. A., and Hughes, T. J. R. (2011). Isogeometric finite element data structures based on Bezier extraction of NURBS. *Int. J. Numer. Meth. Engrg.*, **87**:15–47.
- Canham, P. B. (1970). The minimum energy of bending as a possible explanation of the biconcave shape of the human red blood cell. *J. Theoret. Biol.*, **26**:61–81.
- Cirak, F. and Ortiz, M. (2001). Fully  $C^1$ -conforming subdivision elements for finite element-deformation thin-shell analysis. *Int. J. Numer. Meth. Engrg.*, **51**:813–833.
- Coleman, B. D. and Noll, W. (1964). The thermodynamics of elastic materials with heat conduction and viscosity. *Arch. Ration. Mech. Anal.*, **13**:167–178.
- Corbett, C. J. (2016). *Isogeometric Finite Element Enrichment for Problems Dominated by Surface Effects*. PhD thesis, RWTH Aachen University, Aachen, Germany.
- Cottrell, J. A., Hughes, T. J. R., and Bazilevs, Y. (2009). *Isogeometric Analysis*. Wiley.
- Cuvelier, D., Derényi, I., Bassereau, P., and Nassoy, P. (2005). Coalescence of membrane tethers: Experiments, theory, and applications. *Biophys. J.*, **88**:2714–2726.
- Dao, M., Lim, C. T., and Suresh, S. (2003). Mechanics of the human red blood cell deformed by optical tweezers. *J. Mech. Phys. Solids*, **51**:2259–2280.
- Derényi, I., Jülicher, F., and Prost, J. (2002). Formation and interaction of membrane tubes. *Phy. Rev. Lett.*, **88**(23):238101.
- Du, Q. and Wang, X. Q. (2007). Convergence of numerical approximations to a phase field bending elasticity model of membrane deformations. *Int. J. Numer. Anal. Model.*, **4**(3-4):441–459.
- Dung, N. T. and Wells, G. N. (2008). Geometrically nonlinear formulation for thin shells without rotation degrees of freedom. *Comput. Methods Appl. Mech. Engrg.*, **197**:2778–2788.
- Duong, T. X., Roohbakhshan, F., and Sauer, R. A. (2017). A new rotation-free isogeometric thin shell formulation and a corresponding continuity constraint for patch boundaries. *Comput. Methods Appl. Mech. Engrg.*, **316**:43–83.
- Elliott, C. M. and Stinner, B. (2010). Modeling and computation of two phase geometric biomembranes using surface finite elements. *J. Comput. Phys.*, **229**(18):6585–6612.

- Feng, F. and Klug, W. S. (2006). Finite element modeling of lipid bilayer membranes. *J. Comput. Phys.*, **220**:394–408.
- Flores, F. G. and Estrada, C. F. (2007). A rotation-free thin shell quadrilateral. *Comput. Methods Appl. Mech. Engrg.*, **196**(25-28):2631–2646.
- Gu, R., Wang, X., and Gunzburger, M. (2014). Simulating vesicle-substrate adhesion using two phase field functions. *J. Comput. Phys.*, **275**:626–641.
- Helfrich, W. (1973). Elastic properties of lipid bilayers: Theory and possible experiments. *Z. Naturforsch.*, **28c**:693–703.
- Hughes, T. J. R., Cottrell, J. A., and Bazilevs, Y. (2005). Isogeometric analysis: CAD, finite elements, NURBS, exact geometry and mesh refinement. *Comput. Methods Appl. Mech. Engrg.*, **194**:4135–4195.
- Jarić, M., Seifert, U., Wirtz, W., and Wortis, M. (1995). Vesicular instabilities: The prolate-to-oblate transition and other shape instabilities of fluid bilayer membranes. *Phys. Rev. E*, **52**(6):6623–6634.
- Jenkins, J. T. (1977). The equations of mechanical equilibrium of a model membrane. *SIAM J. Appl. Math.*, **32**(4):755–764.
- Jie, Y., Quanhui, L., Jixing, L., and Zhong-Can, O.-Y. (1998). Numerical observation of non-axisymmetric vesicles in fluid membranes. *Phys. Rev. E*, **58**(4):4730–4736.
- Johannessen, K. A., Kvamsdal, T., and Dokken, T. (2014). Isogeometric analysis using LRB-splines. *Comput. Methods Appl. Mech. Engrg.*, **269**:471–514.
- Kahraman, O., Stoop, N., and Müller, M. M. (2012). Fluid membrane vesicles in confinement. *New J. Phys.*, **14**:095021.
- Kiendl, J., Bazilevs, Y., Hsu, M.-C., Wüchner, R., and Bletzinger, K.-U. (2010). The bending strip method for isogeometric analysis of Kirchhoff-Love shell structures comprised of multiple patches. *Comput. Methods Appl. Mech. Engrg.*, **199**(37-40):2403–2416.
- Kiendl, J., Bletzinger, K.-U., Linhard, J., and Wüchner, R. (2009). Isogeometric shell analysis with Kirchhoff-Love elements. *Comput. Methods Appl. Mech. Engrg.*, **198**:3902–3914.
- Kiendl, J., Hsu, M.-C., Wu, M. C., and Reali, A. (2015). Isogeometric Kirchhoff-Love shell formulations for general hyperelastic materials. *Comput. Methods Appl. Mech. Engrg.*, **291**:280–303.
- Kloppel, T. and Wall, W. A. (2011). A novel two-layer, coupled finite element approach for modeling the nonlinear elastic and viscoelastic behavior of human erythrocytes. *Biomech. Model. Mechanobiol.*, **10**(4):445–459.
- Kozlov, M. M., Campelo, F., Liska, N., Chernomordik, L. V., Marrink, S. J., and McMahon, H. T. (2014). Mechanisms shaping cell membranes. *Current opinion in cell biology*, **29**:53–60.
- Lau, C., Brownell, W. E., and Spector, A. A. (2012). Internal forces, tension and energy density in tethered cellular membranes. *J. Biomech.*, **45**(7):1328–1331.
- Li, H. and Lykotrafitis, G. (2012). Two-component coarse-grained molecular-dynamics model for the human erythrocyte membrane. *Biophys. J.*, **102**(1):75–84.

- Libai, A. and Simmonds, J. G. (1998). *The Nonlinear Theory of Elastic Shells*. Cambridge University Press, Cambridge, 2<sup>nd</sup> edition.
- Linhard, J., Wüchner, R., and Bletzinger, K.-U. (2007). “Upgrading” membranes to shells - The CEG rotation free element and its application in structural analysis. *Finite Elem. Anal. Des.*, **44**(1-2):63–74.
- Lipowsky, R. (2013). Spontaneous tabulation of membranes and vesicles reveals membrane tension generated by spontaneous curvature. *Faraday Discuss.*, **161**:305–331.
- Loc, T. V., Chien, T. H., and Hung, N. X. (2013). On two-field nurbs-based isogeometric formulation for incompressible media problems. *Vietnam Journal of Mechanics*, **35**:225 – 237.
- Ma, L. and Klug, W. S. (2008). Viscous regularization and r-adaptive meshing for finite element analysis of lipid membrane mechanics. *J. Comput. Phys.*, **227**:5816–5835.
- McMahon, H. T. and Gallop, J. L. (2005). Membrane curvature and mechanisms of dynamic cell membrane remodelling. *Nature*, **438**(7068):590–596.
- Naghdi, P. M. (1982). Finite deformation of elastic rods and shells. In Carlson, D. E. and Shields, R. T., editors, *Proceedings of the IUTAM Symposium on Finite Elasticity*, pages 47–103, The Hague. Martinus Nijhoff Publishers.
- Nguyen-Thanh, N., Kiendl, J., Nguyen-Xuan, H., Wüchner, R., Bletzinger, K.-U., Bazilevs, Y., and Rabczuk, T. (2011). Rotation free isogeometric thin shell analysis using pht-splines. *Comput. Methods Appl. Mech. Engrg.*, **200**(47-48):3410–3424.
- Peng, Z., Asaro, R. J., and Zhu, Q. (2010). Multiscale simulation of erythrocyte membranes. *Phys. Rev. E*, **81**:031904.
- Pietraszkiewicz, W. (1989). Geometrically nonlinear theories of thin elastic shells. *Advances Mech.*, **12**(1):51–130.
- Rahimi, M. and Arroyo, M. (2012). Shape dynamics, lipid hydrodynamics, and the complex viscoelasticity of bilayer membranes. *Phys. Rev. E*, **86**:011932.
- Ramakrishnan, N., Kumar, P. B. S., and Ipsen, J. H. (2010). Monte carlo simulations of fluid vesicles with in-plane orientational ordering. *Phys. Rev. E*, **81**:041922.
- Rangamani, P., Agrawal, A., Mandadapu, K. K., Oster, G., and Steigmann, D. J. (2013). Interaction between surface shape and intra-surface viscous flow on lipid membranes. *Biomech. Model. Mechanobiol.*, **12**(4):833–845.
- Rangamani, P., Mandadapu, K. K., and Oster, G. (2014). Protein-induced membrane curvature alters local membrane tension. *Biophysical journal*, **107**(3):751–762.
- Rangarajan, R. and Gao, H. (2015). A finite element method to compute three-dimensional equilibrium configurations of fluid membranes: Optimal parameterization, variational formulation and applications. *J. Comput. Phys.*, **297**:266–294.
- Rim, J. E., Purohit, P. K., and Klug, W. S. (2014). Mechanical collapse of confined fluid membrane vesicles. *Biomech. Model. Mechanobiol.*, **13**(6):1277–1288.
- Rosolen, A., Peco, C., and Arroyo, M. (2013). An adaptive meshfree method for phase-field models of biomembranes. Part I: Approximation with maximum-entropy basis functions. *J. Comput. Phys.*, **249**:303–319.

- Sahu, A., Sauer, R. A., and Mandadapu, K. K. (2017). The irreversible thermodynamics of curved lipid membranes. <https://arxiv.org/1701.06495>.
- Salac, D. and Miksis, M. (2011). A level set projection model of lipid vesicles in general flows. *J. Comput. Phys.*, **230**(22):8192–8215.
- Sauer, R. A. (2014). Stabilized finite element formulations for liquid membranes and their application to droplet contact. *Int. J. Numer. Meth. Fluids*, **75**(7):519–545.
- Sauer, R. A. and De Lorenzis, L. (2013). A computational contact formulation based on surface potentials. *Comput. Methods Appl. Mech. Engrg.*, **253**:369–395.
- Sauer, R. A. and De Lorenzis, L. (2015). An unbiased computational contact formulation for 3D friction. *Int. J. Numer. Meth. Engrg.*, **101**(4):251–280.
- Sauer, R. A. and Duong, T. X. (2017). On the theoretical foundations of solid and liquid shells. *Math. Mech. Solids*, **22**(3):343–371.
- Sauer, R. A., Duong, T. X., and Corbett, C. J. (2014). A computational formulation for constrained solid and liquid membranes considering isogeometric finite elements. *Comput. Methods Appl. Mech. Engrg.*, **271**:48–68.
- Sauer, R. A., Duong, T. X., Mandadapu, K. K., and Steigmann, D. J. (2017). A stabilized finite element formulation for liquid shells and its application to lipid bilayers. *J. Comput. Phys.*, **330**:436–466.
- Scott, M. A., Borden, M. J., Verhoosel, C. V., Sederberg, T. W., and Hughes, T. J. R. (2011). Isogeometric finite element data structures based on Bézier extraction of T-splines. *Int. J. Numer. Meth. Engrg.*, **88**(2):126–156.
- Shi, Z. and Baumgart, T. (2015). Membrane tension and peripheral protein density mediate membrane shape transitions. *Nature communications*, **6**:5974.
- Steigmann, D. J. (1999). Fluid films with curvature elasticity. *Arch. Rat. Mech. Anal.*, **150**:127–152.
- Tasso, I. V. and Buscaglia, G. C. (2013). A finite element method for viscous membranes. *Comput. Methods Appl. Mech. Engrg.*, **255**:226–237.
- Walani, N., Torres, J., and Agrawal, A. (2015). Endocytic proteins drive vesicle growth via instability in high membrane tension environment. *Proceedings of the National Academy of Sciences*, **112**(12):E1423–E1432.
- Zimmerberg, J. and Kozlov, M. M. (2006). How proteins produce cellular membrane curvature. *Nature Reviews Molecular Cell Biology*, **7**(1):9–19.
- Zimmermann, C. and Sauer, R. A. (2017). Adaptive local surface refinement based on LR-NURBS and its application to contact. <https://arxiv.org/1701.08742>.